Cross-link Inhomogeneity of Phenolic Resins

Atsushi Izumi

A dissertation submitted for the degree of Doctor of Philosophy

Department of Advanced Materials Science

Graduate School of Frontier Sciences

The University of Tokyo

2013

Contents

Chapter 1 General Introduction 7

1.1 Introduction 7

1.2 Outline of This Dissertation 10

1.3 References 13

Chapter 2 Atomistic Molecular Dynamics Study of Cross-Linked Phenolic Resins 17

2.1 Introduction 17

2.2 Simulation Method 19

2.2.1 General 19

2.2.2 Cross-linked Polymer Structure Modeling 21

2.2.2.1 Amorphous Structure of Uncross-linked Polymers 21

2.2.2.2 Cross-linking Reaction 23

2.2.2.3 Relaxation of Cross-linked Structures 26

2.2.3 Glass-Transition Temperature and Density 28

2.2.4 Uniaxial Elongation 31

2.2.4.1 Optimization of the Simulation Conditions 31

2.2.4.2 Structural Isotropy 33

2.3 Results and Discussion 34

2.3.1 Density and Poisson's Ratio 35

2.3.2 Stress and Strain Curves 36

2.3.3 Effect of Electrostatic Interactions 37

2.3.4 Distribution of the Bonding Potential Energies 37

2.3.5 Change in the Potential Energy 39

2.4 Conclusions 41

2.5 References 43

Chapter 3 Dynamic Light Scattering and Small-Angle Neutron Scattering Studies on Phenolic Resin Solutions 47

3.1 Introduction 47
3.2 Experimental 48
3.2.1 Materials 48
3.2.2 Sample Preparation 49
3.2.3 GPC 49
3.2.4 DLS 51
3.2.5 SANS 52
3.3 Results and Discussion 54
3.4 Conclusions 64
3.5 References 64

Chapter 4 Gelation and Cross-link Inhomogeneity of Phenolic Resins Studied by ^{13}C-NMR Spectroscopy and Small-Angle X-ray Scattering 69
4.1 Introduction 69
4.2 Experimental 70
4.2.1 Materials 70
4.2.2 Sample Preparation 71
4.2.3 GPC 72
4.2.4 Determination of the Degree of Swelling 72
4.2.5 ^{13}C-NMR Spectroscopy 72
4.2.6 SAXS 74
4.3 Results and Discussion 74
4.4 Conclusion 88
4.5 References 89

Chapter 5 Synthesis and Properties of a Deuterated Phenolic Resin 91
5.1 Introduction 91
5.2 Experimental 93
5.2.1 Materials 93
5.2.2 Polymerization 93
5.2.3 Measurements 94
5.2.3.1 General 94
5.2.3.2 GPC 94

5.2.3.3 SANS 95
5.3 Results and Discussion 96
5.3.1 Polymerization 96
5.3.2 Structure and Conformation 98
5.3.3 Curing Behavior 102
5.3.4 SANS 104
5.4 Conclusions 105
5.5 References 106

Chapter 6 Structural Analysis of Cured Phenolic Resins Using Complementary Small-angle Neutron and X-ray Scattering and Scanning Electron Microscopy 109
6.1 Introduction 109
6.2 Experimental 110
6.2.1 Materials 110
6.2.2 Sample Preparation 110
6.2.3 SANS 112
6.2.4 SAXS 112
6.2.5 SEM 113
6.3 Results and Discussion 113
6.3.1 SANS and SAXS 113
6.3.2 SEM 122
6.4 Conclusions 124
6.5 References 125

Summary 129

List of Publications 135

Acknowledgments 137

Chapter 1

General Introduction

1.1 Introduction

Phenolic resins were the first artificial plastics based on a synthetic polymer and were invented by Baekeland in 1907. Because of their excellent mechanical properties as well as heat and solvent resistance, they have been used as insoluble and infusible thermosetting resins in electronics, automotive, housing, and other industries.[1] The basic chemical structure of phenolic resins consists of a network of three functional phenols and two functional methylenes. Three methylenes can connect to a phenol, one at the *para*-position and the other two at the two *ortho*-positions that are adjacent to the hydroxyl group of the phenolic ring.

This cross-linked network that is usually prepared by curing novolac resins with a low degree of cross-linking provides the above-mentioned desirable properties. However, the structural analysis of phenolic resins is difficult because of their insolubility in common organic solvents and their infusibility. Therefore, elucidation of their cross-linked structure and inhomogeneity has been one of the major objectives of the structural analysis of phenolic and other thermosetting resins. The definition of "inhomogeneity of thermosetting resins" is well summarized in the literature.[2,3] Furthermore, it is well known that the case for the inhomogeneity of phenolic resins was first raised by de Boer and Houwink in 1936.[4,5] de Boer derived theoretical values of the tensile strength and Young's

modulus that were much higher than experimentally obtained values. Houwink suggested that the significant discrepancy between the theoretically predicted and experimental values could be explained by the presence of the inhomogeneity of cross-links, which results in structural defects, as explained by the Lockerstellen theory.

Scanning electron microscopy (SEM) and transmittance electron microscopy (TEM) have commonly been applied to the structural analysis of insoluble and infusible thermosetting resins, and the presence of inhomogeneity associated with nodular structures with particle sizes ranging from tens to hundreds of nanometers on free and etched fracture surfaces of cured thermosetting resins has been reported.[6–12] In addition, there have been many studies concerning the interpretation of the nodular morphology of a fracture surface, and two different interpretations have been made through the investigation of epoxy resins. One interpretation is that the nodular structure is ascribed to a domain with a high degree of cross-linking. Fracture occurs at the interfaces between the nodules and propagates along the nodules where the degree of cross-linking is lower than that of the nodules.[12] The other interpretation is that the nodular structure itself has nothing to do with the evidence of inhomogeneity in thermosetting resins because the etched fracture surfaces of amorphous poly(methyl methacrylate) (PMMA) and polystyrene (PSt) also exhibited similar nodular structures.[13] These interpretations of the nodular structure may depend on the analytical methods; the first interpretation is mainly supported by SEM and TEM observations of the fracture surfaces of thermosetting resins, while the second interpretation is supported by small-angle neutron and X-ray scattering (SANS and SAXS, respectively) observations of unfractured thermosetting resins. However, there are only a few SANS and SAXS studies addressing the nodular structures[2,13–15] as compared to the number of SEM and TEM studies of inhomogeneity. Dušek et al. reported that the nodular structure is not an inherent property of cured epoxy resins because (i) both SEM images of fracture surfaces and SAXS curves of cured epoxy resins did not differ in principle from those of amorphous PMMA and PSt and (ii) swollen epoxy resins in tetrahydrofuran

(THF) did not lead to an increase in the SAXS intensity corresponding to the particle size of 10–100 nm.[2,13] Matyi et al. reported that SAXS results for epoxy resins indicated the presence of an inhomogeneity that is not associated with the nodular structure but with voids having a size distribution range larger than 10–100 nm.[14] Bai reported that SANS results for epoxy resins indicated the absence of inhomogeneity of the cross-links in the range of 3–40 nm.[15] Tapping-mode atomic force microscopy observations have also been reported to understand the cross-link inhomogeneity of epoxy resins through the investigation of the hard and soft phases of the surface.[11,16,17] Duchet et al. reported that epoxy resins based on diglycidyl ether of bisphenol A (DGEBA) cured with diamines have homogeneous cross-linked networks on the nanometric scale because their phase images exhibited very homogeneous morphologies that did not differ from those of amorphous PMMA and PSt.[17] On the other hand, Kishi et al. reported inhomogeneous phase images for epoxy resins based on DGEBA oligomers having molecular weight distributions cured with dicyandiamide.[11] Arguments regarding the interpretation of the nodular structure persist even today, and the characterization of the relationship between the mechanical properties and the inhomogeneous nanostructures on the fracture surface remains an important focus of many investigations of thermosetting resins.[10–12]

For elucidating the inhomogeneity of gel networks, dynamic light scattering (DLS), SANS, and SAXS have proven to be powerful techniques.[18–24] For the study of thermosetting resins, such scattering techniques have typically been applied to the analysis of the phase separation of thermosetting and thermoplastic polymer blends,[25–27] the aggregation and distribution of nanometer-sized reinforcing fillers in nanocomposites,[28–30] and the pore structure of carbon.[31–34] However, only a few studies have addressed the inhomogeneity of thermosetting resins using these methods described above.

For characterizing the relationship between structure and properties at a theoretical level, Molecular dynamics (MD) simulations provide a powerful tool and have been broadly applied to polymer science.[35,36] An advantage of the application of MD simulations to the studies of thermosetting resins is that such

studies are not limited by polymer solubility and infusibility, which always cause experimental difficulties in structural analyses, as mentioned above. However, we believe that there have been no previous MD studies of phenolic resins pertaining to their cross-linked structures. Moreover, only a few MD studies of uncross-linked phenolic resins have been reported, such as those of polymer conformations,[37–39] glass-transition temperature,[38] water diffusion in the polymer,[38] pyrolysis behaviors using the reactive force field,[40,41] and the dynamic response to shock wave compression.[42]

1.2 Outline of This Dissertation

By considering above discussion and research background, I intended to study the relationship between the structural and mechanical properties using MD simulations for a theoretical understanding and the inhomogeneity of phenolic resins using scattering methods for the structural analysis. The following is the outline of this dissertation.

In Chapter 2, to characterize the structure–property relationships of cross-linked phenolic resins from the atomistic viewpoint, cross-linked phenolic resins were analyzed by using atomistic MD simulations. Cross-linked structures consisting of a network of three functional phenols and two functional methylenes with the degree of cross-linking of 0.70, 0.82, and 0.92 were prepared by cross-linking reactions of linear novolac-type phenolic resins in a unit cell under three-dimensional periodic boundary conditions. Uniaxial elongations of cross-linked structures to the strain of 0.03 were performed at 300 K. At this temperature, all structures were apparently in a glassy state, which was confirmed by an analysis of specific volume as a function of the temperature. The uniaxial elongation did not cause a significant change in the distribution of bonding potential energies (i.e., bond stretching, angle bending, and torsion angle potentials). On the other hand, the change in the potential energies owing to the uniaxial elongation indicated that cross-links suppressed local segmental motions

in the cross-linked structure, probably at the region around the linear and terminal phenols, which resulted in an increase in the degree of cross-linking accompanied by a decrease in Poisson's ratio and an increase in Young's modulus.

In Chapter 3, solution properties of unfractionated phenolic resins prepared by polycondensation of phenol and formaldehyde using oxalic acid as a catalyst were investigated by DLS and SANS. The hydrodynamic radius, obtained by DLS experiments with 1 vol% solution in acetone, and the correlation length (ξ) of the Ornstein–Zernike equation, obtained by SANS experiments with 10 vol% solution in tetrahydrofuran, obey a power-law relation as a function of *z*-average molecular weight estimated by gel permeation chromatography (GPC), with scaling exponents of 0.57 and 0.27, respectively. These behaviors are unaffected by polymerization conditions, such as initial phenol-to-formaldehyde molar ratio in the range from 0.9 to 1.5, catalyst concentration with oxalic acid-to-phenol molar ratio from 0.01 to 0.1, and reaction time within the period in which the polymer remains soluble. SANS curves for polymers prepared under different conditions are sufficiently superimposed onto a single curve with the reduced variables, $\xi^{-2}I(q)$ and ξq. These results indicate that unfractionated phenolic resins have a self-similar structure with respect to the molecular weight.

In Chapter 4, the gelation mechanism and cross-link inhomogeneity of phenolic resins prepared by polycondensation of phenol and formaldehyde under acidic conditions were studied by using ^{13}C-NMR spectroscopy and SAXS. The structural analysis of the gelation process indicated the presence of two different mechanisms of the formation and growth of the inhomogeneity that depend on the initial formaldehyde-to-phenol molar ratio: (i) When there is an insufficient amount of a cross-linker at the initial stage of gelation, inhomogeneous domains with a loosely cross-linked network appear and the degree of cross-linking in the domain increases with the reaction time. (ii) When there is a sufficient amount of a cross-linker at the initial stage of gelation, inhomogeneous domains with a tightly cross-linked network appear, followed by an increase in the size of the domain.

In Chapter 5, a highly deuterated novolac-type phenolic resin was prepared by polycondensation of deuterated phenol and formaldehyde using oxalic acid as an acid catalyst. The polycondensation of deuterated monomers and the formation of the highly deuterated phenolic resin were confirmed by the GPC, IR, and ^{1}H NMR analyses. With the exception of hydroxyl groups, the degree of deuteration was estimated to be more than 98%. The polymer conformation in THF solution was evaluated by the scaling exponent of the Mark–Houwink–Sakurada equation. The exponent of the deuterated phenolic resin is 0.26 in THF at 40 °C, and is close to that of a nondeuterated phenolic resin, which suggests that phenolic resins behave like a compact sphere irrespective of deuteration. The curing behavior of the deuterated phenolic resin with hexamethylenetetramine (HMTA) was confirmed by differential scanning calorimetry analysis. The cured highly deuterated phenolic resin exhibits a lower incoherent neutron scattering background than that of the nondeuterated phenolic resin, which suggests that the former is suitable for matrix resins with low incoherent backgrounds for SANS studies of thermosetting resins.

In chapter 6, the structure of cured phenolic resins prepared by compression molding of a deuterated phenolic resin oligomer and nondeuterated HMTA as a curing agent was investigated using complementary SANS, SAXS, and SEM. Cured thermosetting resins have been considered to have an inherent inhomogeneity of the cross-links with sizes ranging from tens to hundreds of nanometers based on SEM observations of fracture surfaces. However, such spatial inhomogeneity has not been observed for the phenolic resins by either SANS or SAXS. The present observation with SANS and SAXS indicates that the phenolic resins have an inhomogeneity associated with internal fractal interfaces between voids and phenolic resins, with a fractal dimension equal to 2.5–2.6 in the range of 3–1600 nm. The presence of voids in phenolic resins with sizes ranging from tens to hundreds of nanometers is clearly confirmed by an evaluation of the difference in scattering length densities between the SANS and SAXS functions and by SEM observations of etched surfaces prepared by focused-ion beam milling. Therefore, it can be concluded that (i) cross-links are

randomly distributed over the range and (ii) the spatial inhomogeneity of the cross-links in that range is very small and negligible in comparison with the inhomogeneity associated with the internal fractal interfaces in terms of the fluctuations of the neutron and X-ray scattering length densities.

1.3 References

1 A. Gardziella, L. A. Pilato and A. Knop, *Phenolic Resins: Chemistry, Applications, Standardization, Safety and Ecology*, 2nd completely rev. edn., Springer, Berlin, 1999.

2 K. Dušek, *Angew. Makromol. Chem.*, 1996, **240**, 1–15.

3 J. P. Pascault, H. Sautereau, J. Verdu and R. J. J. Williams, *Thermosetting Polymers*, Marcel Dekker, New York, 2002.

4 J. H. de Boer, *Trans. Faraday Soc.*, 1936, **32**, 10–37.

5 R. Houwink, *Trans. Faraday Soc.*, 1936, **32**, 122–131.

6 R. A. Spurr, E. H. Erath, H. Myers and D. C. Pease, *Ind. Eng. Chem.*, 1957, **49**, 1839–1842.

7 E. H. Erath and R. A. Spurr, *J. Polym. Sci.*, 1959, **35**, 391–399.

8 J. L. Racich and J. A. Koutsky, *J. Appl. Polym. Sci.*, 1976, **20**, 2111–2129.

9 V. B. Gupta, L. T. Drzal, W. W. Adams and R. Omlor, *J. Mater. Sci.*, 1985, **20**, 3439–3452.

10 J. Mijović and L. Tsay, *Polymer*, 1981, **22**, 902–906.

11 H. Kishi, T. Naitou, S. Matsuda, A. Murakami, Y. Muraji and Y. Nakagawa, *J. Polym. Sci., Part B: Polym. Phys.*, 2007, **45**, 1425–1434.

12 J. Mijović and J. A. Koutsky, *Polymer*, 1979, **20**, 1095–1107.

13 K. Dušek, J. Pleštil, F. Lednický and S. Luňák, *Polymer*, 1978, **19**, 393–397.

14 R. J. Matyi, D. R. Uhlmann and J. A. Koutsky, *J. Polym. Sci., Part B: Polym. Phys.*, 1980, **18**, 1053–1063.

15 S. J. Bai, *Polymer*, 1985, **26**, 1053–1057.

16 M. R. Vanlandingham, R. F. Eduljee and J. W. Gillespie, *J. Appl. Polym. Sci.*, 1999, **71**, 699–712.

17 J. Duchet and J. P. Pascault, *J. Polym. Sci., Part B: Polym. Phys.*, 2003, **41**, 2422–2432.

18 M. Shibayama, *Macromol. Chem. Phys.*, 1998, **199**, 1–30.

19 M. Shibayama and T. Norisuye, *Bull. Chem. Soc. Jpn.*, 2002, **75**, 641–659.

20 M. Shibayama, T. Karino, Y. Domon and K. Ito, *J. Appl. Cryst.*, 2007, **40**, s43–s47.

21 M. Shibayama, *Polym. J.*, 2011, **43**, 18–34.

22 M. Shibayama, *Soft Matter*, 2012, **8**, 8030–8038.

23 J. Bastide and S. J. Candau, Structure of gels as investigated by means of static scattering techniques. in *Physical Properties of Polymeric Gels*, ed. J. P. Cohen Addad, John Wiley, New York, 1996, pp. 143–308.

24 W. L. Wu, M. Shibayama, S. Roy, H. Kurokawa, L. D. Coyne, S. Nomura and R. S. Stein, *Macromolecules*, 1990, **23**, 2245–2251.

25 E. Girard-Reydet, H. Sautereau, J. P. Pascault, P. Keates, P. Navard, G. Thollet and G. Vigier, *Polymer*, 1998, **39**, 2269–2279.

26 F. L. Meng, S. X. Zheng, H. Q. Li, Q. Liang and T. X. Liu, *Macromolecules*, 2006, **39**, 5072–5080.

27 D. Hu, Z. G. Xu, K. Zeng and S. X. Zheng, *Macromolecules*, 2010, **43**, 2960–2969.

28 J. Brus, M. Špírková, D. Hlavatá and A. Strachota, *Macromolecules*, 2004, **37**, 1346–1357.

29 D. W. Schaefer and R. S. Justice, *Macromolecules*, 2007, **40**, 8501–8517.

30 H. Zou, S. S. Wu and J. Shen, *Chem. Rev.*, 2008, **108**, 3893–3957.

31 E. Hoinkis and A. J. Allen, *Carbon*, 1991, **29**, 81–91.

32 A. Gupta and I. R. Harrison, *Carbon*, 1994, **32**, 953–960.

33 J. M. Calo, P. J. Hall and M. Antxustegi, *Colloids Surf., A*, 2001, **187–188**, 219–232.

34 J. M. Calo and P. J. Hall, *Carbon*, 2004, **42**, 1299–1304.

35 K. Binder, *Monte Carlo and Molecular Dynamics Simulations in Polymer*

Science, Oxford University Press, Oxford, 1995.

36 K. Kremer and F. Müller-Plathe, *Mol. Simulat.*, 2002, **28**, 729–750.

37 B. L. Schürmann and L. Vogel, *J. Mater. Sci.*, 1996, **31**, 3435–3440.

38 A. R. Pawloski, J. A. Torres, P. F. Nealey and J. J. de Pablo, *J. Vac. Sci. Technol. B*, 1999, **17**, 3371–3378.

39 S. S. Choi, *Polym. Adv. Technol.*, 2001, **12**, 567–573.

40 D. E. Jiang, A. C. T. van Duin, W. A. Goddard and S. Dai, *J. Phys. Chem. A*, 2009, **113**, 6891–6894.

41 T. G. Desai, J. W. Lawson and P. Keblinski, *Polymer*, 2011, **52**, 577–585.

42 B. Arman, Q. An, S. N. Luo, T. G. Desai, D. L. Tonks, T. Çağın and W. A. Goddard III, *J. Appl. Phys.*, 2011, **109**, 013503.

Chapter 2

Atomistic Molecular Dynamics Study of Cross-Linked Phenolic Resins

2.1 Introduction

Molecular dynamics (MD) simulations provide a powerful tool for characterizing the relationship between structure and properties at a theoretical level and have been broadly applied to polymer science.[1,2] An advantage of the application of MD simulations to the studies of thermosetting resins is that such studies are not limited by polymer solubility and infusibility, which always cause experimental difficulties in structural analyses, as mentioned in Chapter 1. However, we believe that there have been no previous MD studies of phenolic resins pertaining to their cross-linked structures. Moreover, only a few MD studies of uncross-linked phenolic resins have been reported, such as those of polymer conformations,[3–5] glass-transition temperature,[4] water diffusion in the polymer,[4] pyrolysis behaviors using the reactive force field,[6,7] and the dynamic response to shock wave compression.[8]

A disadvantage associated with MD studies of thermosetting resins is the difficulty in modeling cross-linked chemical structures using fully atomistic models under three-dimensional (3D) periodic boundary conditions. A solution to this modeling issue is to apply coarse-grained models, which represent a set of atoms as a dynamic unit having no strict chemical structures. The simplest coarse-grained model is the united atom model in which hydrogens are

incorporated into the attached atoms. Thus, in response to the molecular modeling issue, the coarse-grained models have been broadly applied to the MD studies of cross-linked thermosetting resins.[9–17] On the other hand, fully atomistic MD studies of cross-linked polymers have recently been intensively investigated to characterize the structure–property relationships from the atomistic viewpoint, and many methodologies for the atomistic molecular modeling of cross-linked structures have been developed for epoxy resins,[18–35] poly(methacrylate)s,[36] poly(vinyl alcohol)s,[37,38] and poly(dimethylsiloxane)s.[39] Among these polymers, epoxy resins are one of the typical thermosetting resins as are phenolic resins that have become the mainstream focus of the MD studies of thermosetting resins owing to the establishment of the methodology for the atomistic molecular modeling of cross-linked structures. In addition, MD simulations of cross-linked epoxy resins have proved to be a promising tool, providing details regarding structure–property relationships that could not be obtained experimentally, such as the heat transport mechanism[26] and effect of moisture and nanoparticles on mechanical properties.[24,27] However, these techniques have not yet been applied to cross-linked phenolic resins, another typical class of thermosetting resins that have been experimentally studied for more than 100 years. Furthermore, computational studies of cross-linked phenolic resins have also been limited, and except for MD simulations, they have only been applied to the Monte Carlo study of network formation.[40] Thus, the development and refinement of MD studies of cross-linked phenolic resins would provide new insights into the relationships between structure and mechanical properties, which have not yet been clearly elucidated experimentally.

In this chapter, we report MD studies of cross-linked phenolic resins using fully atomistic models: (i) modeling of the cross-linked structures consisting of phenols and methylenes and (ii) characterization of structure and mechanical properties by uniaxial elongation. We believe that this is the first report on fully atomistic MD studies of highly cross-linked novolac-type phenolic resins.

2.2 Simulation Method

2.2.1 General

Molecular modeling and MD calculations were performed on J-OCTA 1.3 (JSOL Corporation, Japan) and COGNAC 6.1.3.[41] Partial charges were estimated using Gaussian03 (Gaussian, Inc., USA) and the Restrained Electrostatic Potential (RESP) fitting program.[42,43]

DREIDING force field was applied in terms of the generality of potential parameters that are widely applicable to organic materials.[44] The set of potential functions (U) is described by $U = U_b + U_{nb}$, where U_b and U_{nb} denote bonding and nonbonding potentials, respectively. In DREIDING, the bonding interaction consists of four terms, namely, a two-body bond-stretching potential (U_B), a three-body angle-bending potential (U_A), a four-body torsion-angle potential (U_T), and a four-body improper-torsion potential (U_I), such that $U_b = U_B + U_A + U_T + U_I$. The nonbonding interaction consists of three terms, namely, the van der Waals interaction potential (U_{VDW}), an electrostatic-interaction potential (U_Q), and an explicit hydrogen-bonding-interaction potential (U_{HB}), such that $U_{nb} = U_{VDW} + U_Q + U_{HB}$. In DREIDING, these terms, except for U_{HB} and U_Q, can be described as follows:

$$U_B = \frac{1}{2} K_B (r - r_e)^2, \tag{2.1}$$

$$U_A = \frac{1}{2} K_A (\theta - \theta_e)^2, \tag{2.2}$$

$$U_T = \frac{1}{2} K_T \{1 - \cos[n(\varphi - \varphi_e)]\}, \tag{2.3}$$

$$U_I = \frac{1}{2} \frac{K_I}{(\sin \psi_e)^2} (\cos \psi - \cos \psi_e)^2, \tag{2.4}$$

$$U_{VDW} = D_0 \left[\left(\frac{R_0}{R} \right)^{12} - 2 \left(\frac{R_0}{R} \right)^6 \right], \tag{2.5}$$

where K_B, K_A, K_T, and K_I denote spring constants; r denotes bond length; θ denotes bond angle; φ and ψ denote torsion angles; D_0 indicates the van der Waals well depth; R_0 indicates the van der Waals bond length that is equal to the distance at which U_{VDW} reaches its minimum value (i.e., $-D_0$); R indicates the distance between atoms. The subscript "e" signifies "at equilibrium". In this study, U_I was combined into U_T by rearranging eqs 2.3 and 2.4 to a cosine polynomial form, given by

$$U_T = K\sum_{n=0}^{N-1} A_n \cos^n \varphi , \tag{2.6}$$

where K, $N-1$, and A_n denote a constant, order of polynomial, and constants, respectively. The Ewald summation method was applied in the calculation of U_Q with a cutoff length (r_{cutoff}) defined by

$$r_{cutoff} = \frac{11.5^{0.5}}{\pi^{0.5}\left(\frac{5.5N_{atom}}{V_{cell}^{\ 2}}\right)^{1/6}} , \tag{2.7}$$

where N_{atom} and V_{cell} denote number of atoms in a unit cell and volume of a unit cell, respectively.[45,46] Note that U_{HB} was not applied in this study as it was assumed that U_Q can represent the hydrogen-bonding interactions involving the hydrogens and oxygens of the hydroxyl groups in phenolic resins because the hydrogen-bonding interactions are fundamentally electrostatic interactions. Thus, the bonding and nonbonding interactions were given by $U_b = U_B + U_A + U_T$ and $U_{nb} = U_{VDW} + U_Q$, respectively. In the "Simulation Method" section, the calculation of U_Q is performed only in section 2.2.2.1 (iv).

Partial charges of phenolic resins were approximated by those of the model structures shown in Figures 2.1a and 2.1b. Molecular electrostatic potentials at the molecular surfaces of the model structures were estimated by density functional theory calculations using B3LYP with the 6-31G(d) basis set. The RESP fitting scheme was applied to set the same partial charge on geometrically equivalent atoms. The values of the partial charges of methylenes in 2-(2-hydroxybenzyl)phenol (**1a**), 4-(2-hydroxybenzyl)phenol (**1b**), and

4-(4-hydroxybenzyl)phenol (**1c**) were applied to the *o–o'*, *o–p'*, and *p–p'* bridged methylenes in the phenolic resins, respectively. The values of the partial charges of phenolic rings, including the attached hydrogens and a hydroxyl group, in 2-benzylphenol (**2a**), 2,4-bisbenzylphenol (**2b**), 2,6-bisbenzylphenol (**2c**), and 2,4,6-trisbenzylphenol (**2d**) were applied to the *o*-, *o,p*-, *o,o*-, and *o,o,p*-linked phenolic rings, respectively. Note that mono *p*-substituted phenolic rings were absent from our system because all phenolic rings were initially *ortho*-substituted, as described in the following sections. After assigning the partial charges of model structures to phenolic resins, the resulting negative or positive excess charge in the system was distributed to all atoms proportional to the absolute value of the assigned partial charge to give an electrically neutral cell.

2.2.2 Cross-linked Polymer Structure Modeling

Cross-linked phenolic resins consisting of a network of phenols and methylenes, as shown in Figure 2.1c, were three-dimensionally modeled by cross-linking reactions of linear polymers under 3D boundary conditions. Detailed procedures are described in the following subsections.

2.2.2.1 Amorphous Structure of Uncross-linked Polymers

A linear novolac-type phenolic resin having an all-*ortho* configuration, as shown in Figure 2.1d, was modeled as an uncross-linked phenolic resin. The degree of polymerization was chosen to be 9, which corresponds to the molecular weight of 943 g mol^{-1}. Note that this value was chosen considering low-molecular weight phenolic resins with the number-average molecular weight of hundreds to a thousand g mol^{-1} are commonly used as starting materials in the curing process for their better processability (i.e., low viscosity).[47]

Amorphous structures of uncross-linked phenolic resins at the temperature (T) of 450 K, which is within the typical molding and curing temperature range for phenolic resins in the manufacturing process,[47] were obtained by the following procedure: (i) In a cubic MD cell under the 3D periodic

boundary condition, 50 polymers were randomly placed and the size of the cell was adjusted to have the density (d) of 0.3 g cm^{-3}. (ii) The polymers were stirred for 200 ps in the canonical (NVT) ensemble (T = 600 K and the integration time step of the velocity Verlet algorithm (Δt) = 1 fs). This high temperature (600 K)

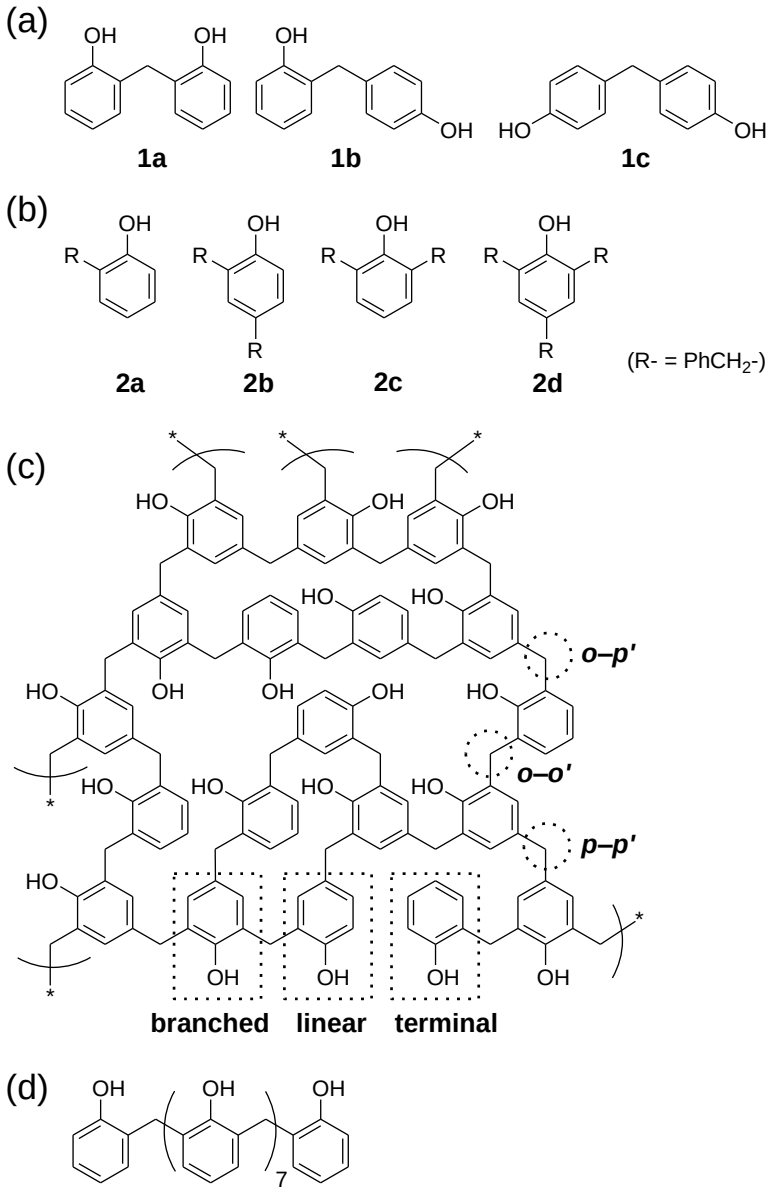

Figure 2.1 Chemical structures of phenolic resins: Model structures for estimating partial charges of (a) methylenes and (b) phenolic rings in (c) cross-linked and (d) uncross-linked novolac-type phenolic resins. The classification of *o–o′*, *o–p′*, and *p–p′* methylene linkages and that of branched, linear, and terminal phenolic rings in the cross-linked structures are shown in (c).

was chosen to generate more possible conformations effectively. The geometrical and topological independence of polymer structures generated at every 10 ps was confirmed through an evaluation of the pair-distribution function of carbon atoms of the methylene groups. (iii) Twenty instantaneous structures obtained at every 10 ps during the stirring process were compressed in the isothermal–isobaric (NPT) ensemble (T = 450 K, the external pressure (P) = 10 GPa, and Δt = 0.5 fs) to give structures with d equal to 1.5 g cm^{-3}. (iv) The compressed structures were relaxed in the NPT ensemble (T = 450 K, P = 0.1 MPa, and Δt = 0.2 fs) to give 20 different amorphous structures of uncross-linked phenolic resins with d equal to 1.0 g cm^{-3}. Note that the Berendsen algorithm was chosen in the procedures (ii)–(iv) for its stability even under drastic cell deformations.[48] In the following investigations, the Nosé–Hoover algorithm was used for the temperature control,[49] and the Andersen and the Parrinello–Rahman algorithms were used for pressure control in isotropic cubic cell deformations and anisotropic rectangular cuboid cell deformations, respectively.[50,51]

2.2.2.2 Cross-linking Reaction

The cross-linking reactions, as shown in Figure 2.2, were performed as described in the following procedure: (v) A pair of reactive carbons at the first nearest neighbor and not on the same phenolic ring was chosen, in which the reactive carbons denote the hydrogen-substituted *o*- or *p*-carbons that are adjacent to the hydroxyl group of a phenolic ring. (vi) Two hydrogens attached to the chosen carbons were removed. (vii) A methylene was inserted between the positions of these carbons from which the hydrogens had been removed. (viii) The carbons were connected via the carbon of the inserted methylene group. These procedures (v)–(viii) were repeated until the degrees of cross-linking (D) reached 0.70, 0.82, and 0.92. Here D is defined by $D = (2N_{CH2}) / (3N_{PhOH})$, where N_{CH2} and N_{PhOH} denote the number of methylene groups and phenolic rings in a unit cell, respectively. Note that in all structures, N_{PhOH} is 450 because they were initially created with the 50 polymer chains having the degree of polymerization of 9. The

values of N_{CH2} were 470, 552, and 621 and those of N_{atom} were 6320, 6402, and 6471 for structures with D equal to 0.70, 0.82, and 0.92, respectively. The DREIDING force field and partial charges were reassigned to the resulting new structures to give 20 different cross-linked structures for each D.

The characterization of these obtained structures, that is, the fraction of *o–o'*, *o–p'*, and *p–p'* methylene linkages and that of branched, linear, and terminal phenolic rings, as shown in Figure 2.1c, are listed in Tables 2.1 and 2.2 (the average value with the standard deviation of 20 different structures for each of uncross-linked and cross-linked structures). In these structures, branched, linear, and terminal phenolic rings denote phenolic rings that are attached to three, two,

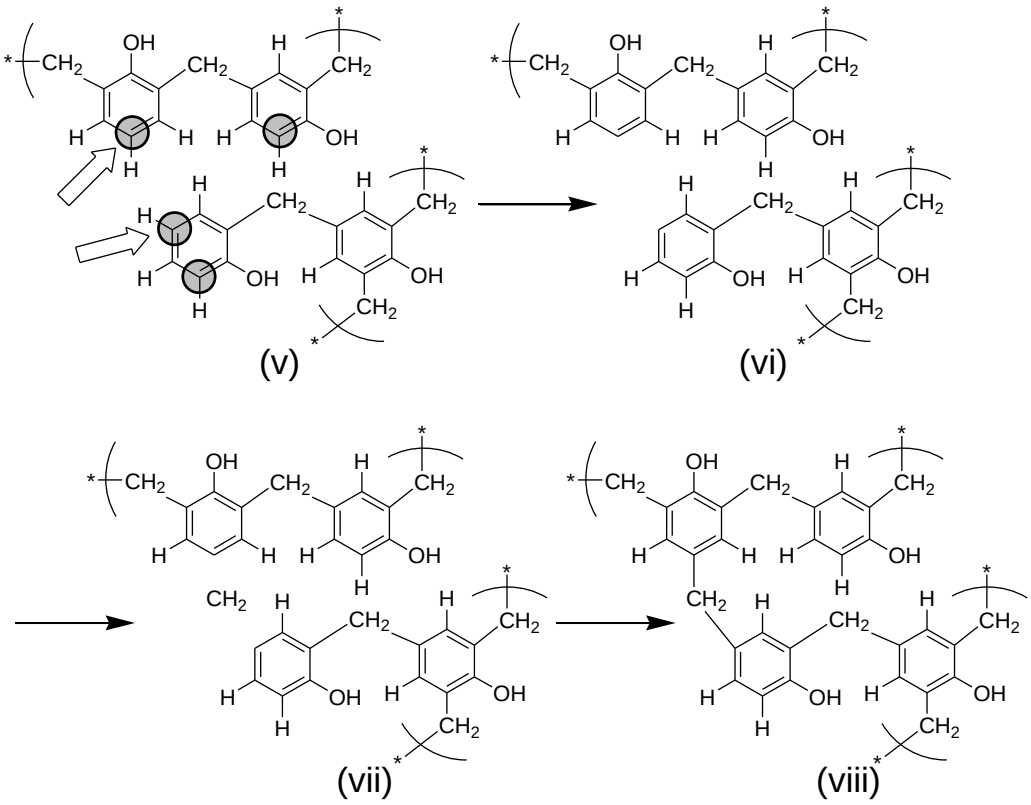

Figure 2.2 Scheme of cross-linking reactions: (v) Reactive carbons (marked with filled circles) and those at the first nearest neighbor (marked with arrows). (vi) Two hydrogens were removed from the selected carbons. (vii) A methylene was inserted between the carbons. (viii) Two new bonds were created between the methylene and the selected carbons. Figure numbers (v)–(viii) correspond to the procedure numbers (v)–(viii) in section 2.2.2.2.

Table 2.1 Components of methylene linkages[a]

polymer	N_{CH2}	*o*–*o′* / %	*o*–*p′* / %	*p*–*p′* / %
uncross-linked	400	100	0	0
D = 0.70	470	85.5 ± 0.2	4.2 ± 1.0	10.3 ± 1.0
D = 0.82	552	73.2 ± 0.2	7.8 ± 0.7	19.0 ± 0.7
D = 0.92	621	65.4 ± 0.3	10.3 ± 0.6	24.3 ± 0.4

[a] The average value with the standard deviation of 20 structures.

Table 2.2 Components of phenolic rings[a]

polymer	N_{PhOH}	branched / %	linear / %	terminal / %
uncross-linked	450	0	43.8	56.3
D = 0.70	450	21.8 ± 1.1	65.3 ± 2.1	12.9 ± 1.1
D = 0.82	450	50.5 ± 0.7	44.3 ± 1.4	5.2 ± 0.7
D = 0.92	450	77.3 ± 0.3	21.4 ± 0.7	1.3 ± 0.3

[a] The average value with the standard deviation of 20 structures.

and one methylenes, respectively. The *o*–*o′*, *o*–*p′*, and *p*–*p′* methylene linkages denote the *o*–*o′*, *o*–*p′*, and *p*–*p′* bridged methylenes in the phenolic resins, respectively.

Note that highly strained structures are produced by simultaneous cross-linking reactions carried out in the absence of any relaxation step between the cross-linking cycles. However, procedures (v)–(viii) did not require reactions between carbons separated by an unreasonably long distance. The cutoff distances of our system are calculated as follows: The shortest distance between two reactive carbons (which corresponds to the distance in the first cross-linking reaction step) for all structures was 3.14 ± 0.06 Å (the average and standard deviation of the 20 structures). The longest distances between two reactive carbons (which correspond to the distance at the first cross-linking reaction steps) for structures with *D* equal to 0.70, 0.82, and 0.92 were 3.80 ± 0.04, 4.27 ± 0.04, and 5.21 ± 0.10 Å, respectively. In reaction procedures (v)–(viii), the length of the

newly created bonds was equal to half the distance between two reactive carbons because two phenolic rings carbons were connected via the carbon of the inserted methylene group. Thus, new bonds were created between carbons of phenolic rings and methylene groups separated by a distance within the range from 1.57 ± 0.03 Å to 1.90 ± 0.02, 2.14 ± 0.02, and 2.61 ± 0.05 Å for structures with *D* equal to 0.70, 0.82, and 0.92, respectively.

2.2.2.3 Relaxation of Cross-linked Structures

The main objective of the cross-linking reaction described in the previous subsection was to construct new molecular structures. The initially obtained cross-linked structures were geometrically highly strained and required a relaxation process before investigation. Figure 2.3 shows the changes in the stress (σ_x, σ_y, and σ_z) and the cell length (*a*, *b*, and *c*) of a cross-linked structure with *D*

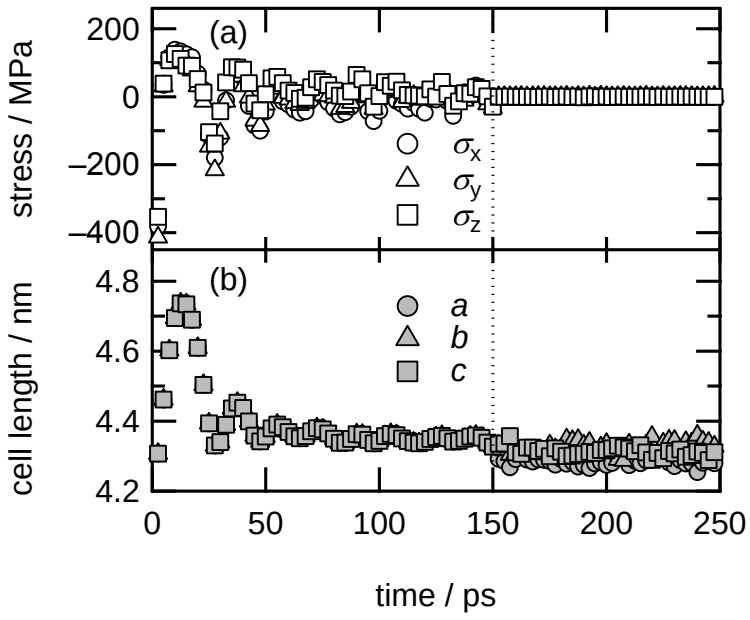

Figure 2.3 Changes in (a) the stress and (b) the cell edge length during the relaxation process for a cross-linked structure with D = 0.92. A unit cell was maintained to be cubic at 0−150 ps, then allowed to deform and be a rectangular cuboid cell at 150−250 ps: Open circle, σ_x; Open triangle, σ_y; Open square, σ_z; Filled circle, *a*; Filled triangle, *b*; Filled square, *c*.

equal to 0.92 in the NPT ensemble (T = 450 K, P = 0.1 MPa, and Δt = 0.5 fs) using the Andersen and Nosé–Hoover algorithms at 0−150 ps and the Parrinello–Rahman and Nosé–Hoover algorithms at 150−250 ps. Here σ_x, σ_y, and σ_z denote the stress of the unit cell parallel to the *x*-, *y*-, and *z*-axes, respectively, and *a*, *b*, and *c* represent the edge lengths of the unit cell along the *x*-, *y*-, and *z*-axes, respectively. As seen in the figure, an oscillation-like fluctuation of the stress did not settle even at 150 ps, which suggests that the highly strained structure that has a very short distance between cross-links (i.e., equivalent to the size of a phenolic ring), could not be relaxed under the regulation of a cubic unit cell (i.e., $a = b = c$). Thus, additional relaxation steps using the Parrinello–Rahman algorithm, instead of the Andersen algorithm, were applied to permit an anisotropic cell deformation to be a rectangular cuboid cell by allowing unit cell lengths, *a*, *b*, and *c*, to vary independently at each calculation time step, while unit cell angles were fixed at 90°. As seen in Figure 2.3a, just after 150 ps, the fluctuation in the stress successfully diminished, and the order of magnitude of the average stress settled to that of the external pressure (i.e., P = 0.1 MPa) owing to the rectangular cuboid cell deformation. Note that the fluctuation of cell lengths after 150 ps can be seen in Figure 2.3b, however, the variation of each cell length during 200–250 is sufficiently small in comparison with the cell length (i.e., the values of *a*, *b*, and *c* were in the range 4.25–4.31, 4.29–4.36, and 4.29–4.33 nm, respectively).

On the basis of these results, all cross-linked structures were first relaxed with maintaining cubic cells in the NPT ensemble using the Andersen and Nosé–Hoover algorithms for 100 ps (T = 450 K, P = 0.1 MPa, and Δt = 0.5 fs). Then, using the Parrinello–Rahman and Nosé–Hoover algorithms, the structures were relaxed for an additional 100 ps (T = 300 K, P = 0.1 MPa, and Δt = 0.5 fs). During the second relaxation step, unit cell lengths were allowed to vary independently at each calculation time step, while unit cell angles were fixed at 90° to give rectangular cuboid cells, as shown in Figure 2.4. The temperature of the second relaxation step was set at 300 K for the subsequent uniaxial elongation studies.

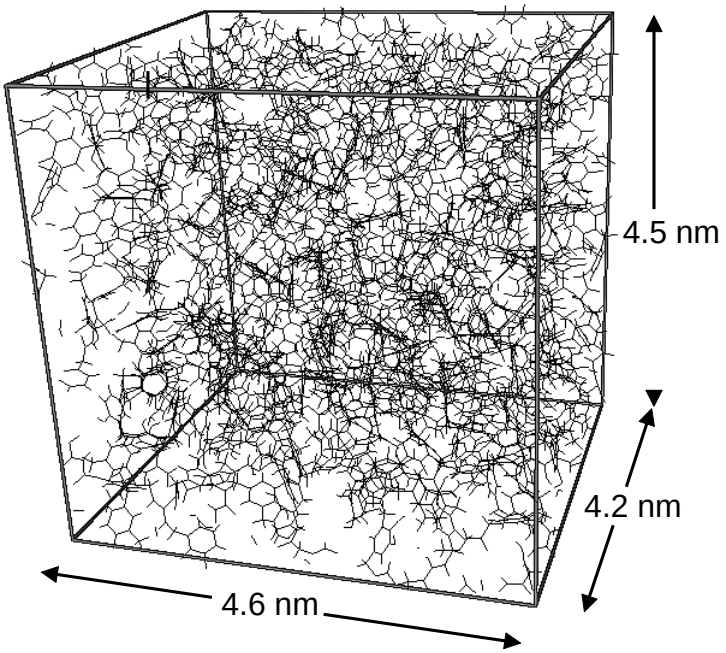

Figure 2.4 Relaxed structure of a cross-linked phenolic resin (N_{atom} = 6471 and D = 0.92) in a rectangular cuboid cell.

2.2.3 Glass-Transition Temperature and Density

The glass-transition temperatures (T_g) of the uncross-linked and cross-linked structures were evaluated by analyzing the change in the slope of the specific volume (V_{sp}) as a function of T, where V_{sp} is equal to the inverse of d. The temperatures were varied to 275 K decreasing stepwise in 25 K increments, from 600 K for the uncross-linked structure and 600, 650, and 775 K for the structures with D equal to 0.70, 0.82, and 0.92, respectively. Note that these temperature ranges were determined through preliminary investigations with a couple of randomly chosen structures for each of uncross-linked and cross-linked structures. At each temperature, uncross-linked structures in cubic cells were equilibrated in the NPT ensemble using the Andersen and Nosé–Hoover algorithms for 100 ps (P = 0.1 MPa and Δt = 1 fs), whereas cross-linked structures with D equal to 0.70, 0.82, and 0.92 were equilibrated in the NPT ensemble using the

Parrinello–Rahman and Nosé–Hoover algorithms for 100 ps (P = 0.1 MPa and Δt = 1 fs), and the unit cell lengths were allowed to vary independently at each calculation time step, while unit cell angles were fixed at 90°. Subsequently, V_{sp} was evaluated at an average of 50–100 ps. Figure 2.5 shows the changes in the average V_{sp} of 20 structures (error bars represent the 95% confidence intervals, in which error bars in Figures 2.5a and 2.5b are hidden by the graph markers because the values of the errors are less than 0.0024 and 0.0032 $cm^3\ g^{-1}$, respectively). Changes in the slopes were observed at 445 ± 11, 472 ± 18, 545 ± 23, and 632 ± 36 K for the uncross-linked structure, structures with D equal to 0.70, 0.82, and 0.92, respectively. This result clearly indicates that an increase in D accompanies an increase in T_g. Note that these values were estimated by fitting the values of V_{sp} using two linear functions at lower and upper temperature ranges for each of the 20 different uncross-linked and cross-linked structures. For this analysis, the lower temperature range was 275–400 K for all structures and the upper temperature ranges were 500–600, 500–600, 600–650, and 650–775 K for the uncross-linked structure and the structures with D equal to 0.70, 0.82, and 0.92, respectively. Then, T_g was determined as an average of the 20 values with error.

The result for the uncross-linked structure, as shown in Figure 2.5a, agrees with that for a previously reported MD study (d = 1.05 g cm^{-3}, corresponding to V_{sp} = 0.95 $cm^3\ g^{-1}$, T_g = 450 K) based on a similar structure, namely, a linear novolac-type phenolic resin having an all-*ortho* configuration with the degree of polymerization of 10 and a methyl group attached at the *ortho*-position of one of the terminal phenolic rings.[4] This previous study was calculated with the Polymer Consistent Force Field and the 9-6 Lennard–Jones nonbonding potential. Note that the typical experimental values of d for uncross-linked novolac-type phenolic resin oligomers at room temperature is about 1.2 g cm^{-3}, which corresponds to V_{sp} of 0.83 $cm^3\ g^{-1}$. The deviation between experimental and calculated values would result from weak nonbonding attractive interactions in the MD calculations, which lower the density in the MD results. This could be resolved by optimizing the DREIDING force field parameters for the phenolic resins.

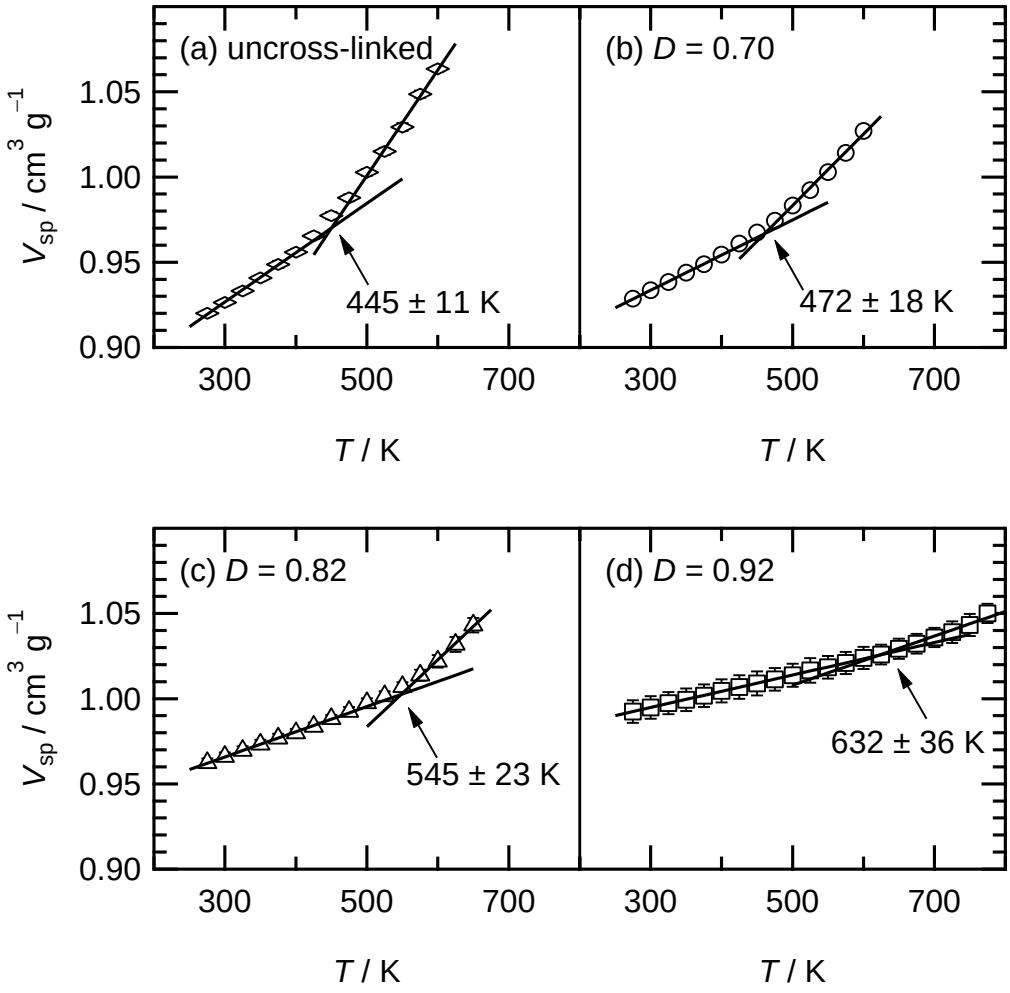

Figure 2.5 Change in specific volume: (a) Uncross-linked, (b) D = 0.70, (c) D = 0.82, and (d) D = 0.92.

The values of V_{sp} at 300 K for the uncross-linked structure, structures with D equal to 0.70, 0.82, and 0.92 were 0.926, 0.934, 0.966, and 0.995 $cm^3\ g^{-1}$, respectively, which correspond to the values of d equal to 1.08, 1.07, 1.04, and 1.01 $g\ cm^{-3}$, respectively. This result is contradictory to the general experimental result of cure shrinkage. In general, the cure shrinkage of thermosetting resins results from (i) thermal shrinkage, (ii) a decrease in the mass owing to the evaporation of low-molecular weight molecules (i.e., water, solvent, and monomers), and (iii) a decrease in the free volume due to the formation of new

covalent bonds. Reason (i) is clearly observed in Figure 2.5. Reason (ii) is not the case with our modeling scheme. On the other hand, there is an increase of one atom per cross-linking reaction cycle because the insertion of one methylene group rather than the removal of two hydrogens is performed, which may lead to a decrease in the density resulting from the cross-linking reaction. Reason (iii) is the case with our system because two reactive carbons were bridged via the methylene carbon in the cross-linking reaction and their distance was consequently reduced to 2.52 ± 0.06 Å after structural relaxation at 300 K. This distance is clearly shorter than the lower cutoff distance (3.14 ± 0.06 Å) of the cross-linking reaction (i.e., the distance between the first nearest neighbor reactive carbons before the cross-linking reaction). Moreover, it is experimentally well known that low-molecular weight or uncross-linked phenolic resins adopt a dense or packed structure because the conformation of a phenolic resin molecule is compact or short, which is elucidated by an analysis of the intrinsic viscosity as a function of the absolute molecular weight (see Chapter 5.3.2). In addition, there are many intra- and inter-molecular hydrogen bonds in the phenolic resins, whose chemical structure is shown in Figure 2.1c. These structural properties would also reduce the cure shrinkage resulting from reason (iii). These cure shrinkage mechanisms could also be resolved by optimizing the DREIDING force field parameters for the phenolic resins.

2.2.4 Uniaxial Elongation

2.2.4.1 Optimization of the Simulation Conditions

Uniaxial elongations of the cross-linked structures were investigated in the NPT ensemble using the Parrinello–Rahman and Nosé–Hoover algorithms, in which the cell deformation perpendicular to the elongation direction was induced by the external pressure. Thus, the order of magnitude of the stress perpendicular to the elongation direction, that is, σ_x and σ_y in the uniaxial elongation along the *z*-axis, should ideally be equal to that of the external pressure. To optimize the simulation conditions for the uniaxial elongation, the influence of Δt, the constant

elongation rate ($d\varepsilon/dt$), and the cell mass (M_{cell}) on σ_x, σ_y, and σ_z was investigated. Here the cell mass corresponds to a virtual mass of a unit cell used in the pressure control algorithm and ε denotes the strain defined by $\varepsilon = (c - c_0)/c_0$ for the elongation along the z-axis, where c_0 denotes the initial value of c before elongation.

Figures 2.6a–d show the changes in σ_x, σ_y, and σ_z for an equivalent initial

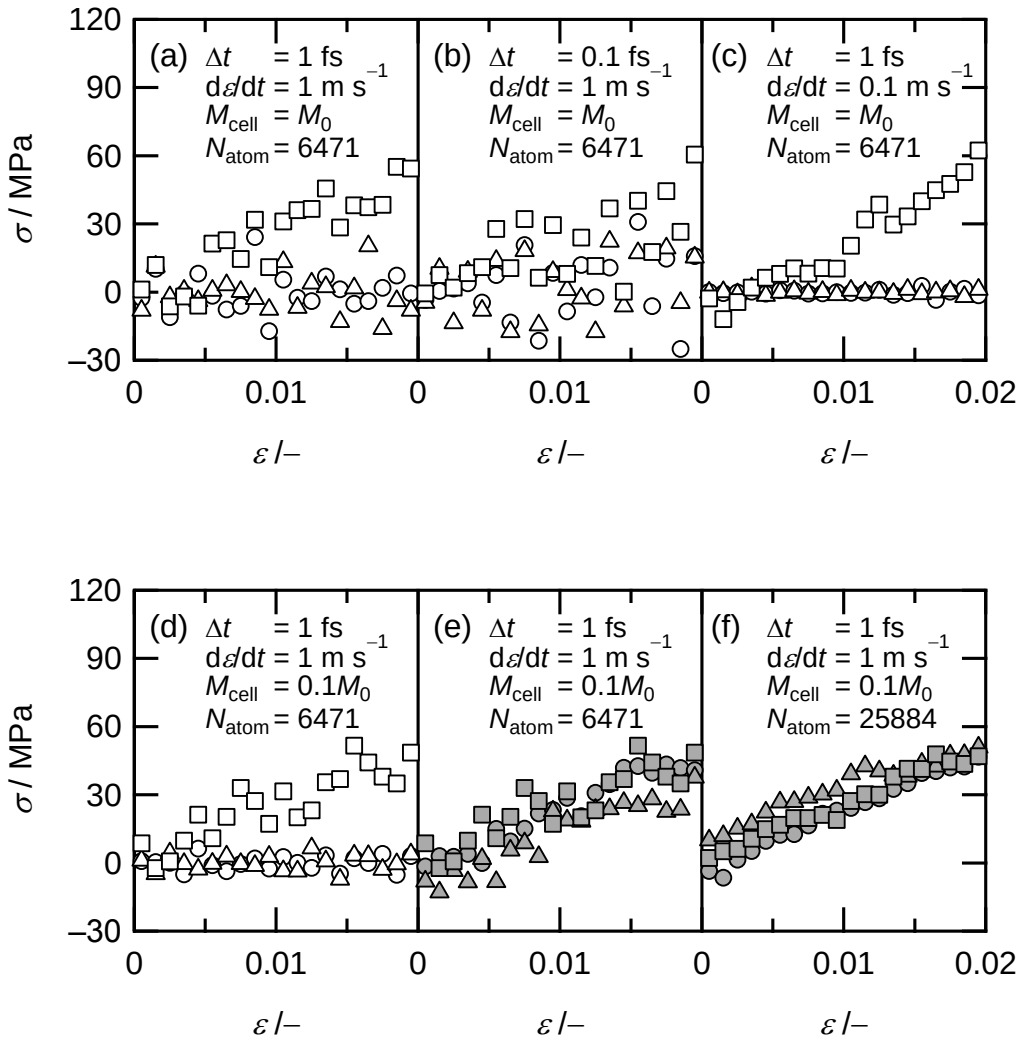

Figure 2.6 Change in the stress of a structure with $D = 0.92$ during uniaxial elongations: Open circle, σ_x; Open triangle, σ_y; Open square, σ_z; Filled circle, $\sigma_x - (\sigma_y + \sigma_z)/2$; Filled triangle, $\sigma_y - (\sigma_z + \sigma_x)/2$; Filled square, $\sigma_z - (\sigma_x + \sigma_y)/2$. Investigated simulation conditions and numbers of atoms in a unit cell are described in the figures.

structure during the uniaxial elongation along the *z*-axis (D = 0.92, T = 300 K, and P = 0.1 MPa). The elongations were performed to ε of 0.02. As seen in Figure 2.6a, there was a large fluctuation in σ_x and σ_y when Δt was 1 fs, $d\varepsilon/dt$ was 1 m s^{-1}, and M_{cell} was M_0, where M_0 represents the sum of the atomic mass in a unit cell. This fluctuation did not diminish when Δt was decreased to 0.1 fs, as shown in Figure 2.6b, but clearly settled down when $d\varepsilon/dt$ or M_{cell} was decreased by a factor of 0.1, as shown in Figures 2.6c and 2.6d. These results indicate that when M_{cell} was M_0, deformation of the heavy cell along the *x*- and *y*-axes in response to the external pressure proceeded slowly such that it could not follow a uniaxial deformation to the *z*-axis when $d\varepsilon/dt$ was 1 m s^{-1}, as shown in Figures 2.6a and 2.6b, but could follow a slow uniaxial deformation to the *z*-axis when $d\varepsilon/dt$ was 0.1 m s^{-1}, as shown in Figure 2.6c. When M_{cell} was $0.1M_0$, the deformation of the light cell along the *x*- and *y*-axes proceeded faster in response to the external pressure such that it followed uniaxial deformation to the *z*-axis when $d\varepsilon/dt$ was 1 m s^{-1}, as shown in Figure 2.6d. Finally, the elongation conditions Δt = 1 fs, $d\varepsilon/dt$ = 1 m s^{-1}, and $M_{cell} = 0.1M_0$ were chosen for the following investigations of elongations to ε of 0.03 in consideration of the calculation costs, where decreasing $d\varepsilon/dt$ by a factor of 0.1 requires a 10-fold longer calculation time than decreasing M_{cell} by a factor of 0.1.

2.2.4.2 Structural Isotropy

Figure 2.6e shows the change in stress (σ) of the same structure evaluated in the proceeding subsection during uniaxial elongations along the *x*-, *y*-, and *z*-axes using the same simulation conditions used in Figure 2.6d, except for the elongation direction. Here σ denotes the stress parallel to the elongation direction subtracted by the average stress perpendicular to the elongation direction, that is, $\sigma = \sigma_z - (\sigma_x + \sigma_y)/2$ for the elongation along the *z*-axis. As seen in this figure, the three stress and strain curves did not superimpose onto a single curve. This result indicates that structural isotropy is insufficient, probably owing to the small system size of a unit cell (i.e., N_{atom} = 6471). The system size dependence on

the structural isotropy was investigated with a unit cell that was four times larger (i.e., N_{atom} of 25884 and D = 0.92), which was prepared by the cross-linking reactions of 200 linear polymers using the same procedures described in the "Cross-linked Polymer Structure Modeling" section. Figure 2.6f shows the result of this large cell. The superposition of the three stress and strain curves onto a single curve was improved but still not optimal, which indicates that structural isotropy can be diminished by using a larger system, but an even larger cell (i.e., $N_{atom} > 10^5$) might be required to obtain an isotropic cross-linked structure with an optimal superposition of the three stress and strain curves. In this study, however, cross-linked structures prepared from 50 polymers were used in the subsequent studies and three uniaxial elongations along the *x*-, *y*-, and *z*-axes were performed for each of the 20 initial structures for each D to obtain sufficient static data, instead of enlarging the system size, which requires excessive calculation costs both in terms of the molecular modeling and uniaxial elongations.

2.3 Results and Discussion

The uniaxial elongations of cross-linked structures were performed to ε of 0.03 (T = 300 K, P = 0.1 MPa, Δt = 1 fs, $d\varepsilon/dt$ = 1 m s^{-1}, and $M_{cell} = 0.1M_0$) in the NPT ensemble using the Parrinello–Rahman and Nosé–Hoover algorithms, where the values of r_{cutoff} in the calculation of U_Q were 14.4–14.8 Å depending on N_{atom} and V_{cell}. It should be mentioned that ε of 0.03 is a very large deformation for typical phenolic resins.[47] At this temperature, all structures were in a glassy state, as confirmed in the "Glass-Transition Temperature" section. The elongations along the *x*-, *y*-, and *z*-axes were performed with 20 different initial structures for each D. Results were evaluated as an average of 60 elongations for each D, and errors were calculated with 95% confidence intervals.

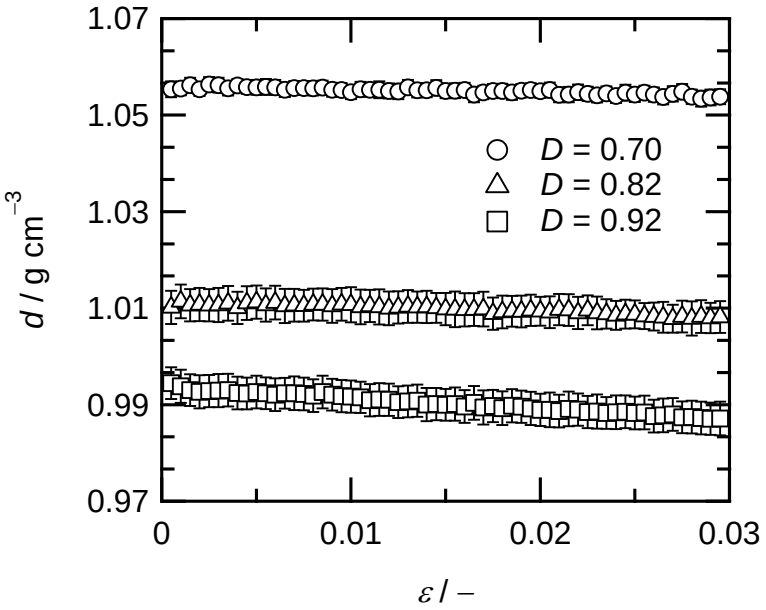

Figure 2.7 Change in density during uniaxial elongation: Circle, D = 0.70; Triangle, D = 0.82; Square, D = 0.92.

2.3.1 Density and Poisson's Ratio

Figure 2.7 shows the change in the density during uniaxial elongation. The values of Poisson's ratio (v) given by

$$\frac{\Delta V_{\text{cell}}}{V_{\text{cell}}} = (1+\varepsilon)^{1-2v} - 1 \tag{2.8}$$

were estimated to be 0.47, 0.46, and 0.37 for the structures with D equal to 0.70, 0.82, and 0.92, respectively. These results show that the cross-linking lowers d and v. This could be explained by changes in local structures. The methylene cross-linker increased the distance between two bridged phenols, which lowered d and reduced the motion around these phenols (i.e., rubbery segments in the structure), which lowered v. Thus, segmental motions existed for the structures in which D was 0.70 and 0.82, although they were confirmed to be in a glassy state at 300 K, as shown in Figures 2.5b and 2.5c, respectively.

2.3.2 Stress and Strain Curves

Figure 2.8 shows the stress and strain curves. All curves can be regarded as straight lines, which indicates that elastic deformations occurred for all structures within the ε range of 0–0.03. As seen in this figure, the stress and strain curves are clearly dependent on D. The values of Young's modulus (E) corresponding to the slopes of the stress and strain curves, were estimated to be 1.3, 1.8, and 2.7 GPa for structures with D equal to 0.70, 0.82, and 0.92, respectively, which demonstrates a clear dependence on D. Note that these values are smaller than the typical experimental value (i.e., E = 5–6 GPa),[47] which might be due to the nonquantitative nature of the MD simulations using generic force field parameters that have not been fully optimized for the phenolic resins as discussed in section 2.2.3; however, the order of magnitude agrees with the experimental values.

The influence of the degree of cross-linking on stress was examined from the standpoints of (i) the effect of electrostatic interactions including the

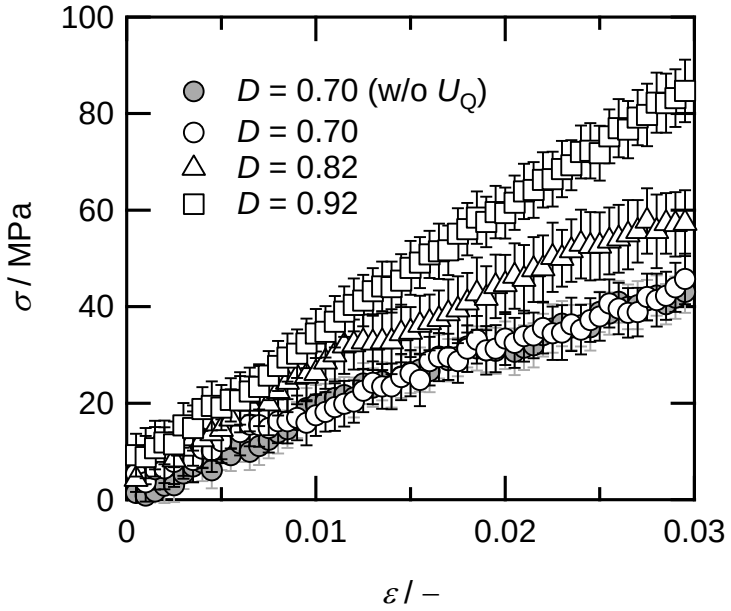

Figure 2.8 Stress and strain curves: Circle, D = 0.70; Triangle, D = 0.82; Square, D = 0.92. Open symbol calculated with U_Q. Filled symbol calculated without U_Q.

hydrogen-bonding interactions associated with the hydrogens and oxygens of the hydroxyl groups in the phenolic resins, (ii) the change in the distributions of bonding potential energies (i.e., U_B, U_A, and U_T) before and after uniaxial elongations, and (iii) the change in the potential energies during elongation.

2.3.3 Effect of Electrostatic Interactions

A high number density of hydroxyl groups is a structural feature of phenolic resins. The hydrogen-bonding interactions would be the dominant factor of U_Q in the system whose chemical structure is shown in Figure 2.1c. To evaluate the effect of electrostatic interactions on stress, uniaxial elongations of the structure with D equal to 0.70 were performed again with the same simulation conditions except that U_Q was not calculated. The result is shown in Figure 2.8 (filled circles). The stress and strain curves for structures with and without calculations for U_Q were sufficiently superimposed onto a single curve with errors, which indicates that electrostatic interactions including hydrogen-bonding interactions would not be the major influence on the stress of the uniaxial elongation of cross-linked phenolic resins.

2.3.4 Distribution of the Bonding Potential Energies

The uniaxial elongation of bulk polymers could be accompanied by stretching of bond lengths, bending of bond angles, and rotation of torsion angles, which may cause changes in the distributions of U_B, U_A, and U_T.[52] Thus, the change in the distribution of potential energies resulting from the uniaxial elongation would provide insights into understanding structural changes. Figure 2.9 shows distributions of the bonding potential energies when ε is 0 and 0.03, where N_{node} denotes the number of potential nodes, and the investigated bonding potentials were those resulting from the interactions of two, three, and four carbons for U_B, U_A, and U_T, respectively. The distribution of these potential energies was dependent on D owing to the differences in N_{node} for each potential but independent of ε. These results indicate that the uniaxial elongation to ε of

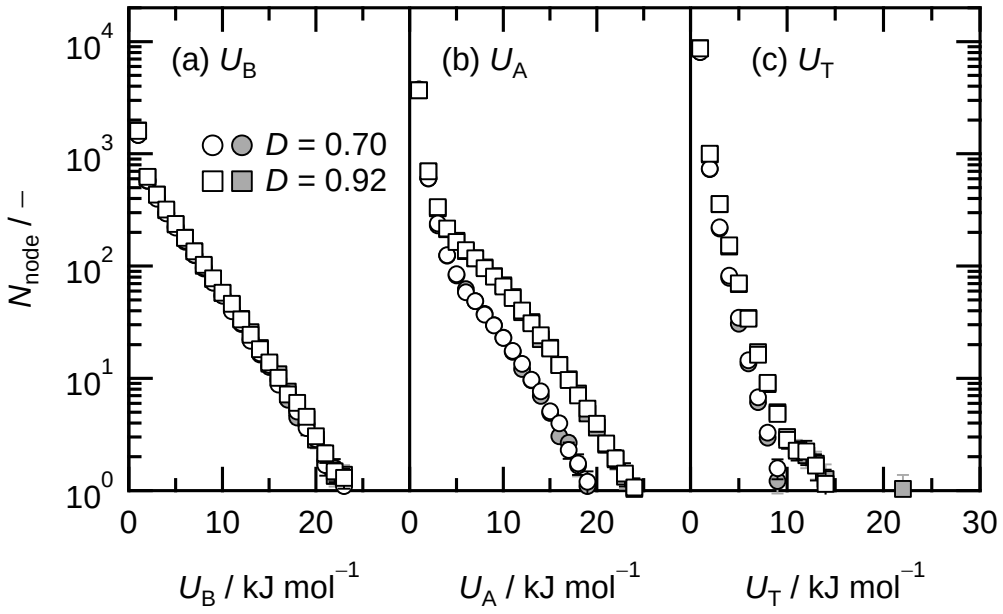

Figure 2.9 Distribution of the bonding potential energy: (a) U_B; (b) U_A; (c) U_T. Circle, D = 0.70; Square, D = 0.92; Open symbol, ε = 0; Filled symbol, ε = 0.03.

0.03 does not cause a significant change in the distribution of the bonding potential energies.

To investigate the distribution of U_B more precisely, the distribution was decomposed into the angle of the bond vector with respect to the elongation direction (θ_{bond}) in the range of 0°–90°. The results are shown in Figures 2.10a–d for structures with D equal to 0.70 and 0.92, in which N_{node} was corrected to a solid angle (Ω) given by

$$\Omega = \int 2\pi \sin\theta_{bond} \, d\theta_{bond} . \tag{2.9}$$

As seen in these figures, the distribution of the high-energy nodes was not biased toward a direction parallel to the elongation direction (i.e., $\theta_{bond} < 30°$), and was independent of θ_{bond} and ε. These results indicate that bonds parallel to the elongation direction were not uniquely stretched and that the uniaxial elongation for ε = 0–0.03 did not cause a significant change in the distribution of U_B.

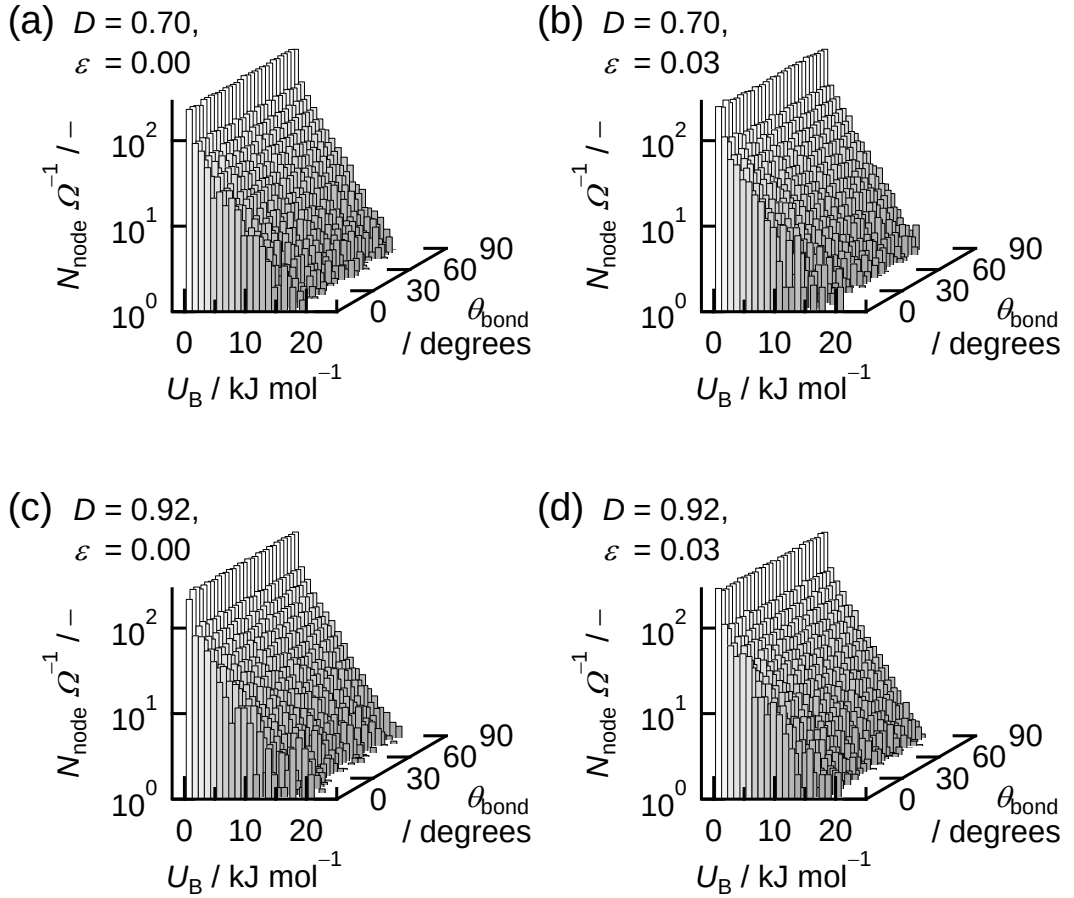

Figure 2.10 Distribution of U_B: (a) D = 0.70 and ε = 0; (b) D = 0.70 and ε = 0.03; (c) D = 0.92 and ε = 0; (d) D = 0.92 and ε = 0.03.

2.3.5 Change in the Potential Energy

Figure 2.11 shows the change in the potential energies during the uniaxial elongation. Considering the values of the potential energies (i.e., 1.5×10^4, 1.8×10^4, 1.4×10^4, 2.2×10^4, and -3.1×10^4 kJ mol^{-1} for U_B, U_A, U_T, U_{VDW}, and U_Q, respectively, for the structure with D equal to 0.92), the variations were slight. This agrees with the results in Figures 2.9 and 2.10 showing a distribution of the bonding potential energies that was nearly unchanged. However, as seen in Figure 2.11, the behavior of the potential energy change shows a clear tendency toward a dependence on the degree of cross-linking.

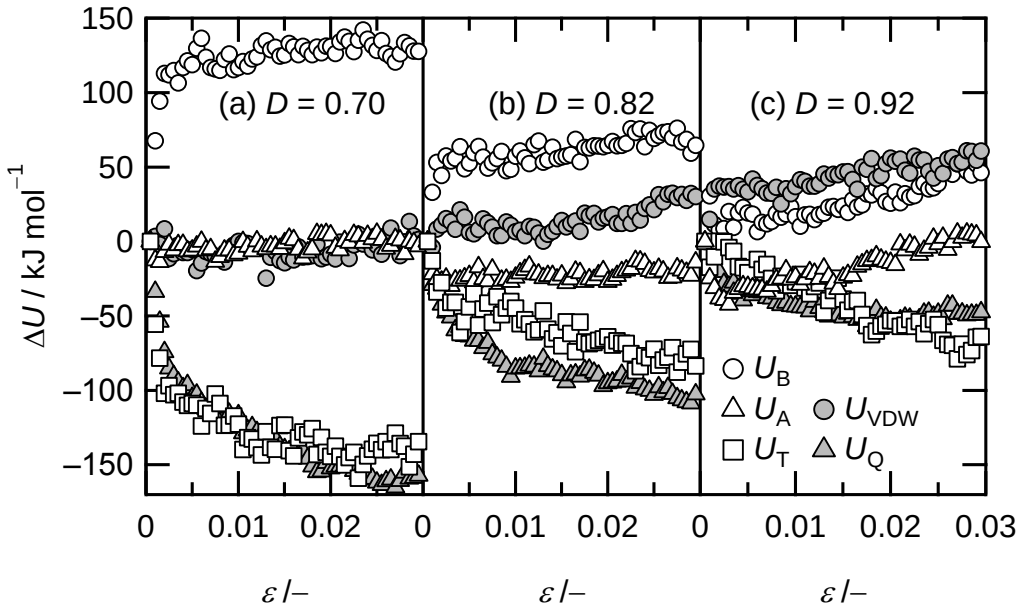

Figure 2.11 Change in the potential energy: (a) D = 0.70; (b) D = 0.82; (c) D = 0.92. Open circle, U_B; Open triangle, U_A; Open square, U_T; Filled circle, U_{VDW}; Filled triangle, U_Q.

At the initial stage of the elongation (ε = 0–0.002), there were dramatic changes (100 kJ mol^{-1}) to $|\Delta U|$ in U_B, U_T, and U_Q for the structure with D equal to 0.70, which were diminished by increasing D. In contrast, there were small but clear changes (40 kJ mol^{-1}) to $|\Delta U|$ in U_A and U_{VDW} for the structure with D equal to 0.92, which were diminished by decreasing D. These results indicate that the cell deformation was absorbed by the rotation of torsion angles for structures with a low-degree of cross-linking. This conformational change in the torsion angles caused the bond lengths that existed around the rotating segments to stretch, which resulted in the increase in U_B. In addition, the change in the distance between atoms around the rotating segments, leading to a more electrostatically stable distance, resulted in the decrease in U_Q. For structures with a high-degree of cross-linking, the conformational change in torsion angles was suppressed by the

cross-links and the deformation was first absorbed by the bending of unstable bond angles to achieve stable angles, which resulted in the decrease in U_A. This conformational change caused the distance between atoms that existed around the bending segments to shorten because the segmental motion needed to maintain a stable distance between atoms was suppressed by the highly cross-linked structures, which resulted in the increase in U_{VDW}.

After the initial stage of the elongation, the decreases in U_T and U_Q were observed for all structures, which indicates that cell deformation was mainly absorbed by the rotation of the torsion angles. This conformational change in the torsion angles was accompanied by a change in the distance between the atoms that existed around the rotating segments to achieve a more electrostatically stable distance, which resulted in the decrease in U_Q as observed at the initial stage for the structure with D equal to 0.70. For the structure with D equal to 0.92, the increases in U_B, U_A, and U_{VDW} after the initial stage of the elongation were clearly observed, which is probably because the rotation of torsion angles changed the conformation of neighboring segments (i.e., stretching bond lengths, bending bond angles, and reducing the distance between atoms), and these conformational changes could not be relaxed owing to the highly cross-linked nature of the structures.

At 300 K, all structures were confirmed to exist in a glassy state, as shown in Figures 2.5b–d; however, these results indicate that there would be segmental motions probably at the region around the linear and terminal phenols in the cross-linked structure. These motions could be a key factor contributing to the stress response in the uniaxial elongation of cross-linked phenolic resins.

2.4 Conclusions

Cross-linked phenolic resins were studied by atomistic MD simulations. Cross-linked structures consisting of a network of three functional phenols and two functional methylenes with D equal to 0.70, 0.82, and 0.92 were prepared by

the cross-linking reactions of 50 linear novolac-type phenolic resins that have an all-*ortho* configuration and the degree of polymerization of 9 in a unit cell under 3D periodic boundary conditions. An increase in D accompanied the increase in T_g, which was determined from the change in the slope of V_{sp} as a function of T. This indicates that segmental motions were suppressed by the cross-links. The uniaxial elongations of the cross-linked structures were performed at 300 K, the temperature at which all cross-linked structures were in a glassy state below T_g. The calculated values of Poisson's ratio were 0.47, 0.46, and 0.37 for structures with D equal to 0.70, 0.82, and 0.92, respectively, which indicates that there were segmental motions in the local structures that were reduced by the cross-links. In the uniaxial elongations, elastic deformations occurred for all cross-linked structures in the ε range of 0–0.03, which was confirmed by the straight-line relationships between σ and ε. Young's modulus was estimated to be 1.3, 1.8, and 2.7 GPa for structures with D equal to 0.70, 0.82, and 0.92, respectively, which shows clear dependence on D. The electrostatic interactions including hydrogen-bonding interactions were not expected to be the major factor regulating the stress of the uniaxial elongation of the cross-linked phenolic resins. Uniaxial elongation to ε of 0.03 did not cause a significant change in the distribution of bonding potential energies. On the other hand, the change in the potential energies owing to the uniaxial elongation indicated that cross-links suppressed local segmental motions in the cross-linked structures, probably at the region around the linear and terminal phenols. As a result, it was found that an increase in the degree of cross-linking accompanied the decrease in Poisson's ratio and increase in Young's modulus. DREIDING force field was applied in this study in terms of the generality of potential parameters that are widely applicable to organic materials. The optimization of the force field parameters for the phenolic resins to minimize the deviation between experimental and calculated values of density and Young's modulus is the subject of future investigation.

2.5 References

1 K. Binder, *Monte Carlo and Molecular Dynamics Simulations in Polymer Science*, Oxford University Press, Oxford, 1995.

2 K. Kremer and F. Müller-Plathe, *Mol. Simulat.*, 2002, **28**, 729–750.

3 B. L. Schürmann and L. Vogel, *J. Mater. Sci.*, 1996, **31**, 3435–3440.

4 A. R. Pawloski, J. A. Torres, P. F. Nealey and J. J. de Pablo, *J. Vac. Sci. Technol. B*, 1999, **17**, 3371–3378.

5 S. S. Choi, *Polym. Adv. Technol.*, 2001, **12**, 567–573.

6 D. E. Jiang, A. C. T. van Duin, W. A. Goddard and S. Dai, *J. Phys. Chem. A*, 2009, **113**, 6891–6894.

7 T. G. Desai, J. W. Lawson and P. Keblinski, *Polymer*, 2011, **52**, 577–585.

8 B. Arman, Q. An, S. N. Luo, T. G. Desai, D. L. Tonks, T. Çağın and W. A. Goddard III, *J. Appl. Phys.*, 2011, **109**, 013503.

9 M. J. Stevens, *Macromolecules*, 2001, **34**, 1411–1415.

10 M. J. Stevens, *Macromolecules*, 2001, **34**, 2710–2718.

11 C. D. Lorenz, M. J. Stevens and R. P. Wool, *J. Polym. Sci., Part B: Polym. Phys.*, 2004, **42**, 3333–3343.

12 M. Tsige, C. D. Lorenz and M. J. Stevens, *Macromolecules*, 2004, **37**, 8466–8472.

13 M. Tsige and M. J. Stevens, *Macromolecules*, 2004, **37**, 630–637.

14 D. Mukherji and C. F. Abrams, *Phys. Rev. E*, 2008, **78**, 050801(R).

15 D. Mukherji and C. F. Abrams, *Phys. Rev. E*, 2009, **79**, 061802.

16 T. Ikeno, M. Tsubuku, M. Katagiri and T. Tsujimoto, *Chem. Lett.*, 2011, **40**, 309–311.

17 P. H. Lin, S. C. Kohale and R. Khare, *J. Phys. Chem. B*, 2011, **115**, 12348–12355.

18 I. Yarovsky and E. Evans, *Polymer*, 2002, **43**, 963–969.

19 J. Mijović and H. Zhang, *J. Phys. Chem. B*, 2004, **108**, 2557–2563.

20 C. Wu and W. Xu, *Polymer*, 2006, **47**, 6004–6009.

21 H. B. Fan and M. M. F. Yuen, *Polymer*, 2007, **48**, 2174–2178.

22 P. V. Komarov, Y. T. Chiu, S. M. Chen, P. G. Khalatur and P. Reineker, *Macromolecules*, 2007, **40**, 8104–8113.

23 V. Varshney, S. S. Patnaik, A. K. Roy and B. L. Farmer, *Macromolecules*, 2008, **41**, 6837–6842.

24 T. C. Clancy, S. J. V. Frankland, J. A. Hinkley and T. S. Gates, *Polymer*, 2009, **50**, 2736–2742.

25 P. H. Lin and R. Khare, *Macromolecules*, 2009, **42**, 4319–4327.

26 V. Varshney, S. S. Patnaik, A. K. Roy and B. L. Farmer, *Polymer*, 2009, **50**, 3378–3385.

27 S. Yu, S. Yang and M. Cho, *Polymer*, 2009, **50**, 945–952.

28 C. Li and A. Strachan, *Polymer*, 2010, **51**, 6058–6070.

29 L. J. Abbott and C. M. Colina, *Macromolecules*, 2011, **44**, 4511–4519.

30 N. Nouri and S. Ziaei-Rad, *Macromolecules*, 2011, **44**, 5481–5489.

31 H. Liu, M. Li, Z. Y. Lu, Z. G. Zhang, C. C. Sun and T. Cui, *Macromolecules*, 2011, **44**, 8650–8660.

32 A. Bandyopadhyay, P. K. Valavala, T. C. Clancy, K. E. Wise and G. M. Odegard, *Polymer*, 2011, **52**, 2445–2452.

33 C. Li and A. Strachan, *Polymer*, 2011, **52**, 2920–2928.

34 J. Choi, S. Yu, S. Yang and M. Cho, *Polymer*, 2011, **52**, 5197–5203.

35 X. Y. Song, Y. Sun, X. R. Wu and F. L. Zeng, *Comp. Mater. Sci.*, 2011, **50**, 3282–3289.

36 D. C. Doherty, B. N. Holmes, P. Leung and R. B. Ross, *Comput. Theor. Polym. Sci.*, 1998, **8**, 169–178.

37 J. S. Bermejo and C. M. Ugarte, *Macromol. Theor. Simul.*, 2009, **18**, 259–267.

38 J. S. Bermejo and C. M. Ugarte, *Macromol. Theor. Simul.*, 2009, **18**, 317–327.

39 D. R. Heine, G. S. Grest, C. D. Lorenz, M. Tsige and M. J. Stevens, *Macromolecules*, 2004, **37**, 3857–3864.

40 T. Yamagishi, T. Nakatogawa, M. Ikuji, Y. Nakamoto and S. Ishida, *Angew.*

Makromol. Chem., 1996, **240**, 181–186.

41 OCTA Home Page. http://octa.jp/index.html.

42 C. I. Bayly, P. Cieplak, W. D. Cornell and P. A. Kollman, *J. Phys. Chem.*, 1993, **97**, 10269–10280.

43 Amber Home Page. http://ambermd.org.

44 S. L. Mayo, B. D. Olafson and W. A. Goddard III, *J. Phys. Chem.*, 1990, **94**, 8897–8909.

45 M. P. Allen and D. J. Tildesley, *Computer Simulation of Liquids*, Clarendon Press, Oxford, 1987.

46 D. Fincham, *Mol. Simulat.*, 1994, **13**, 1–9.

47 A. Gardziella, L. A. Pilato and A. Knop, *Phenolic Resins: Chemistry, Applications, Standardization, Safety and Ecology*, 2nd completely rev. edn., Springer, Berlin, 1999.

48 H. J. C. Berendsen, J. P. M. Postma, W. F. Vangunsteren, A. DiNola and J. R. Haak, *J. Chem. Phys.*, 1984, **81**, 3684–3690.

49 W. G. Hoover, *Phys. Rev. A*, 1985, **31**, 1695–1697.

50 H. C. Andersen, *J. Chem. Phys.*, 1980, **72**, 2384–2393.

51 M. Parrinello and A. Rahman, *J. Appl. Phys.*, 1981, **52**, 7182–7190.

52 K. Yashiro, T. Ito and Y. Tomita, *Int. J. Mech. Sci.*, 2003, **45**, 1863–1876.

Chapter 3

Dynamic Light Scattering and Small-Angle Neutron Scattering Studies on Phenolic Resin Solutions

3.1 Introduction

To elucidate inhomogeneity of phenolic resins, we focus on understanding the inhomogeneity of soluble oligomers, insoluble gels, and infusible cured resins by scattering techniques such as dynamic laser-light scattering (DLS), small-angle neutron and X-ray scattering (SANS and SAXS, respectively). These methods have proven to be powerful tools in elucidating the inhomogeneity of gel networks.[1–3] For studies of thermosetting resins, the applications of scattering techniques have typically included the analyses of the phase separation of thermosetting and thermoplastic polymer blends,[4–6] aggregation and distribution of nanometer-sized reinforcing fillers in nanocomposites,[7–9] pore structure of carbon.[10–13] However, only a few studies have been reported on the inhomogeneity of thermosetting resin involving these methods.[14–18]

For the structural analysis of thermosetting resins, it is necessary to understand the polymer conformation before it becomes insoluble and infusible because of cross-linking. Thus, many structural analyses were performed using soluble phenolic resins with lower molecular weight or lower degree of

cross-linking. These studies have employed techniques such as NMR to analyze the chemical structure, mass spectroscopy and gel permeation chromatography (GPC) to determine molecular weight, and light scattering to analyze polymer conformation in solution to understand not only the nature of soluble phenolic resin but also the curing behavior and property of the cross-linked resin.[19,20] Among these studies, one of the major topics is the evaluation of the scaling exponent (a) in the Mark–Houwink–Sakurada equation given by $[\eta] = KM^a$, where $[\eta]$, K, and M denote intrinsic viscosity, constant, and molecular weight, respectively.[21–26] According to these studies of the polymer conformation in dilute solution, phenolic resins have a values of 0.2–0.5 in good solvents, such as acetone and THF. This value is smaller than 0.5 for a linear Gaussian chain, which is the result of a compact sphere-like conformation in good solvents. We should note that these studies were achieved using phenolic resins with narrow molecular-weight distribution (i.e., polydispersity index (M_w/M_n) < 1.2), which were obtained by a careful solution fractionation technique using a solvent/nonsolvent system.

In this study, to elucidate the solution properties of unfractionated phenolic resins with original molecular weight distribution, which was prepared by the polycondensation of phenol and formaldehyde, the hydrodynamic radius in 1 vol% solution and the correlation length in 10 vol% solution were evaluated as a function of molecular weight, using DLS, SANS, and GPC.

3.2 Experimental

3.2.1 Materials

Phenol (PhOH), formaldehyde (HCHO, 37 wt% aqueous solution), oxalic acid (OX, anhydrous), acetone and tetrahydrofuran (THF) were purchased from Wako Pure Chemical Industries, Ltd., Japan. Tetrahydrofuran-d_8 (THF-d_8) was purchased from C/D/N isotopes, Inc., Canada. All materials were used without further purification.

3.2.2 Sample Preparation

Phenolic resins were prepared from PhOH and HCHO using OX as a catalyst. A mixture of PhOH, HCHO aq., and OX in a flask, open to air, was stirred at 100 °C (reflux) for 330 min. An aliquot of the reaction mixture was collected and dried under vacuum at room temperature for GPC, DLS, and SANS analyses. Sample ID, corresponding initial molar ratio of $[PhOH]_0/[HCHO]_0/[OX]_0$, concentration of HCHO in aqueous solution, and reaction time are listed in Table 3.1.

3.2.3 GPC

GPC experiments were performed on a Tosoh HLC-8120 system equipped with six poly(styrene-*co*-divinylbenzene) gel columns (TSKgel SuperHZM-M, $HZ3000_{XL}$, $HZ2000_{XL}$, $HZ2000_{XL}$, $HZ2000_{XL}$, and $HZ1000_{XL}$) and a refractive index detector. THF at 40 °C was used as the eluent. The *z*-average molecular weight (M_z), the weight-average molecular weight (M_w), and the number-average molecular weight (M_n), were calculated with a calibration line that was obtained by fitting the peak molecular weights of 18 polystyrene (PSt) standards using a cubic function. The peak molecular weights of PSt standards were 1.09×10^6, 7.06×10^5, 3.55×10^5, 1.90×10^5, 9.64×10^4, 3.79×10^4, 1.81×10^4, 9100, 5970, 2630, 994, 786, 682, 578, 474, 370, 266, and 162 g mol^{-1}, and the polymer concentration of the injection solution was 0.20 mg mL^{-1}. The polymer solution was filtered through a 0.45 μm filter (Tosoh H-13-5) before injection into the chromatograph. GPC results of M_z, M_w, and M_w/M_n of the investigated polymers are listed in Table 3.1. Note that, the molecular weight of phenol (94.11 g mol^{-1}) was estimated to be M_w of 176 g mol^{-1} and M_n of 155g mol^{-1} owing to the broadening of the GPC signal at longer retention time. In this study, however, molecular weights were estimated on the basis of the calibration line and further desmearing procedures were not applied for the smeared signals.

Table 3.1 Sample Preparation and Molecular Weight[a]

Sample	$[PhOH]_0/[HCHO]_0/[OX]_0$[b]	Reaction time / min	M_z / g mol^{-1}	M_w / g mol^{-1}	M_w/M_n
NV0901a	1/0.9/0.01[c]	195	2630	1200	2.2
		225	4390	1630	2.8
		255	6580	2230	3.2
		315	14700	4420	4.7
NV0905a	1/0.9/0.05[c]	135	3530	1370	2.5
		165	9820	3080	4.0
		195	17600	5330	5.6
		225	26900	7730	7.2
		255	37600	10300	8.8
		315	68300	16100	12.0
NV0910a	1/0.9/0.1[c]	75	5320	1940	3.0
		135	9750	3260	4.1
		165	22300	6780	6.7
		195	39500	11200	9.6
		225	66600	15600	13.2
		255	121000	21800	17.4
		315	491000	33400	26.0
NV1201a	1/1.2/0.01[c]	195	4170	1610	2.8
		225	9270	2990	4.1
		255	18900	5730	6.2
NV1501a	1/1.5/0.01[c]	165	2870	1190	2.3
		195	12300	3750	4.5
NV0901b	1/0.9/0.01[d]	120	7370	2360	3.6
		180	15800	4590	5.7
		240	18200	5090	6.1
		300	22800	6220	7.2
NV0905b	1/0.9/0.05[d]	120	20000	5460	6.2
		180	26000	7160	7.6
		240	29200	7830	8.1
		300	35700	9020	9.0
		330	62300	10900	10.0
NV1201b	1/1.2/0.01[d]	120	8780	2710	3.9
		240	722000	39800	36.4
NV1501b	1/1.5/0.01[d]	120	9430	2870	4.0

[a] Estimated by GPC (THF, PSt). [b] Molar ratio in feed. [c] 22 wt% HCHO aqueous solution was used. [d] 37 wt% HCHO aqueous solution was used.

3.2.4 DLS

DLS experiments were performed on a dynamic/static compact goniometer DLS/SLS-5000 (ALV, Langen, Germany). A He–Ne laser with a power of 22 mW emitting polarized light at a wavelength of 632.8 nm was used as the incident beam. DLS measurements were conducted at 25 °C with an acquisition time of 60 s. The scattering angle was 90°. The polymer concentration was 0.01 mg mL^{-1}. The polymer solution was filtered through a 0.45 μm filter (Tosoh H-13-5) as in the GPC experiments. Acetone and THF were used as solvents. The time–intensity correlation function ($g^{(2)}(\tau)$) was obtained as a function of the decay time (τ), which is linked to the scattering electric field correlation function ($g^{(1)}(\tau)$),

$$g^{(2)}(\tau) = 1 + \beta \left| g^{(1)}(\tau)^2 \right|, \tag{3.1}$$

where β denotes the instrumental coherence factor close to unity.[27] Here $g^{(1)}(\tau)$ is described by the decay rate distribution function ($G(\Gamma)$),

$$g^{(1)}(\Gamma) = \int_0^\infty G(\Gamma) \exp(-\Gamma\tau)\, \mathrm{d}\tau, \tag{3.2}$$

where Γ denotes the characteristic decay rate which is an inverse of the characteristic decay time (Γ^{-1}). $G(\Gamma)$ was calculated from an inverse Laplace transform of $g^{(2)}(\tau)$ on the basis of eqs 3.1 and 3.2.[27] In this study, the constrained regularization program, CONTIN, supplied with the correlator was used to obtain $G(\Gamma)$ from $g^{(2)}(\tau)$.[28] If the dynamics of the system is diffusive, Γ is related to the translational diffusion coefficient (D),

$$\Gamma = Dq^2. \tag{3.3}$$

Here q denotes the magnitude of the scattering vector given by

$$q = \frac{4\pi n_0}{\lambda} \sin(\theta/2), \tag{3.4}$$

where n_0, λ, and θ denote the refractive index of the solvent, the wavelength of light in vacuum, and the scattering angle, respectively. The hydrodynamic radius (R_h) of the polymer was then obtained by the Stokes–Einstein equation for dilute

polymer solutions,

$$R_h = \frac{k_B T}{6\pi\eta D}, \tag{3.5}$$

where k_B, T, and η denote Boltzmann's constant, absolute temperature, and solvent viscosity, respectively.

Figures 3.1a and 3.1b show the solvent dependencies of $g^{(2)}(\tau)-1$ and the distribution of R_h, respectively, of phenolic resin with M_w of 5480 and M_w/M_n of 5.8. In this study, acetone and THF, which are typically good solvents for soluble phenolic resins, were used as solvents. As shown in these figures, $g^{(2)}(\tau)-1$ decays faster in acetone than in THF. This agrees with the order of η, 0.308 mPa·s for acetone and 0.465 mPa·s for THF at 25 °C,[29] which affects the rate of translational diffusion. It was confirmed, however, that the polymer has the same distribution of R_h in both solvents after correction of η and n_0 according to eqs 3.3–3.5. Thus, we employed the data for R_h obtained by DLS experiments in acetone solution for further analysis in conjunction with the molecular weight values obtained from GPC experiments in THF solution. In the following DLS measurements, acetone was used as a solvent rather than THF because of the larger deviation in n_0 between phenol and the solvent,[30] which results in a reasonable DLS intensity even for the lower molecular weight polymer.

3.2.5 SANS

SANS experiments were performed on the SANS-U spectrometer belonging to the Institute for the Solid State Physics, the University of Tokyo, which is installed in the Guide Hall of the JRR-3 Research Rector of Japan Atomic Energy Agency in Tokai, Ibaraki, Japan.[31–33] A monochromated cold neutron beam with an average neutron wavelength of 7.0 Å and 10% wavelength distribution was used to irradiate the samples at room temperature. The scattered neutrons were counted by a two-dimensional position detector (2660N, Ordela, USA). The sample-to-detector distances were chosen to be 1 and 4 m, and the collimation length was fixed to 4 m. A polymer solution was placed in a sealed

quartz cell with thicknesses of 2 or 4 mm. THF-d_8 was used as the solvent. The polymer concentration was 120 mg mL^{-1}, which corresponds to 10 vol%

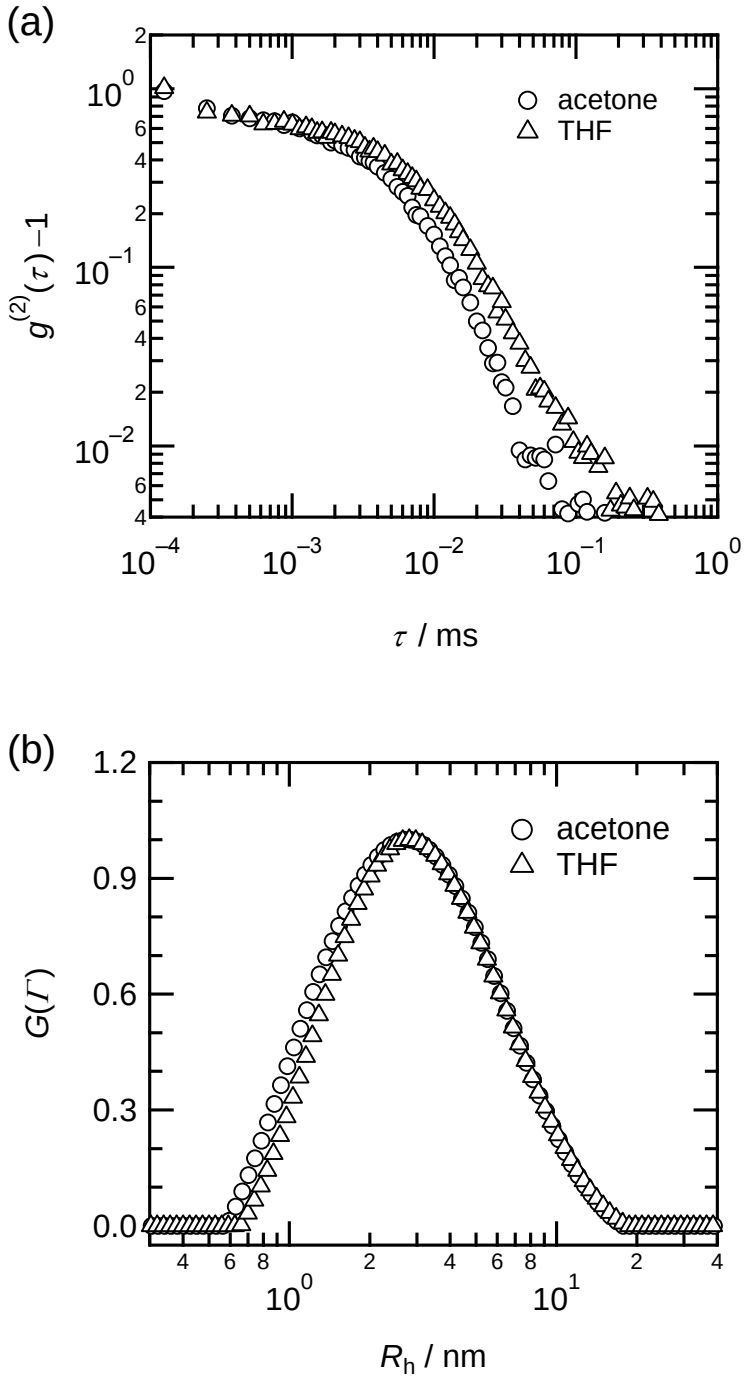

Figure 3.1 (a) Time–intensity correlation functions, and (b) the distribution functions of the hydrodynamic radius of a phenolic resin in acetone and THF at 25 °C.

assuming a polymer density of 1.2 g cm^{-3}. No insoluble part was observed in appearance. After necessary corrections for open beam scattering, transmittance, and detector inhomogeneities, the corrected scattering intensity functions were normalized to the absolute intensity scale using a polyethylene secondary standard.

3.3 Results and Discussion

Figure 3.2 shows the change in GPC chromatograms of NV0910a during polymerization. In GPC, large molecules elute first and small molecules elute later. The peaks at retention times of 29, 27, 26, and 25 min in the figure correspond to unreacted phenol monomer, dimer (bis(hydroxyphenyl)methane), trimer (bis(hydroxyphenylmethyl)phenol), and tetramer, respectively, as shown with arrows. As polymerization proceeds, the size of the polymer increases, which resulted in the shorter retention time seen in Figure 3.2. The molecular weights of the oligomers, obtained by GPC measurements, are listed in Table 3.1 with their different reaction times. Note that the numbers in the sample code indicate the

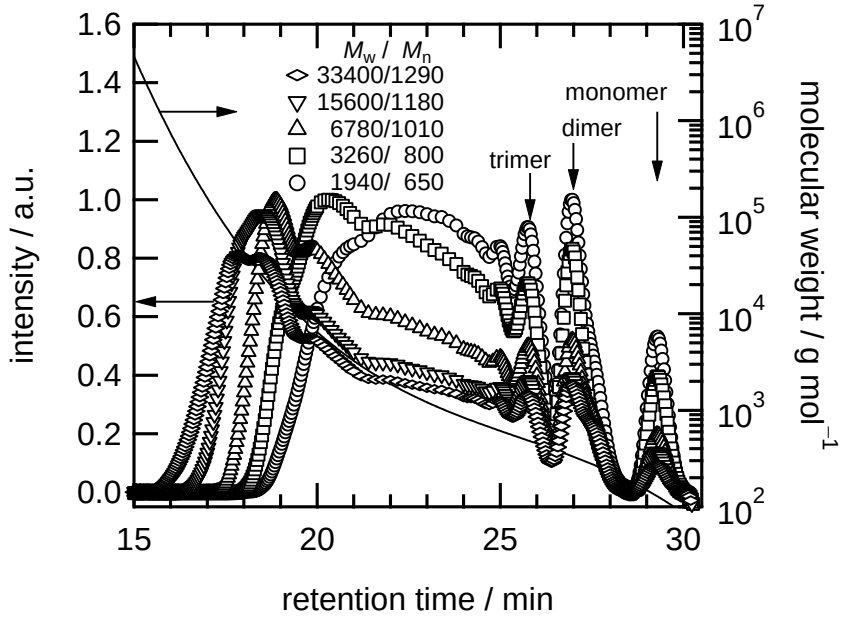

Figure 3.2 The gel permeation chromatograms of NV0910a measured in THF at 40 °C. A solid line represents a calibration line based on PSt standards.

initial molar ratio.

Figures 3.3a and 3.3b show $g^{(2)}(\tau)-1$ and $G(\Gamma)$ of NV0910a with different molecular weights, respectively. As molecular weights increase, $g^{(2)}(\tau)-1$ shifts toward a longer relaxation time. The molecular weight dependence of R_h is

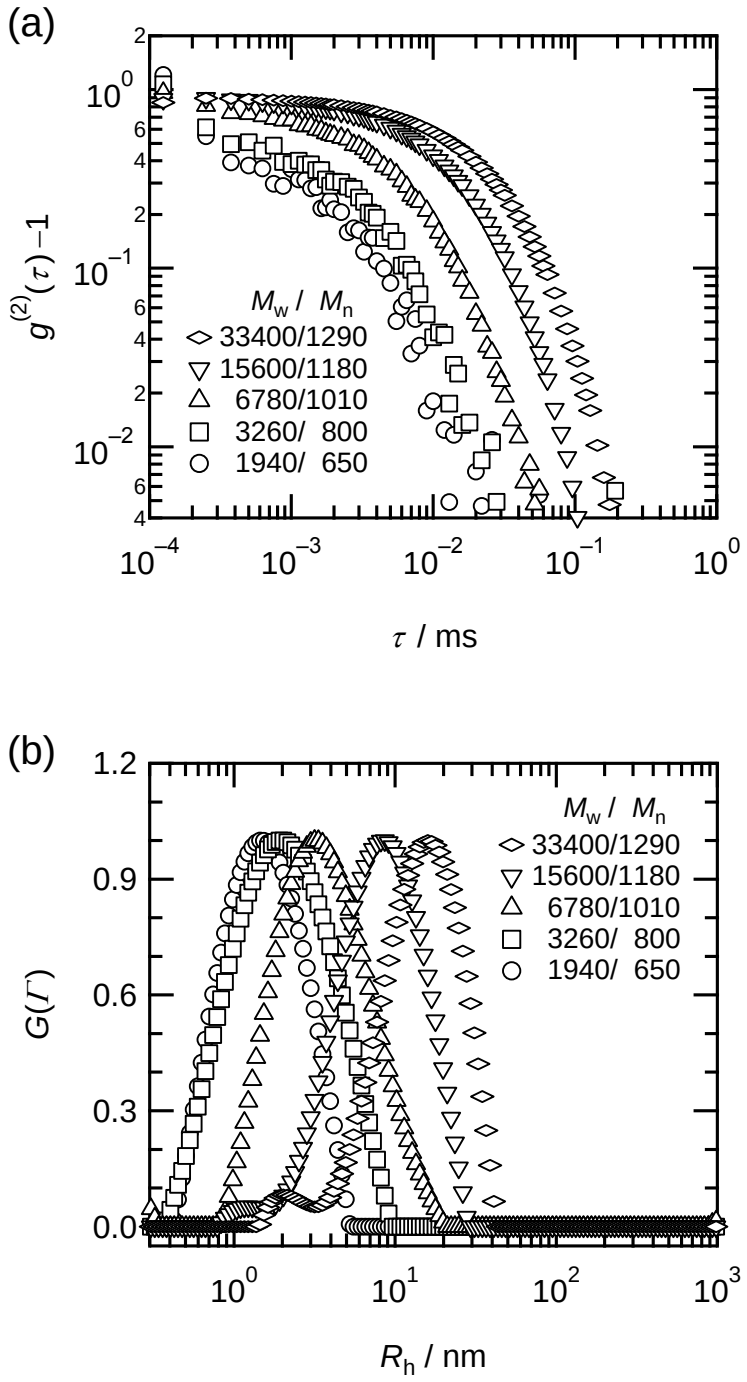

Figure 3.3 (a) Time–intensity correlation functions, and (b) the distribution functions of the hydrodynamic radius of NV0910a in acetone at 25 °C.

clearly observed in Figure 3.3b as a shift of the peak toward a large value of R_h.

All values of R_h were calculated from Γ at the point of the maximum $G(\Gamma)$ and plotted against M_w in Figure 3.4a. As seen in this figure, R_h and M_w exhibited power-law-like behavior, and a slope of 0.95 was obtained. This suggests R_h and M_w of phenolic resins prepared from PhOH, HCHO, and OX obey the power-law relation irrespective of polymerization conditions with the initial molar ratio of $[PhOH]_0/[HCHO]_0$ from 0.9 to 1.5, the concentration of HCHO aqueous solution of 22 and 37 wt%, the molar ratio of catalyst $[OX]_0/[PhOH]_0$ from 0.01 to 0.1, and reaction time dependent on the duration for which the polymer remains soluble.

The obtained exponent of M_w in the power-law relation between R_h and M_w is much larger than those reported in previous studies, 0.2 to 0.5.[21–26] These numbers were obtained by assuming that phenolic resin behaves like a compact sphere in dilute acetone solution elucidated by previous studies using the Mark–Houwink–Sakurada equation with exponent values of 0.2–0.5.[21–26] This disagreement is probably due to the large molecular-weight distribution of the polymers investigated in this work, which complicates DLS data interpretation.[34–38] In this study of unfractionated phenolic resins with original molecular weight distribution, R_h was chosen as the value calculated from Γ at the point of the maximum $G(\Gamma)$ and M_w was chosen as the weight averaged value. If we consider the broad molecular-weight distribution of phenolic resins with M_w/M_n ranging from 2 to 36, as listed in Table 3.1, scattering from the higher molecular weight polymers should be dominant in the DLS measurements,[35] and M_z would be appropriate in this case for evaluating the relationship between R_h and the averaged molecular weight. Thus, we obtained the power-law behavior with a slope of 0.57 in the relation of R_h and M_z as seen in Figure 3.4b. At this point of discussion, however, the value of the exponent itself is not sufficient to determine the polymer conformation, and the important aspect here is that the polycondensation of the phenolic resins proceeds under the power-law relation of R_h and M_w or M_z irrespective of polymerization conditions.

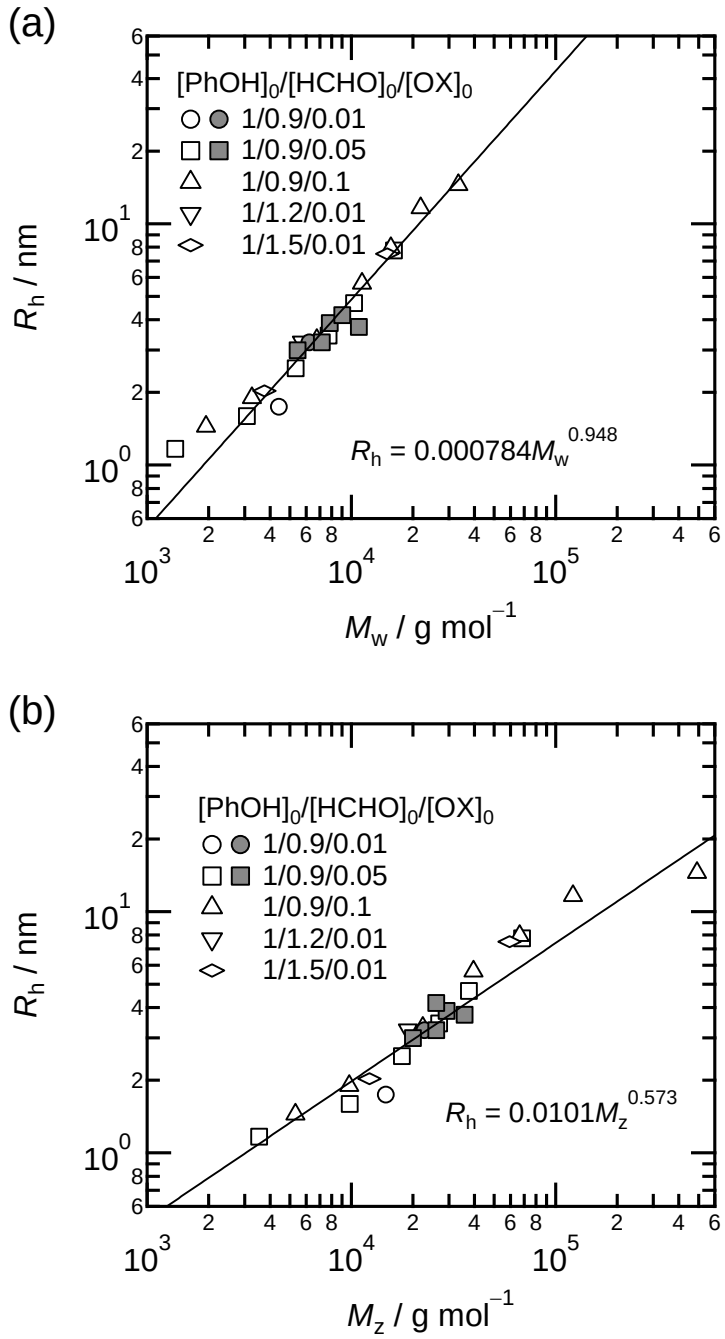

Figure 3.4 The hydrodynamic radius as functions of (a) the weight-average molecular weight and (b) the hydrodynamic radius as a function of the z-average molecular weight estimated by GPC. Open and filled symbols represent HCHO concentrations of 22 and 37 wt% in HCHO aq., respectively. The solid lines are the fitting results by the power-law function.

Figure 3.5a shows the change in observed SANS curves of NV0910a during polymerization. Polymer concentration in THF-d_8 was 10 vol%. The higher the molecular weight, the more intense the scattering intensity. Note that, as seen in this figure, the absolute intensity does not exceed 10^0 cm^{-1} even for the polymer with M_w of 33400 g mol^{-1}, which is the second-highest molecular weight in this experiment. This is due to the existence of a large portion of oligomers with small molecular weight, even in the high-molecular weight phenolic resins with M_w of > 10^4 g mol^{-1}, as seen in Figure 3.2. In this SANS study on unfractionated phenolic resins, a semidilute concentration of 10 vol% is required to obtain a reasonable SANS intensity. It is known that the scattering intensity from semidilute polymer solutions is described by the Ornstein–Zernike (OZ) equation[39] given by

$$I(q) = \frac{I(0)}{1+\xi^2 q^2}, \tag{3.6}$$

where ξ denotes the correlation length (i.e., a characteristic size of concentration fluctuations). By curve fitting observed scattering intensity functions ($I_{obs}(q)$) with

$$I_{obs}(q) = \frac{I(0)}{1+\xi^2 q^2} + I_{incoh}, \tag{3.7}$$

where I_{incoh} denotes an incoherent scattering intensity, the correlation lengths of the polymers in THF-d_8 were evaluated. The incoherent background was estimated to be 0.12–0.14 cm^{-1}. As shown in Figure 3.5b, the coherent scattering intensity functions are successfully described by the OZ equation (solid lines).

It is noted that the SANS curves fall into a single master curve by scaling $\xi^{-2}I(q)$ and ξq as shown in Figure 3.6a. This was the case for the polymers prepared using $[PhOH]_0/[HCHO]_0/[OX]_0$ = 1/0.9/0.1. More interestingly, as shown in Figure 3.6b, SANS curves for polymers prepared with different monomer molar ratios and catalyst amounts can be sufficiently superimposed to a single curve with these reduced variables within experimental error. These results indicate that the values of ξ have a self-similar structure with respect to the molecular weight, irrespective of the investigated polymerization conditions.

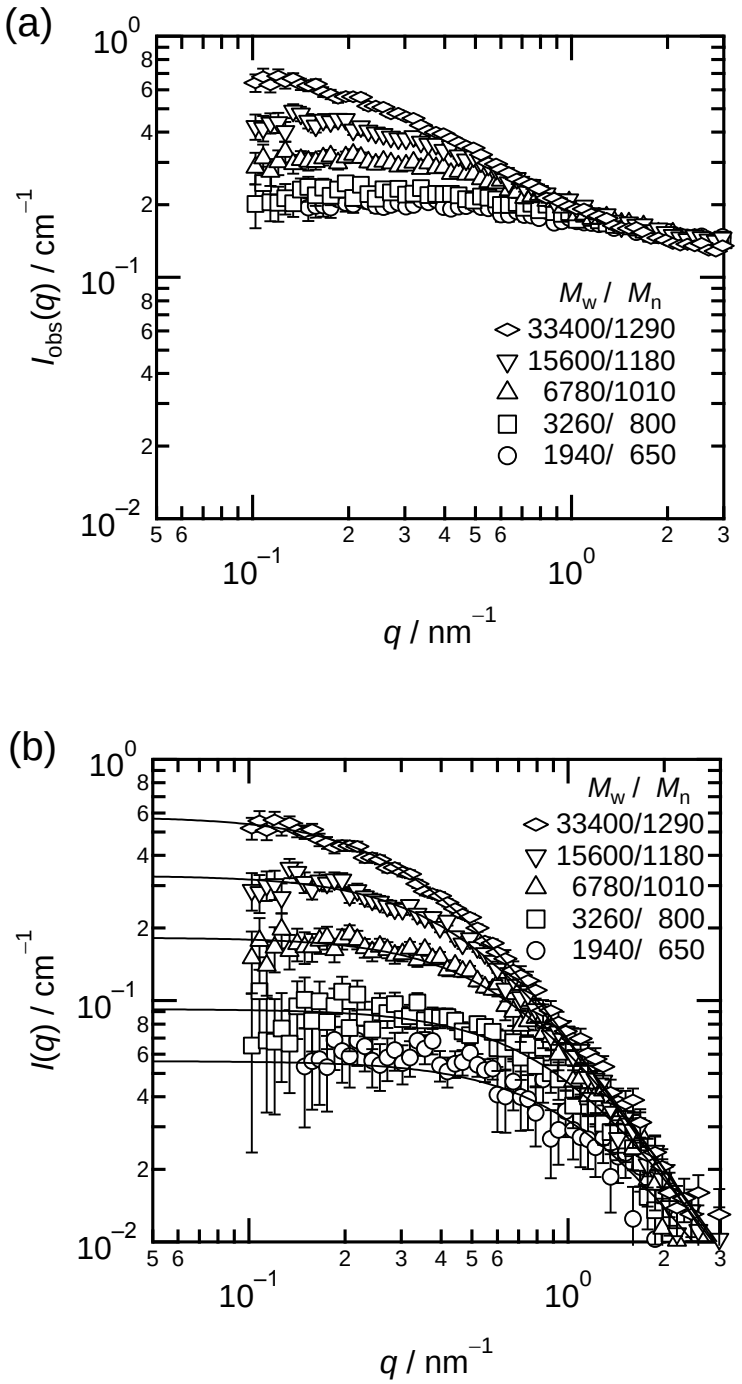

Figure 3.5 SANS curves of 10 vol% NV0910a in THF-d_8: (a) Observed and (b) coherent scattering intensity functions. Solid lines are the fitting results by the Ornstein–Zernike equation.

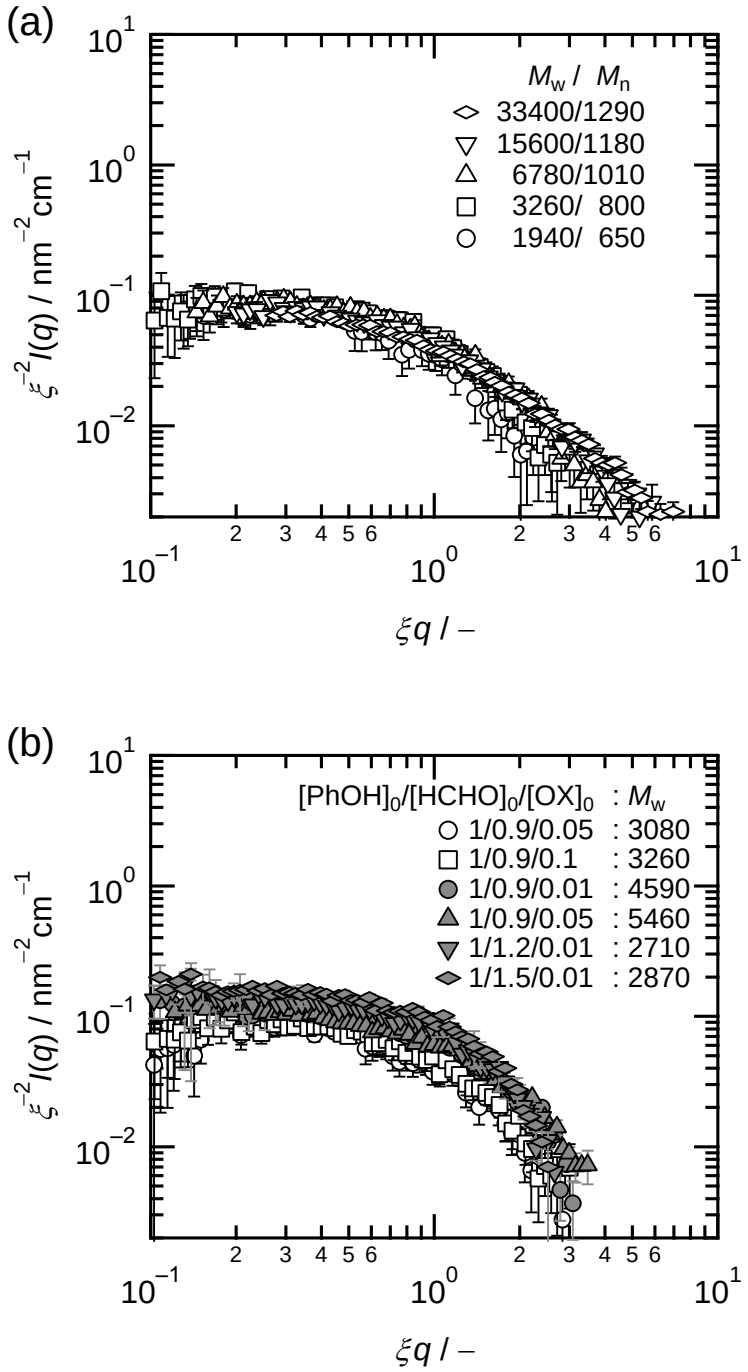

Figure 3.6 Scaled plots of SANS curves, $\xi^{-2}I(q)$ and ξq, for (a) 10 vol% NV0910a, and (b) 10 vol% phenolic resin solutions. Open and filled symbols represent HCHO concentrations of 22 and 37 wt% in HCHO aq., respectively.

The calculated values of ξ are plotted against M_w and M_z in Figures 3.7a and 3.7b, respectively. The power-law behaviors are obtained for both plots and their exponents are 0.44 and 0.27, respectively. This suggests that ξ and M_w and M_z of phenolic resins prepared from PhOH, HCHO, and OX obey a power-law relation, and this behavior is also irrespective of polymerization conditions. As mentioned above, polymers with high-molecular weight polymers still contain a large portion of oligomers, which do not give sufficiently intense SANS signals. Hence, M_z would be a more appropriate measure of the molecular weight for this evaluation of the scaling exponent than M_w.

In the above discussions, we have elucidated that there exists a clear relationship between the characteristic properties, R_h and ξ, and the molecular weight for phenolic resins. However, there is a large difference in the scaling exponents. One of the major reasons is the difference in polymer concentration in solution. With increasing polymer concentration, the segment–segment spatial correlation is screened by the surrounding segments and the long-range intrachain excluded-volume interactions decrease, and as a result, the scaling exponents are lowered.[40–42] Thus, the exponent of 0.27 obtained by SANS experiments in 10 vol% solution becomes smaller than the value obtained by DLS experiments in 1 vol% solution (0.57). Figure 3.8 schematically illustrates the time-evolution of (a) R_h (diluted) and (b) and ξ (semidiluted). In the diluted region (a), clusters of phenolic resin oligomers grow with polymerization, and $G(\Gamma)$ shifts to larger R_h. In the semidilute regime (b), the scattering intensity increases accompanying an increase in ξ. Furthermore, a self-similarity in the concentration fluctuations is maintained, as revealed by SANS ($\xi^{-2}I(q)$ vs ξq plot). These seem to be a characteristic feature of the polymerization of phenolic resins.

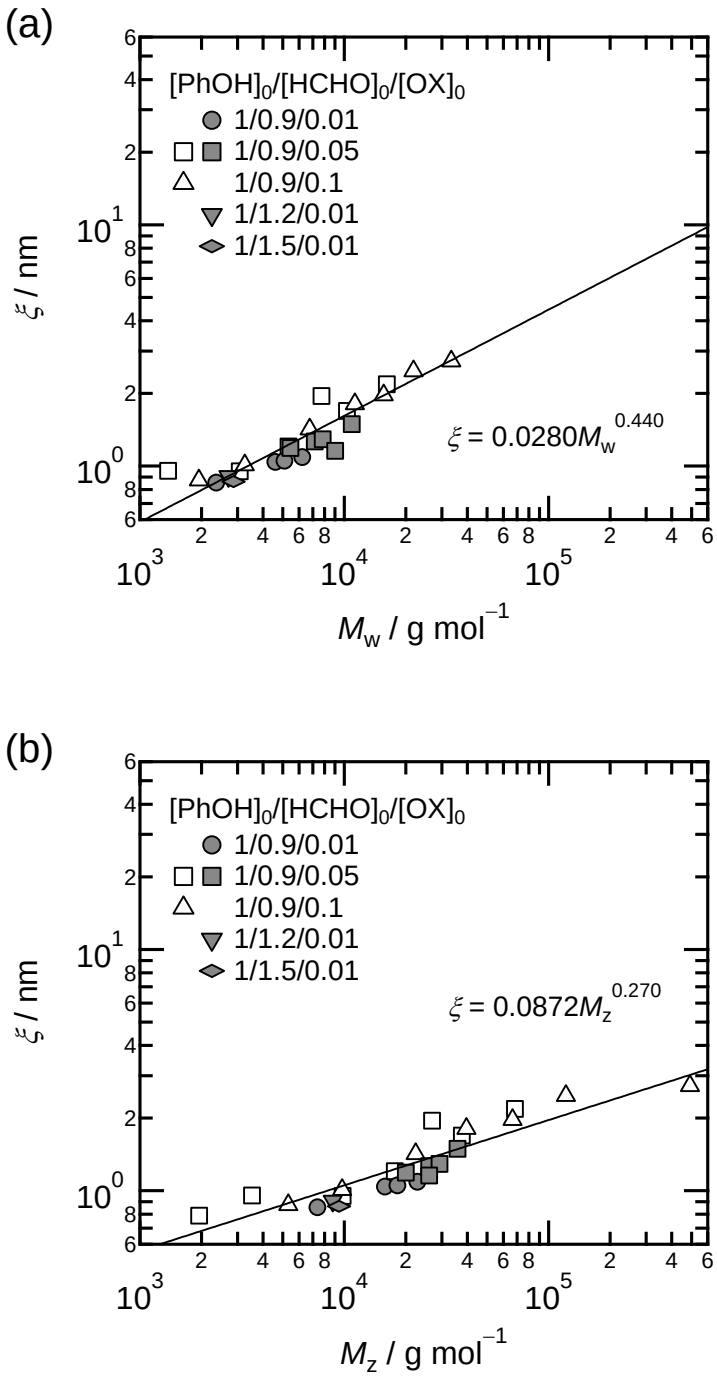

Figure 3.7 The correlation length as a function of (a) the weight-average molecular weight, and (b) the *z*-average molecular weight estimated by GPC. Open and filled symbols represent HCHO concentrations of 22 and 37 wt% in HCHO aq. respectively. The solid line is the fitting result by the power-law function.

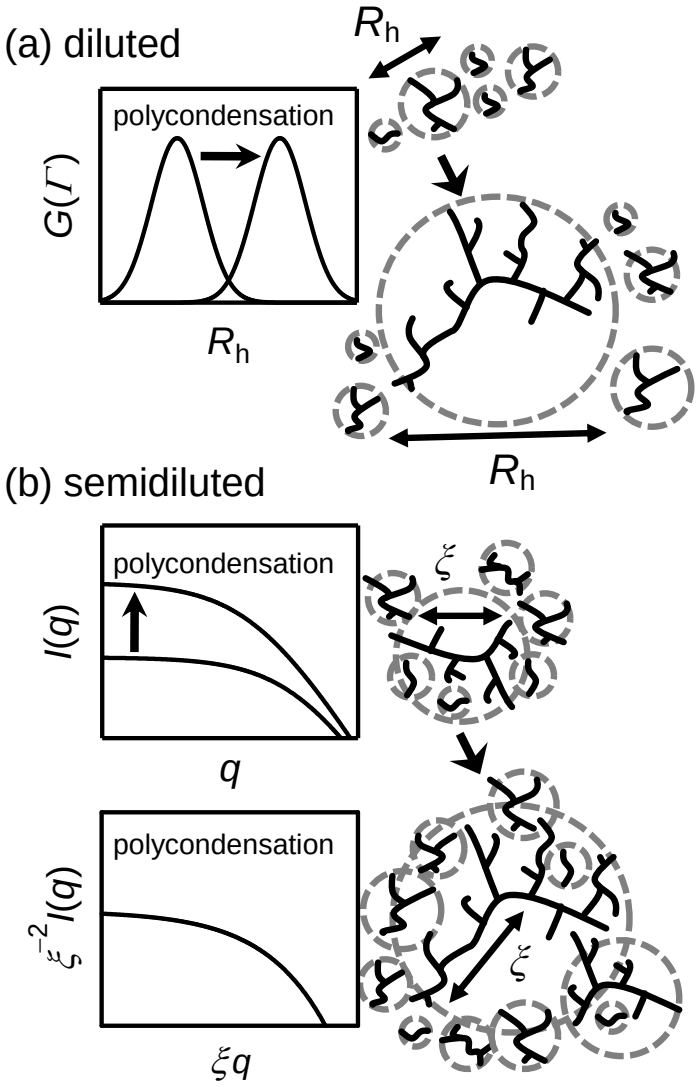

Figure 3.8 Schematic illustration showing time-evolution of (a) the hydrodynamic radius at diluted, and (b) the correlation length at semidiluted.

3.4 Conclusions

Solution properties of unfractionated phenolic resins prepared by the polycondensation of PhOH and HCHO using OX as a catalyst were investigated by GPC, DLS, and SANS experiments. R_h in 1 vol% acetone solution obtained by DLS obeys the power-law relation with M_z (estimated by GPC) and the scaling exponent of 0.57 was obtained. SANS curves of 10 vol% solution in THF-d_8 were fitted using the OZ equation and could be superimposed to a single curve with the reduced variables, $\xi^{-2}I(q)$ and ξq. These results indicate that ξ is determined by the polymer size or molecular weight and the polymers have a self-similar structure with respect to the molecular-weight distribution. In addition, ξ obeys the power-law relation with M_z (estimated by GPC) with the scaling exponent of 0.27. The deviation in scaling exponents of M_z is due to the difference in polymer concentration in solution, because higher concentration lowers the exponent owing to the screening effect. In this study, we explored a new approach for evaluating the solution properties of unfractionated phenolic resins, with original molecular-weight distribution, using GPC, DLS, and SANS. When the monomer concentration is sufficiently low, clusters of phenolic resin oligomers grow as polymerization proceeds with a power-law of $R_h \sim M_z^{0.57}$. On the other hand, in the semidilute regime, ξ evolves with $\xi \sim M_z^{0.57}$, while maintaining the self-similarity between $\xi^{-2}I(q)$ and ξq. This is, to our knowledge, the first observation of the structural evolution of phenolic resins during polymerization.

3.5 References

1 M. Shibayama, *Macromol. Chem. Phys.*, 1998, **199**, 1–30.

2 M. Shibayama and T. Norisuye, *Bull. Chem. Soc. Jpn.*, 2002, **75**, 641–659.

3 M. Shibayama, T. Karino, Y. Domon and K. Ito, *J. Appl. Cryst.*, 2007, **40**, s43–s47.

4 E. Girard-Reydet, H. Sautereau, J. P. Pascault, P. Keates, P. Navard, G.

Thollet and G. Vigier, *Polymer*, 1998, **39**, 2269–2279.

5 F. L. Meng, S. X. Zheng, H. Q. Li, Q. Liang and T. X. Liu, *Macromolecules*, 2006, **39**, 5072–5080.

6 D. Hu, Z. G. Xu, K. Zeng and S. X. Zheng, *Macromolecules*, 2010, **43**, 2960–2969.

7 J. Brus, M. Špírková, D. Hlavatá and A. Strachota, *Macromolecules*, 2004, **37**, 1346–1357.

8 D. W. Schaefer and R. S. Justice, *Macromolecules*, 2007, **40**, 8501–8517.

9 H. Zou, S. S. Wu and J. Shen, *Chem. Rev.*, 2008, **108**, 3893–3957.

10 E. Hoinkis and A. J. Allen, *Carbon*, 1991, **29**, 81–91.

11 A. Gupta and I. R. Harrison, *Carbon*, 1994, **32**, 953–960.

12 J. M. Calo, P. J. Hall and M. Antxustegi, *Colloids Surf., A*, 2001, **187–188**, 219–232.

13 J. M. Calo and P. J. Hall, *Carbon*, 2004, **42**, 1299–1304.

14 K. Dušek, *Angew. Makromol. Chem.*, 1996, **240**, 1–15.

15 K. Dušek, J. Pleštil, F. Lednický and S. Luňák, *Polymer*, 1978, **19**, 393–397.

16 R. J. Matyi, D. R. Uhlmann and J. A. Koutsky, *J. Polym. Sci., Part B: Polym. Phys.*, 1980, **18**, 1053–1063.

17 N. C. Beck Tan, B. J. Bauer, J. Plestil, J. D. Barnes, D. Liu, L. Matêjka, K. Dušek and W. L. Wu, *Polymer*, 1999, **40**, 4603–4614.

18 S. J. Bai, *Polymer*, 1985, **26**, 1053–1057.

19 A. Gardziella, L. A. Pilato and A. Knop, *Phenolic Resins: Chemistry, Applications, Standardization, Safety and Ecology*, 2nd completely rev. edn., Springer, Berlin, 1999.

20 Y. Zhang, Y. J. Liu, Q. He and Z. W. Han, *J. Appl. Polym. Sci.*, 2008, **108**, 3009–3015.

21 S. Ishida, M. Nakagawa, H. Suda and K. Kaneko, *Koubunshi Kagaku*, 1971, **28**, 250–253.

22 F. L. Tobiason, C. Chandler and F. E. Schwarz, *Macromolecules*, 1972, **5**, 321–325.

23 K. Kamide and Y. Miyakawa, *Makromol. Chem.*, 1978, **179**, 359–372.

24 T. Yamagishi, M. Nomoto, S. Ito, S. Ishida and Y. Nakamoto, *Polym. Bull.*, 1994, **32**, 501–507.

25 T. Yamagishi, H. Kumagai, T. Hasegawa, Y. Nakamoto and S. Ishida, *Polym. Int.*, 1995, **36**, 333–338.

26 T. Yamagishi, M. Nomoto, S. Yamashita, T. Yamazaki, Y. Nakamoto and S. Ishida, *Macromol. Chem. Phys.*, 1998, **199**, 423–428.

27 E. Geissler, Dynamic Light Scattering from Polymer Gels. in *Dynamic Light Scattering: the Methods and Applications*, ed. W. Brown, Oxford University, Oxford, England, 1993.

28 S. W. Provencher, *Comput. Phys. Commun.*, 1982, **27**, 213–227.

29 C. L. Yaws, *Handbook of Viscosity*, Gulf Professional Publishing, Houston, TX, 1995.

30 C. Wohlfarth and B. Wohlfarth, Optical Constants, Subvolume B: Refractive Indices of Organic Liquids. in *Landolt–Börnstein: Group III - Condensed Matter*, ed. M. D. Lechner, Springer, Berlin, 1996, vol. 38.

31 S. Okabe, M. Nagao, T. Karino, S. Watanabe, T. Adachi, H. Shimizu and M. Shibayama, *J. Appl. Cryst.*, 2005, **38**, 1035–1037.

32 S. Okabe, T. Karino, M. Nagao, S. Watanabe and M. Shibayama, *Nucl. Instrum. Methods Phys. Res., Sect. A*, 2007, **572**, 853–858.

33 H. Iwase, H. Endo, M. Katagiri and M. Shibayama, *J. Appl. Cryst.*, 2011, **44**, 558–568.

34 L. Mrkvičková, B. Porsch and L. O. Sundelöf, *J. Appl. Polym. Sci.*, 1995, **58**, 2033–2038.

35 M. Shibayama, T. Karino and S. Okabe, *Polymer*, 2006, **47**, 6446–6456.

36 W. H. Stockmayer and M. Schmidt, *Pure Appl. Chem.*, 1982, **54**, 407–414.

37 G. Vancso, I. Tomka and K. Vancso-Polacsek, *Macromolecules*, 1988, **21**, 415–420.

38 C. Wu and D. Lilge, *J. Appl. Polym. Sci.*, 1993, **50**, 1753–1759.

39 H. E. Stanley, *Introduction to Phase Transitions and Critical Phenomena*, Oxford University Press, New York, 1971.

40 P. G. de Gennes, *Scaling Concepts in Polymer Physics*, Cornell University, Ithaca, New York, 1979.

41 M. Oostwal and T. Odijk, *Macromolecules*, 1993, **26**, 6489–6497.

42 E. Geissler, S. Mallam, A. M. Hecht, A. R. Rennie and F. Horkay, *Macromolecules*, 1990, **23**, 5270–5273.

Chapter 4

Gelation and Cross-link Inhomogeneity of Phenolic Resins Studied by ^{13}C-NMR Spectroscopy and Small-Angle X-ray Scattering

4.1 Introduction

For elucidating the inhomogeneity of gel networks, characterization of the formation and growth mechanisms of gel networks could be an important key to elucidate the inhomogeneity of phenolic and other thermosetting resins. However, the precise structural analysis of the gelation process is difficult to perform because of insolubility issues, and there have only been a few computer simulation studies investigating the network structure of phenolic resins after gelation. Yamagishi et al. investigated the gelation mechanism of phenolic resins using the Monte Carlo simulations with the cubic percolation theory.[1] According to the simulation results for a polycondensation system with an initial formaldehyde-to-phenol molar ratio of 1.2, the intramolecular reaction occurred more frequently with increasing gel fraction beyond the gelation point and resulted in network formation inside the gel. Unfortunately, this significant result for the gelation mechanism of phenolic resins has not yet been evaluated experimentally.

As mentioned in the previous chapters, dynamic light scattering (DLS), small-angle neutron and X-ray scattering (SANS and SAXS, respectively) are

powerful techniques for elucidating the inhomogeneity of gel networks. In most cases, these techniques utilize the swelling feature of the gel; swelling enhances the local fluctuations of the crosslink density because the degree of swelling depends on the degree of cross-linking. The enhancement of the spatial inhomogeneity of the gel network results in a large scattering contrast. Herein, we discuss the results of the application of this solvent-swelling technique to phenolic resins for the elucidation of their gelation mechanism and cross-link inhomogeneity, and report our observations based on the ^{13}C-NMR and SAXS analysis of phenolic resins during the gelation process.

We believe that this study is the first report of experimentally elucidated mechanisms for the formation and growth of the cross-link inhomogeneity in phenolic resins. In addition, we want to emphasize that the topic of this study addresses general issues of thermosetting resins and is not limited specially to phenolic resins, which is important because elucidating their cross-link inhomogeneity remains one of the major objectives of studies on thermosetting resins, as mentioned above. The successful application of the well-established solvent-swelling technique for structural analysis of the gel networks to phenolic resins during their gelation process offers a new technique for elucidating the inhomogeneity of thermosetting resins.

4.2 Experimental

4.2.1 Materials

Phenol (PhOH), formaldehyde (HCHO, 37 wt% solution in water), oxalic acid (anhydrous), and tetrahydrofuran (THF) were purchased from Wako Pure Chemical Industries, Ltd., Japan. Methanol-d_4 was purchased from Merck KGaA, Germany. All materials were used without further purification.

4.2.2 Sample Preparation

Phenolic resins NV10, NV12, and NV15 were prepared via the polycondensation of PhOH and HCHO using oxalic acid as a catalyst, as shown in Figure 4.1. A solution containing phenol (110 g, 1.17 mol), 37 wt% formaldehyde (94.9 g, 1.17 mol for NV10; 113.9g, 1.40 mol for NV12; 142.3 g, 1.75 mol for NV15), and oxalic acid (1.05 g, 0.0117 mol) was divided into six portions; each portion was transferred to a 50-mL-sealable vial, and then the vials were tightly sealed. The six vials were heated at 100 °C for 50, 100, 150, 200, 300, and 450 min. Each reaction mixture was first cooled in a water bath, and then milled and washed three times with water (200 mL) using a mixer mill (Labo Millser LM-2, Iwatani Corporation, Japan). The obtained solids were frozen in liquid nitrogen, and then dried in a vacuum at 30 °C for 3 h, at 60 °C for 2 h, and at 70 °C for 1 day. It should be noted that the reaction was performed without stirring the mixture to avoid affecting the results with any slight differences in the stirring efficiencies of each reaction mixture because NV12 and NV15 became highly viscous and finally lost fluidity with reaction time.

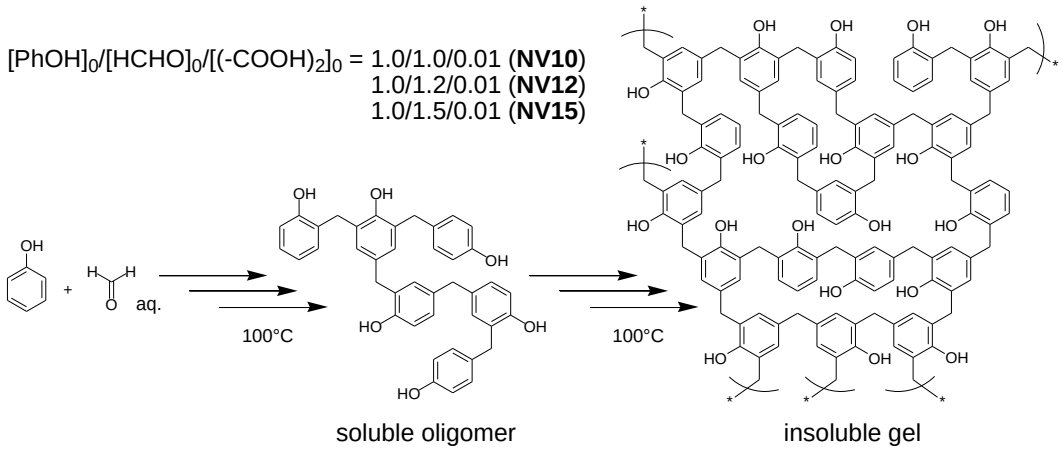

Figure 4.1 Polycondensation of phenol and formaldehyde.

4.2.3 GPC

For the THF-soluble polymers, gel permeation chromatography (GPC) experiments were performed using a Tosoh HLC-8320 system equipped with four poly(styrene-co-divinylbenzene) gel columns (TSKgel GMH_{XL}, GMH_{XL}, $G2000H_{XL}$, and $G2000H_{XL}$) and a refractive index detector. THF at 40 °C was used as the eluent. The weight-average molecular weight (M_w) and the number-average molecular weight (M_n) were calculated with a calibration line that was obtained by fitting the peak molecular weights of 13 polystyrene (PSt) standards using a cubic function. The peak molecular weights of the PSt standards were 1.09×10^6, 7.06×10^5, 3.55×10^5, 1.90×10^5, 9.64×10^4, 3.79×10^4, 1.81×10^4, 1.02×10^4, 5970, 2630, 994, 152, and 124 g mol^{-1}. The polymer concentration of the injection solution was 0.20 mg mL^{-1}. The polymer solution was filtered through a 0.45-μm filter (Tosoh H-13-5) before injection into the chromatograph. The GPC results for the THF-soluble polymers are listed in Table 4.1.

4.2.4 Determination of the Degree of Swelling

For the THF-insoluble polymers, the degree of swelling (VV_0^{-1}) in the fully THF-swollen state was estimated from the change in the volume before and after drying the fully THF-swollen gel (1–2 g) at 60 °C for 24 h in a vacuum (V and V_0, respectively). Here, the volume was estimated from the weight of sample and densities of polymers and THF, which were assumed to be 1.2 and 0.89 g cm^{-3}, respectively. The value VV_0^{-1} was obtained as the average of three measurements, and the results are listed in Table 4.2.

4.2.5 ^{13}C-NMR Spectroscopy

^{13}C-NMR experiments were performed using a JEOL JNM-ECA400 NMR spectrometer operated at 100 MHz using a 45° pulse at room temperature. Solution ^{13}C-NMR spectra were recorded using the nuclear Overhauser effect-eliminated proton complete decoupling method with 1024 scans and a

Table 4.1 Molecular weight of the soluble polymers.

time / min	NV10		NV12		NV15	
	M_w / g mol^{-1}	M_n / g mol^{-1}	M_w / g mol^{-1}	M_n / g mol^{-1}	M_w / g mol^{-1}	M_n / g mol^{-1}
50	390	810	5930	990	4770	910
100	790	1010	23700	1260	–[a]	
150	680	1070	–[a]		–[a]	
200	590	1130	–[a]		–[a]	
300	1600	1180	–[a]		–[a]	
450	3600	1200	–[a]		–[a]	

[a] Polymers are insoluble in THF because of gelation.

Table 4.2 Degree of swelling in the fully THF-swollen state for the insoluble polymers.

time/min	NV10	NV12	NV15
50	–[a]	–[a]	–[a]
100	–[a]	–[a]	12
150	–[a]	15	11
200	–[a]	12	7.6
300	–[a]	8.4	6.2
450	–[a]	8.3	5.4

[a] Polymers are soluble in THF.

relaxation delay of 105 s between subsequent scans to obtain quantitative data, where the total acquisition time for a single measurement was 30 h. A 25 wt% solution in methanol-d_4 that was filtered through a 0.45-μm filter (Tosoh H-13-5), as in the GPC experiments, was used for the measurements. Solid-state ^{13}C-NMR spectra were recorded with 1024 scans and a relaxation delay of 330 s between subsequent scans under a magic-angle spinning (MAS) frequency of 20 kHz to obtain quantitative data, where the total acquisition time for a single measurement was 4 days. A two-pulse, phase-modulated proton decoupling pulse sequence was applied during the acquisition time. A JEOL 3.2 mm cross-polarization MAS probe was used.

4.2.6 SAXS

SAXS experiments were performed on the BL03XU beamline (Frontier Softmaterial Beamline (FSBL)) at SPring-8 that is located in Sayo, Hyogo, Japan.[2] A monochromated X-ray beam with a wavelength (λ) of 1.0 Å was used to irradiate the samples at room temperature, and the scattered X-rays were counted at the sample-to-detector distance of 1.1 m. Quartz glass capillaries (Mark-Tube, Hilgenburg GmbH, Germany) with a diameter of 2 mm and a wall thickness of 0.01 mm were used for the sample cells. The height and width of the X-ray beam at the sample position were set to 0.04 and 0.1 mm, respectively, and the scattered X-rays were counted by an imaging plate detector (R-AXIS VII++, Rigaku Corporation, Japan) with 3000 × 3000 pixel arrays and a pixel size of 0.1 mm pixel^{-1}. After necessary correction for the dark current, background scattering, and transmittance, the corrected scattering intensity functions were normalized to the absolute intensity scale using a 1-mm-thick glassy carbon plate (glassy carbon Type 2, Alfa Aesar, USA) as a secondary standard, in which the absolute intensity of the glassy carbon plate was previously determined using a glassy carbon that was provided by Jan Ilavsky of the Advanced Photon Source at Argonne National Laboratory in Illinois, USA.[3] Errors were calculated with standard deviations.

4.3 Results and Discussion

The solubility of the polymers (i.e., soluble or insoluble in THF) is indicated in Table 4.1; NV10 remained soluble in THF at 450 min, while NV12 and NV15 became insoluble in THF at 150 and 100 min, respectively, because of gelation. It should be noted that polycondensation with an initial molar ratio of formaldehyde-to-phenol ($[HCHO]_0/[PhOH]_0$) of 1.0 typically results in gelation.[1,4] However, gelation of NV10 did not occur in this study. The absence of gelation for NV10 was because of the reduced reaction rate as described in Section 4.2.2.

Figure 4.2 shows the change in the molar ratio of methylene-to-phenolic units in the phenolic resins ($R_{CH2/PhOH}$), where the value $R_{CH2/PhOH}$ was estimated

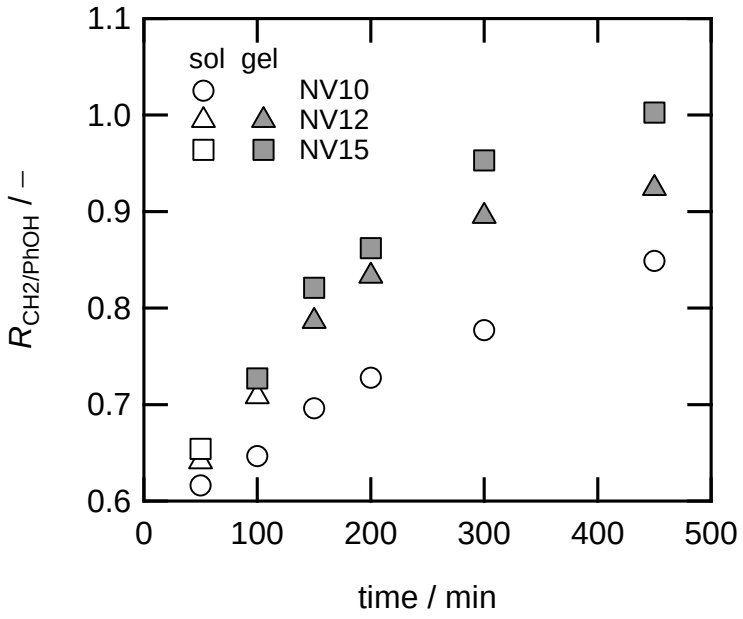

Figure 4.2 Change in the molar ratio of methylene-to-phenolic units in the phenolic resins estimated using ^{13}C-NMR: Open symbols, THF-soluble polymers; Filled symbols, THF-insoluble polymers.

from the integral ratio of the aromatic-to-aliphatic carbons in the solution ^{13}C-NMR spectra of NV10 and the solid-state ^{13}C-NMR spectra of NV12 and NV15 that were recorded under quantitative acquisition conditions. Note that the $R_{CH2/PhOH}$ values of NV10, NV12, and NV15 at a full-formaldehyde conversion are 1.0, 1.2, and 1.5, respectively, because the initial molar ratios $[HCHO]_0/[PhOH]_0$ were 1.0, 1.2, and 1.5, respectively. The $R_{CH2/PhOH}$ values of NV10, NV12, and NV15 increased with reaction time up to the investigated 450 min without any sign of gelation. This result indicates that the polycondensation proceeds irrespective of gelation, which can be observed as the change in the degree of swelling in the fully THF-swollen state for the insoluble polymers as shown in Table 4.2. Here, the degree of swelling is defined as the volume change ratio. Both of the VV_0^{-1} values of NV12 and NV15 decreased with reaction time, which could result from a decrease in the average mesh size of the gel network.[5] Therefore, the polycondensation reaction that occurs after gelation could shorten

the average mesh size of the gel network. The $R_{CH2/PhOH}$ value of NV10 reached 0.85 without gelation, whereas those for NV12 and NV15 were well below 0.85 when they became insoluble (i.e., 0.78 at 150 min and 0.73 at 100 min, respectively). These results can be explained by the difference in the rate of formation of branched structures; that is, an increase in the initial molar ratio $[HCHO]_0/[PhOH]_0$ would result in an increase in the rate, which implies the presence of different gelation mechanisms that depend on the initial molar ratio. Note that, a previous study of the phenol–formaldehyde polycondensation kinetics using a statistical recursive method reported by Aranguren et al. has demonstrated that the $[HCHO]_0/[PhOH]_0$ value strongly affects the molar fractions of branched phenolic units in the resulting structure.[4]

To elucidate the cross-link inhomogeneity by characterizing this ensemble-averaged structural information in more detail, SAXS experiments were performed with 7 wt% THF solutions of the soluble polymers and the fully THF-swollen gels (i.e., semidilute state) for the insoluble polymers. The semidilute concentration of 7 wt% was chosen such that the value would be the same as the weight fraction of NV12 in the fully THF-swollen state when the polymer became insoluble.

In our previous studies involving SANS analysis of THF-soluble phenolic resin oligomers prepared via the polycondensation of phenol and formaldehyde with oxalic acid (see Chapter 3), the coherent neutron scattering curves from semidilute phenolic resin solutions in THF-d_8 were well described by the Ornstein–Zernike (OZ) equation[6] that is given by

$$I(q) = \frac{I(0)}{1+\xi^2 q^2}, \tag{4.1}$$

where q and ξ denote the magnitude of the scattering vector and the correlation length (i.e., the characteristic size of the concentration fluctuations), respectively. Here q is given by $q = (4\pi/\lambda)\sin(2\theta/2)$, where 2θ denotes the scattering angle. The SAXS curve from a phenolic resin solution in THF can give essentially the same information as the SANS profile in THF-d_8 because the SANS and SAXS

profiles of the phenolic resin solutions result from fluctuations of the neutron and X-ray scattering length densities (ρ) in the solution, and the difference in ρ (i.e., the scattering contrast) between the phenolic resins and the solvent (THF or THF-d_8) exists for both methods.

The SAXS curves are shown in Figure 4.3, in which the statistical error bars are small enough to be hidden by the graph markers. The SAXS curves of the soluble phenolic resins NV10 and NV12 at 50–100 min, and NV15 at 50 min are well fitted by the OZ equation, as shown by the solid lines in Figures 4.3a–c. Our previous SANS experiments with THF-d_8 solutions of soluble polymers demonstrated that polycondensation proceeds under the power-law relation of ξ and M_w irrespective of the polycondensation conditions (i.e., formation a self-similar structure with respect to the molecular weight) (see Chapter 3).[7] To clarify the characteristic features of the structural evolution of phenolic resins during polycondensation, the fitting parameter ξ is plotted as a function of M_w, in Figure 4.4, and such structural evolution of soluble polymers is confirmed by the

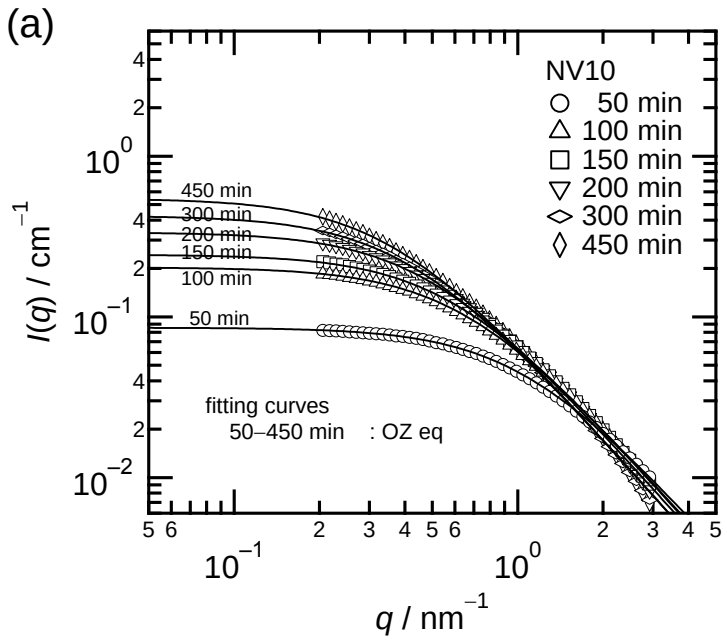

Figure 4.3 Change in the SAXS curves and curve fitting results as a function of reaction time: (a) NV10, (b) NV12, and (c) NV15; Open and filled symbols represent THF-soluble and insoluble polymers, respectively.

power-law relationship between them. Note that the difference in the exponent between this study (0.62) and our previous results (0.44) could be attributed to different measurement conditions such as solvent, concentration, and scattering method.

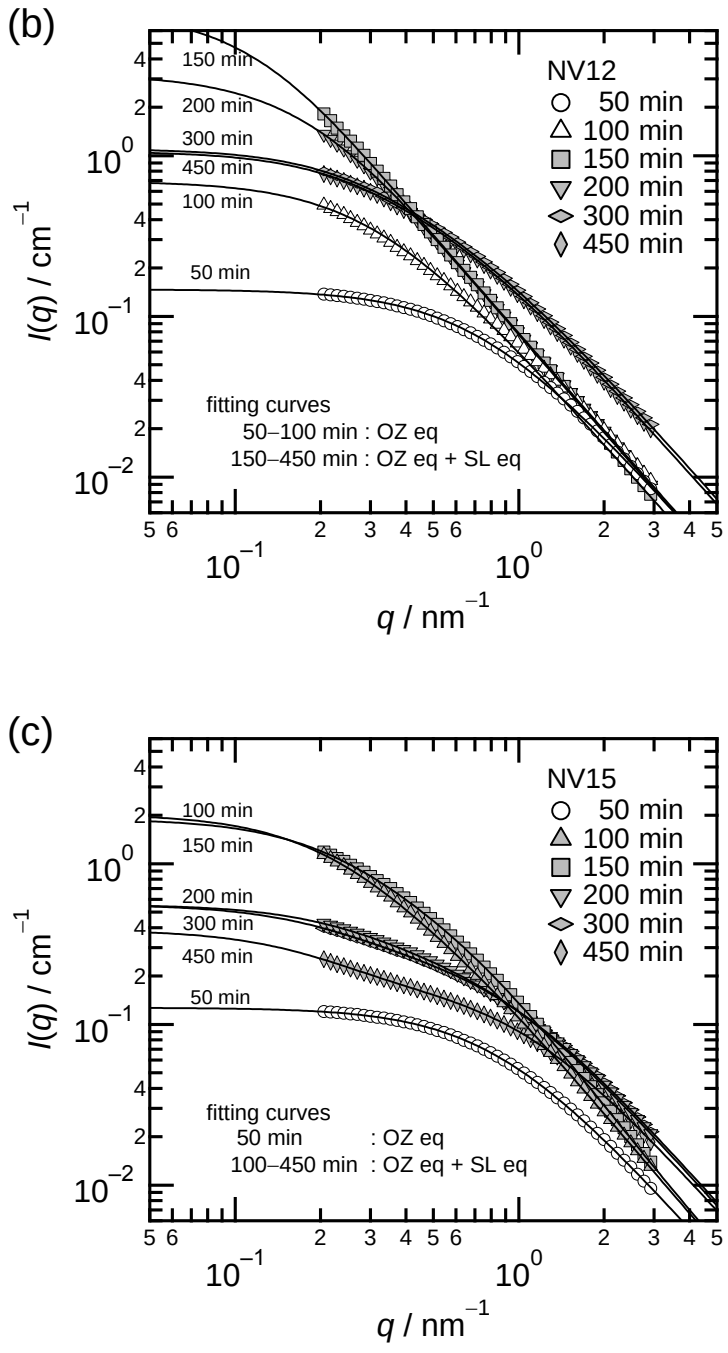

Figure 4.3 Continued.

On the other hand, as seen in Figures 4.3b and 4.3c, there is a clear change in the shape of the scattering curves after gelation, both for NV12 and NV15, which cannot be explained solely by the OZ equation. In particular, when the scattering curve can be explained by the OZ equation, the slope (m) of the double logarithmic plot of eq 4.1 should remain larger than or equal to −2; however, the value of m of NV12 at 150 min falls below −2 in the q range near 0.3 nm^{-1}, which was confirmed by the presence of a negative slope in the function $q^2I(q)$ vs q. This result suggests the presence of another structure related to the spatial inhomogeneity; therefore, another theoretical function should be considered to explain the scattering curves after gelation.

It is well known that chemically cross-linked polymer gels typically have topological defects and spatial inhomogeneities in their network structure with a scattering function are well-described as a combination of two scattering functions

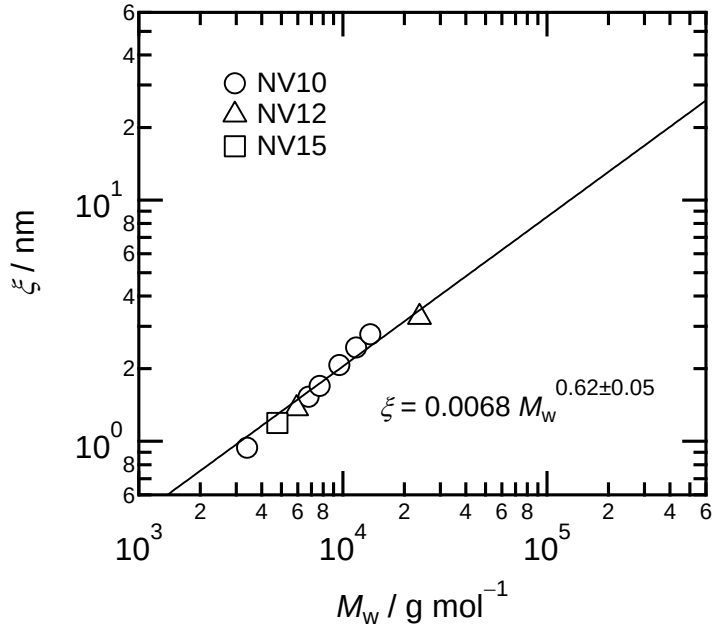

Figure 4.4 Correlation length as a function of the weight-average molecular weight. The solid line is the fitting result by the power-law function.

of a liquid-like fluctuation and a solid-like frozen inhomogeneity.[8,9] When the second term is described with the Squared–Lorentz (SL) equation given by

$$I_{ex}(q) = \frac{I_{ex}(0)}{\left(1+\Xi^2 q^2\right)^2}, \tag{4.2}$$

where Ξ denotes the characteristic length of the inhomogeneity, the scattering function of polymer gels is given by the combination of the OZ and SL equations by

$$I(q) = \frac{I(0)}{1+\xi^2 q^2} + \frac{I_{ex}(0)}{\left(1+\Xi^2 q^2\right)^2}. \tag{4.3}$$

Note that the SL equation is equal to the Debye–Bueche equation representing a two-phase structure with a sharp boundary, such that the SL equation here represents the presence of a sharp boundary between randomly and inhomogeneously cross-linked domains in the network structure. This empirical equation has long been used to represent the structure factor of gels in the swollen state.[8–14] However, there is no report on the application of this equation to the structural analysis of the inhomogeneity of insoluble and infusible phenolic and other thermosetting resins. As described so far, insoluble phenolic resins can swell in THF at the initial stage of their gelation, which suggests that the empirical equation is also applicable to the swollen phenolic resins. In fact, a curve fitting using eq 4.3 was successful for all of the NV12 and NV15 SAXS curves after gelation (filled symbols in Figures 4.3b and 4.3c, respectively). This result clearly indicates that, after gelation, both NV12 and NV15 have frozen cross-link inhomogeneity that can be explained by the SL equation. It should be mentioned that additional lower-q scattering data could serve to confirm the validity of the fitting scheme (i.e., in the q range of 0.05–0.2 nm^{-1} where flattening of the fitting curves appears, as seen in Figures 4.3a–c). To obtain a reasonable signal in that q range with these samples that exhibit low-absolute scattering intensities (i.e., $I(0) = 10^{-1}$–10^{0} cm^{-1}), experimental conditions with lower background scattering and lower radiation energy are preferred because they result in an increase in the signal-to-background ratio and a decrease in the radiation damage of the polymer

structure over longer irradiation times, respectively. Therefore, we are planning to perform SANS experiments for further investigations because of the lower parasitic scattering and beam energy of SANS compared to those of SAXS.

Figure 4.5 shows the fitting parameters ξ and Ξ as a function of reaction time. As discussed above, the value ξ is related to the average size of phenolic resins when they are soluble, which agrees with our previous SANS results (see Chapter 3).[7] On the other hand, the ξ values of NV12 and NV15 reach a maximum, and then decrease after gelation. This result indicates that the value ξ of a swollen gel is related to the mesh size of the gel network that behaves like a polymer chain in the semidilute regime.[9,12] Therefore, the decrease in ξ with reaction time is because of a decrease in the mesh size, which agrees with a decrease in VV_0^{-1} with reaction time. There is a distinct difference in the behavior of Ξ between NV12 and NV15 as shown in Figure 4.5. The value of NV12 decreased with reaction time, whereas that of NV15 increased. This result could provide very important tips for understanding the mechanism of the formation and growth of the

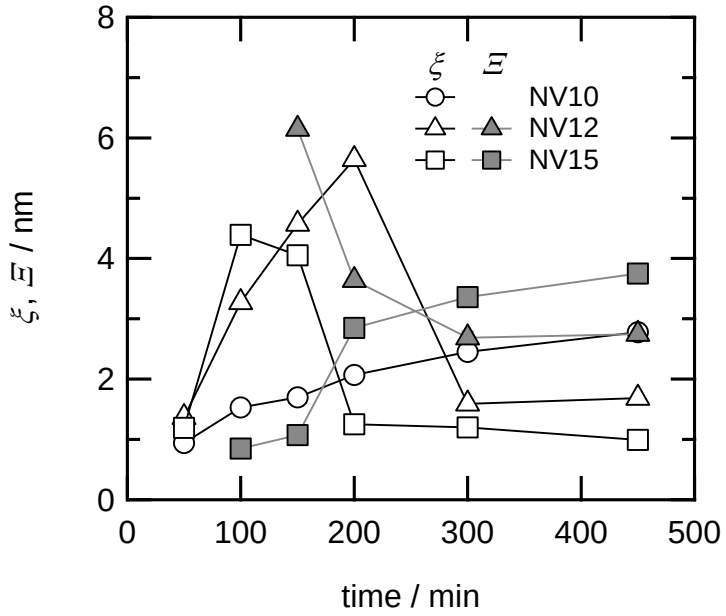

Figure 4.5 Change in the fitting parameters as a function of reaction time: Open symbols, correlation length; Filled symbols, correlation length of the inhomogeneity. Solid lines are guides for the eyes.

cross-link inhomogeneity. When the characteristic length of the inhomogeneity Ξ is defined by the correlation length of the inhomogeneity, the value Ξ is related to the size of a domain that has a higher crosslink density and a degree of swelling that is lower than the ensemble average. Therefore, the increase in the value Ξ of NV15 with reaction time could be ascribed to an increase in the size of the domain with a higher crosslink density. On the other hand, the decrease in the value Ξ of NV12 with reaction time cannot be explained by the size growth of the domain. To characterize the structural change that resulted in a decrease in Ξ, it is necessary to consider that the insoluble phenolic resins were prepared in the bulk state, whereas their SAXS curves were obtained in the THF-swollen state. An increase in the degree of cross-linking accompanies a decrease in the degree of swelling of the domain, which could be sufficient to account for the decrease in the value of Ξ of NV12 with reaction time. This conjecture for NV12 agrees with the previously proposed gelation mechanism of phenolic resins by Yamagishi et al. through the Monte Carlo simulations with the cubic percolation theory,[1] in which the simulation parameters were optimized for an experimental polycondensation result with a $[HCHO]_0/[PhOH]_0$ of 1.2 equal to that of NV12. The simulation indicated that the intramolecular reaction occurred frequently after gelation, which resulted in an enhancement of the network formation inside the gel. If the gel in the simulation is related to the domain with a higher crosslink density in this study, namely, the inhomogeneity, the intramolecular reaction in the cluster results in an increase in the degree of cross-linking of the domain.

Figure 4.6 shows schematic images representing the cross-linker amount dependence of the formation and growth of the inhomogeneity of phenolic resins. When there is an insufficient amount of cross-linkers, inhomogeneous domains with a loosely cross-linked network appear at the initial stage of gelation as shown in Figure 4.6a. The degree of cross-linking in the domain increases with the reaction time, which results in a decrease in the degree of swelling of the domain. On the other hand, when there is a sufficient amount of a cross-linker, inhomogeneous domains with a tightly cross-linked network appear at the initial stage of gelation, followed by an increase in the size of the domain as shown in

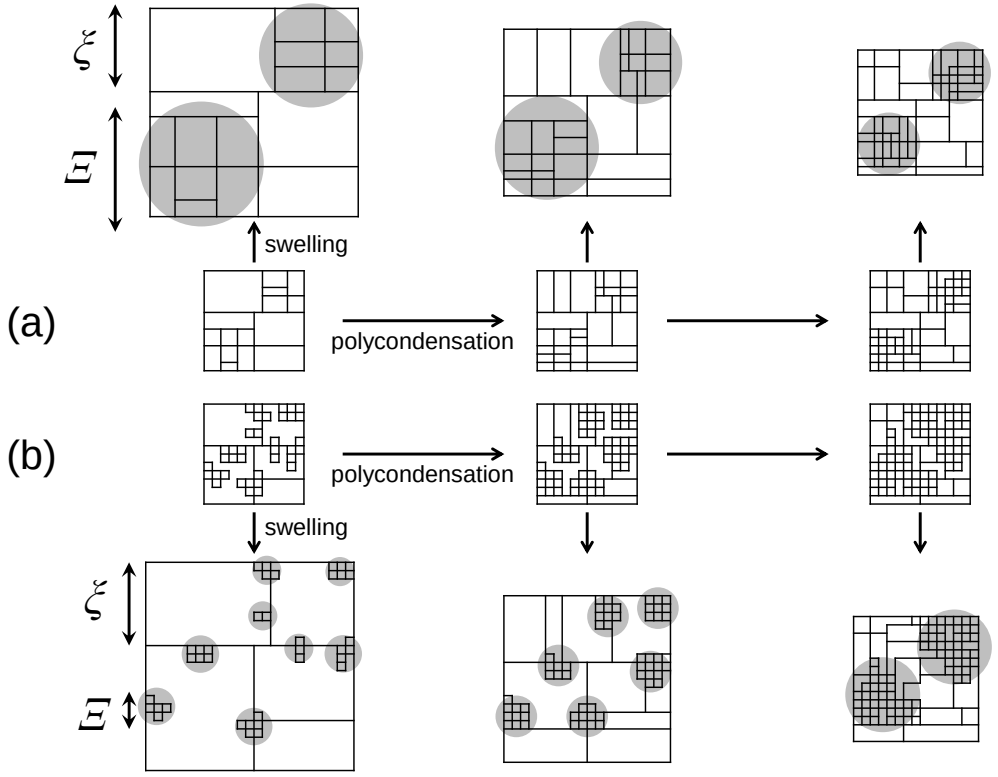

Figure 4.6 Schematic image representing the formation and growth of the inhomogeneity during the gelation process of phenolic resins with (a) an insufficient and (b) a sufficient amount of a cross-linker.

Figure 4.6b. Therefore, a decrease and an increase in Ξ with reaction time were observed because of the swelling of NV12 and NV15 in THF, respectively.

In order to clarify the mechanism causing these cross-link inhomogeneities in the phenolic resins, the influence of the $[HCHO]_0/[PhOH]_0$ value on the resulting polymer structure was examined from the viewpoint of reaction kinetics. A set of 14 rate equations for the phenol–formaldehyde polycondensation kinetics, derived by Aranguren et al.,[4] were numerically solved for the $[HCHO]_0/[PhOH]_0$ values of 1.0, 1.2, and 1.5 using the fifth-order Runge–Kutta–Fehlberg algorithm implemented in IGOR Pro 6.2.2 (WaveMetrics, Inc., USA). The calculations were performed until the gel point was reached, the

time at which the M_w value diverges to infinity. Figure 4.7 shows the evolution of the molar fractions as a function of a dimensionless reaction time (t^*). The value M_w is also plotted as a function of t^* in Figures 4.7a–c to indicate the gel point. Here, $t^* = k_{10}[\mathrm{PhOH}]_0 t$, where t indicates the reaction time and k_{10} denotes the rate constant of formaldehyde addition to an *ortho*-position of a nonsubstituted phenol.[4] As seen in Figures 4.7a–c, the gel time (i.e., t^* at the gel point) becomes shorter as the $[\mathrm{HCHO}]_0/[\mathrm{PhOH}]_0$ value increases, which can be explained by an increase in the formation rate of branched units, as shown in Figure 4.7d. However, the investigated $[\mathrm{HCHO}]_0/[\mathrm{PhOH}]_0$ values of 1.0, 1.2, and 1.5 give essentially the same evolution behavior for the molar fractions of monomer, terminal, linear, and branched phenolic units; namely, the polycondensation proceeds with (i) an increase in terminal units at the initial stage, followed by (ii) an increase in linear units accompanying a decrease in the terminal units, and last (iii) an increase in the number of branched units that results in a rapid increase in M_w. Table 4.3 shows the molar fractions and $R_{CH2/PhOH}$ at the gel point. With the exception of the molar fraction of the unreacted formaldehyde, there is no significant difference in the molar fractions at the gel point between the investigated $[\mathrm{HCHO}]_0/[\mathrm{PhOH}]_0$ values. The $R_{CH2/PhOH}$ value at the gel point increases with the $[\mathrm{HCHO}]_0/[\mathrm{PhOH}]_0$ value, a feature that is apparently different from the experimental result, as seen in Figure 4.2. These differences between the calculated and experimental results (i.e., homogeneous and inhomogeneous systems, respectively) would arise from two major assumptions in the rate equations: (i) the polycondensation proceeds with constant reactivity irrespective of the molecular weight and molecular mobility, and (ii) the formation of loops in the resulting structure owing to the intramolecular reaction is neglected. These assumptions in the reaction kinetics would suggest the mechanism causing the cross-link inhomogeneity of phenolic resins.

At this point in the discussion, there is no strong evidence to explain the mechanism causing the inhomogeneity. However, we believe that the formation of branched phenolic units could play a key role in causing the cross-link inhomogeneity; namely, the branched units decrease local segmental motion,[15]

which results in an increase in local fluctuations of the reaction rate and probability of the intramolecular reaction. A previous study of cross-linked poly(acrylamide)s demonstrated that both the segmental mobility of the polymer chain constructing the cage structure and the cage size strongly affect the mobility of water inside the cage, which was elucidated by a spin–spin relaxation time analysis using pulsed NMR measurements.[16] Therefore, the formation of cages resulting from the three-dimensional loop formation that occurred during the gelation of phenolic resins would reduce the diffusion of oligomers and unreacted formaldehyde trapped inside them. In addition, it should be noted that an increase in the initial molar ratio $[HCHO]_0/[PhOH]_0$ from 1.2 to 1.5 accompanies a significant decrease in the initial monomer concentration $[PhOH]_0$. As a result, at low monomer concentrations, the probabilities of the intramolecular reaction and the formation of small loops would increase.[17,18] This dilution effect could also be one of the major factors causing the different gelation mechanisms between NV12 and NV15. This monomer concentration dependence on the gelation mechanism of polymer gels was experimentally demonstrated by Furukawa et al. through a scanning microscopic light scattering study of poly(acrylamide) gels.[19]

For further investigation, a spin–spin relaxation time analysis using pulsed NMR and a refinement of the gelation kinetics with a stochastic approach, such as the cascade theory,[20,21] to solve the polycondensation kinetics of phenolic resins would be promising tools to help validate these conjectures regarding the mechanism causing the cross-link inhomogeneity that was observed by the ^{13}C-NMR and SAXS analyses.

Table 4.3 Molar fractions and $R_{CH2/PhOH}$ at the gel point estimated by rate equations.

$[HCHO]_0/[PhOH]_0$	HCHO	PhOH	terminal	linear	branched	$R_{CH2/PhOH}$
1.0	0.072	0.0058	0.27	0.63	0.090	0.93
1.2	0.23	0.0048	0.26	0.65	0.087	0.97
1.5	0.48	0.0042	0.26	0.65	0.085	1.02

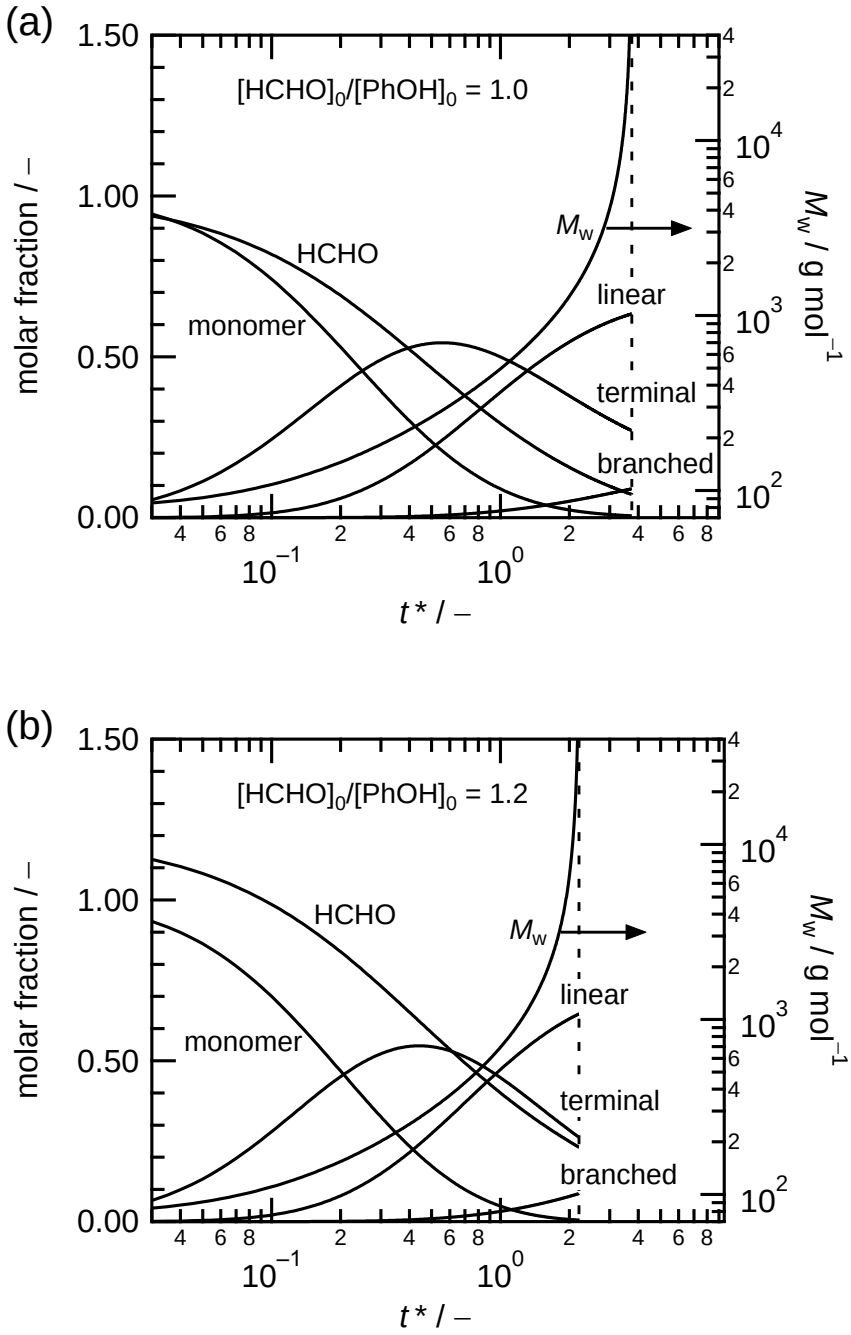

Figure 4.7 Evolution of the molar fraction and the weight-average molecular weight as a function of a dimensionless reaction time estimated by the rate equations: (a) $[HCHO]_0/[PhOH]_0$ = 1.0, (b) $[HCHO]_0/[PhOH]_0$ = 1.2, and (c) $[HCHO]_0/[PhOH]_0$ = 1.5. Dashed lines represent the gel point. (d) Molar fractions of branched phenolic units.

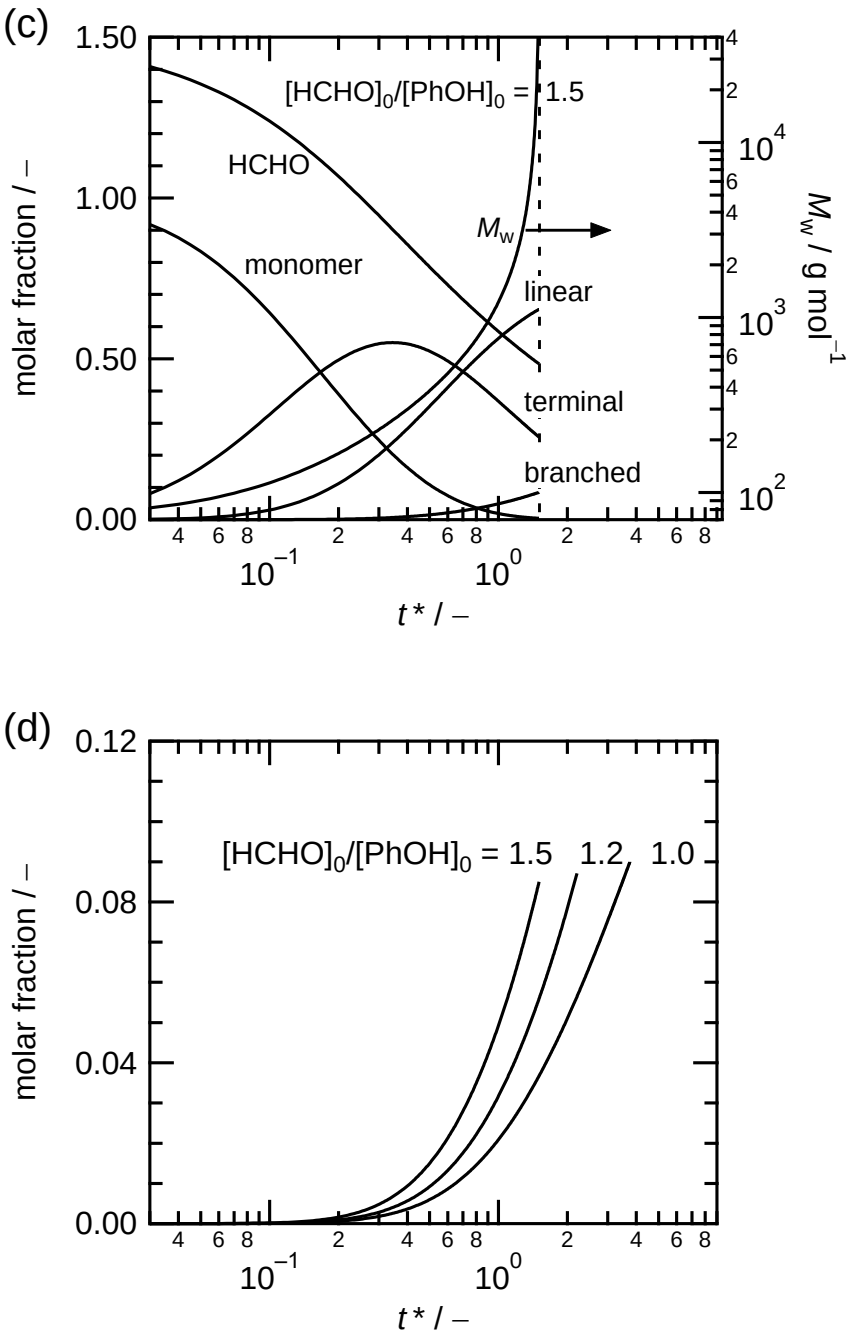

Figure 4.7 Continued.

4.4 Conclusion

To elucidate the cross-link inhomogeneity of novolac-type phenolic resins, their gelation process during polycondensation of phenol and formaldehyde with oxalic acid as an acid catalyst at 100 °C was investigated using ^{13}C-NMR and SAXS analyses. The initial molar ratios $[PhOH]_0/[HCHO]_0/[(\text{-}COOH)_2]_0$ were chosen to be 1.0/1.0/0.01 (NV10), 1.0/1.2/0.01 (NV12) (i.e., off-stoichiometric ratios) and 1.0/1.5/0.01 (NV15) (i.e., on-stoichiometric ratio).

The progress of the polycondensation irrespective of gelation was confirmed by an increase in the ratio of methylene-to-phenolic units with reaction time, which was estimated using ^{13}C-NMR spectra. The values of the ratios were less than 0.80 for NV12 and NV15 at which they became insoluble. On the other hand, that of NV10 reached 0.85 without gelation. These results can be explained by the difference in the rate of formation of branched structures, which implies the presence of different gelation mechanisms that depend on the ratio of $[HCHO]_0/[PhOH]_0$.

SAXS experiments were then performed with 7 wt% semidilute THF solutions for the soluble polymers and fully THF-swollen gels (i.e., in the semidilute state) for the insoluble polymers. The SAXS curves from the 7 wt% solutions of NV10, NV12, and NV15 in THF are well fitted by the OZ equation. On the other hand, the SAXS curves after gelation can be fitted using another function given by a combination of the OZ and SL equations, which describe liquid-like fluctuations and solid-like frozen inhomogeneity, respectively. This result indicates that there is frozen cross-link inhomogeneity in the network structure of phenolic resins. The change in the correlation length ξ of the OZ equation with reaction time indicates an increase in the size of the polymer chains before gelation and a decrease in the mesh size of the gel network after gelation. The change in the correlation length of the inhomogeneity Ξ of the SL equation indicates that the formation and growth of the inhomogeneity of phenolic resins

depends on the amount of a cross-linker; namely, there are different mechanisms when there is (i) an insufficient or (ii) a sufficient amount of a cross-linker. In case (i), inhomogeneous domains with a loosely cross-linked network appear at the initial stage of gelation. The degree of cross-linking in the domain increases with the reaction time, which results in a decrease in the degree of swelling of the domain. In case (ii), inhomogeneous domains with a tightly cross-linked network appear at the initial stage of gelation, followed by an increase in the size of the domain. We believe that the formation of branched phenolic units could play a key role in causing the cross-link inhomogeneity; namely, the branched units decrease local segmental motion, which results in an increase in local fluctuations of the reaction rate and probability of the intramolecular reaction.

4.5 References

1 T. Yamagishi, T. Nakatogawa, M. Ikuji, Y. Nakamoto and S. Ishida, *Angew. Makromol. Chem.*, 1996, **240**, 181–186.

2 H. Masunaga, H. Ogawa, T. Takano, S. Sasaki, S. Goto, T. Tanaka, T. Seike, S. Takahashi, K. Takeshita, N. Nariyama, H. Ohashi, T. Ohata, Y. Furukawa, T. Matsushita, Y. Ishizawa, N. Yagi, M. Takata, H. Kitamura, K. Sakurai, K. Tashiro, A. Takahara, Y. Amamiya, K. Horie, M. Takenaka, T. Kanaya, H. Jinnai, H. Okuda, I. Akiba, I. Takahashi, K. Yamamoto, M. Hikosaka, S. Sakurai, Y. Shinohara, A. Okada and Y. Sugihara, *Polym. J.*, 2011, **43**, 471–477.

3 F. Zhang, J. Ilavsky, G. G. Long, J. P. G. Quintana, A. J. Allen and P. R. Jemian, *Metall. Mater. Trans. A*, 2010, **41A**, 1151–1158.

4 M. I. Aranguren, J. Borrajo and R. J. J. Williams, *Ind. Eng. Chem. Prod. Res. Dev.*, 1984, **23**, 370–374.

5 T. Canal and N. A. Peppas, *J. Biomed. Mater. Res.*, 1989, **23**, 1183–1193.

6 H. E. Stanley, *Introduction to Phase Transitions and Critical Phenomena*, Oxford University Press, New York, 1971.

7 A. Izumi, T. Takeuchi, T. Nakao and M. Shibayama, *Polymer*, 2011, **52**, 4355–4361.

8 J. Bastide and S. J. Candau, Structure of gels as investigated by means of static scattering techniques. in *Physical Properties of Polymeric Gels*, ed. J. P. Cohen Addad, John Wiley, New York, 1996, pp. 143–308.

9 M. Shibayama, *Soft Matter*, 2012, **8**, 8030–8038.

10 M. Shibayama, *Macromol. Chem. Phys.*, 1998, **199**, 1–30.

11 M. Shibayama and T. Norisuye, *Bull. Chem. Soc. Jpn.*, 2002, **75**, 641–659.

12 M. Shibayama, *Polym. J.*, 2011, **43**, 18–34.

13 W. L. Wu, M. Shibayama, S. Roy, H. Kurokawa, L. D. Coyne, S. Nomura and R. S. Stein, *Macromolecules*, 1990, **23**, 2245–2251.

14 M. Shibayama, T. Karino, Y. Domon and K. Ito, *J. Appl. Cryst.*, 2007, **40**, s43–s47.

15 K. Dušek, *Polym. Gels Networks*, 1996, **4**, 383–404.

16 H. Tanaka, K. Fukumori and T. Nishi, *J. Chem. Phys.*, 1998, **89**, 3363–3372.

17 M. Dušková-Smrčková, H. Valentová, A. Ďuračková and K. Dušek, *Macromolecules*, 2010, **43**, 6450–6462.

18 K. Dušek and M. Dušková-Smrčková, *Macromol. React. Eng.*, 2012, **6**, 426–445.

19 H. Furukawa, K. Horie, R. Nozaki and M. Okada, *Phys. Rev. E*, 2003, **68**, 031406.

20 T. Nakao, F. Tanaka and S. Kohjiya, *Macromolecules*, 2002, **35**, 5649–5656.

21 T. Nakao, F. Tanaka and S. Kohjiya, *Macromolecules*, 2006, **39**, 6643–6652.

Chapter 5

Synthesis and Properties of a Deuterated Phenolic Resin

5.1 Introduction

In this chapter, we report the synthesis and properties of a highly deuterated novolac-type phenolic resin, which is intended mainly for the application of matrix resins in structural analysis of cured phenolic resins using small-angle neutron scattering (SANS).

In polymer science, fully and partially deuterated polymers have been widely used to study polymer structures and dynamics by SANS,[1] NMR, mass, IR, and Raman spectroscopies.[2,3] Of these methods, SANS uses deuterated polymers for studying of bulk polymers. This is because the use of nondeuterated and deuterated polymers increases the scattering contrast owing to the large difference in the scattering length between H and D, where the values of the coherent scattering length for H and D are -0.374×10^{-12} and 0.667×10^{-12} cm, respectively.[1] In many cases, deuterated polymers are chosen as matrix materials to reduce the background noise derived from incoherent scattering, where the values of the incoherent scattering cross section for H and D are 79.9×10^{-24} and 2.04×10^{-24} cm^2, respectively.[1]

Three typical methods used to prepare deuterated polymers are as follows: (i) polymerization of deuterated monomers;[4–6] (ii) H–D exchange

reaction of nondeuterated polymers;[7,8] and (iii) deuteration of unsaturated polymers by gaseous D_2.[9] Method (i) is advantageous from the viewpoint that existing synthetic facilities and procedures for nondeuterated polymers can be used only if deuterated monomers are available. However, there may be differences in the molecular weight distribution and tacticity between polymers that are prepared from deuterated and nondeuterated monomers because of the deuterium isotope's effects on polymerization.[10] Method (ii) is the most convenient because the reaction procedure only involves stirring a mixture of nondeuterated polymers, D_2O or gaseous D_2, and a metal catalyst.[11] However, it is difficult to obtain fully deuterated polymers because of the difference in the reactivity of each hydrogen atom of the nondeuterated polymers. Also, in some cases, this reaction requires high temperature and pressure (i.e., > 200 °C and > 1 MPa), which could cause undesirable side effects including polymer degradation. A change in the molecular weight distribution was reported even for the reaction at room temperature.[12] Method (iii) is useful for the preparation of polymers by hydrogenation of unsaturated polymers, but it is not applicable to most polymers.

In this chapter, we report the synthesis and properties of the highly deuterated novolac-type phenolic resin prepared using method (i) by the polycondensation of deuterated phenol and formaldehyde using oxalic acid as an acid catalyst. This deuterated phenolic resin is intended mainly for the application of matrix resins in the SANS analysis on the thermosetting resins. However, this resin is also expected to be applicable to broader studies of polymer physics of thermosetting resins, such as polymer chain dynamics and miscibility of polymer blends. Previous reports on deuterated phenolic resins are limited to partially deuterated resol-type phenolic resins prepared under basic conditions[13,14] and novolac-type resins containing partially deuterated hydroxyl groups[15,16] for the structural analysis of curing, carbonization, pyrolysis, and dissolution behaviors of phenolic resins by NMR, IR, and mass spectroscopies. To our knowledge, this is the first report on highly deuterated novolac-type phenolic resins.

5.2 Experimental

5.2.1 Materials

Phenol-d_6 (PhOD, 98.9 atom % D), 20 wt% formaldehyde-d_2 (DCDO, 99.8 atom % D) in D_2O, and dimethylsulfoxide-d_6 (DMSO-d_6) were purchased from C/D/N isotopes Inc., Canada. Ethanol-d_6 (EtOH-d_6) was purchased from Cambridge Isotope Laboratories, Inc., USA. Phenol (PhOH), 37 wt% formaldehyde (HCHO) in H_2O, and oxalic acid were purchased from Wako Pure Chemical Industries, Ltd., Japan. A nondeuterated random novolac-type phenolic resin (NVH, supplier's product number: PR-51305) was provided by Sumitomo Bakelite Co., Ltd., Japan. Hexamethylenetetramine (HMTA) was purchased from Chang Chun PetroChemical Co., Ltd., Taiwan. All materials were used without further purification.

The weight-average molecular weight (M_w) and the number-average molecular weight (M_n) of NVH were estimated to be 5470 g mol^{-1} and 950 g mol^{-1}, respectively, under the following gel permeation chromatography (GPC) measurement conditions. The bulk density (d) of NVH was estimated to be 1.23 g cm^{-3}.

5.2.2 Polymerization

A solution containing PhOD (44.0 g, 439 mmol), 20 wt% DCDO in D_2O (63.4 g, 396 mmol), and oxalic acid (0.385 g, 4.28 mmol) in a 200 mL round-bottom flask equipped with a reflux condenser and a vacuum distillation head was stirred at 90 °C for 120 min, at 100 °C (reflux) for 180 min under nitrogen, and then at 120 °C for 30 min under reduced pressure to remove D_2O. The resulting polymer was collected and dried in vacuum at 150 °C for 120 min to remove the volatiles including unreacted monomers to give NVD (42.2 g) as a colorless solid. M_w / g mol^{-1}: 9200; M_n / g mol^{-1}: 1180; d / g cm^{-3}: 1.29; IR / cm^{-1}: 3500, 3329, 2598, 2459, 2257, 2190, 2087, 1588, 1570, 1431, 1395, 1310, 1169, 818, 789, 677.

5.2.3 Measurements

5.2.3.1 General

FT-IR spectra were recorded on a Shimadzu FTIR-8900 spectrophotometer with KBr pellet. ^{1}H-NMR spectra were recorded on a JEOL JNM-GSX-400 spectrometer in DMSO-d_6 solution at 400 MHz. ^{13}C-NMR spectra were recorded on a JEOL JNM-AL-300 spectrometer in 25 wt% EtOH-d_6 solution at 75 MHz. Differential scanning calorimetry (DSC) measurements were performed on a Rigaku DSC-8320 instrument using a sealable aluminum pan (SSC000E031, Seiko Instruments, Inc., Japan) as a sample vessel. Samples were first cooled to 10 °C, and then heated to 200 °C at a heating rate of 5 °C min^{-1}. The DSC thermograms were recorded from 30 °C to 190 °C. The bulk densities of the phenolic resins were calculated from the weight and volume of disk-shaped specimens prepared by compression molding at 60 °C under a pressure of 40 MPa.

5.2.3.2 GPC

GPC analyses for the evaluation of M_w and M_n were performed on a Tosoh HLC-8120 system equipped with six poly(styrene-*co*-divinylbenzene) gel columns (TSKgel SuperHZM-M, HZ3000, HZ2000, HZ2000, HZ2000, and HZ1000) and a differential refractive index detector. THF at 40 °C was used as the eluent. The molecular weight was calculated with a calibration line that was obtained by fitting the peak molecular weights of 18 polystyrene (PSt) standards using a cubic function. The peak molecular weights of PSt standards were 1.09 × 10^6, 7.06 × 10^5, 3.55 × 10^5, 1.90 × 10^5, 9.64 × 10^4, 3.79 × 10^4, 1.81 × 10^4, 9100, 5970, 2630, 994, 786, 682, 578, 474, 370, 266, and 162 g mol^{-1}. The polymer concentration of the injection solution was 0.2 wt%. The polymer solution was filtered through a 0.45 μm filter (Tosoh H-13-5) before injection into the chromatograph.

GPC analyses for the evaluation of intrinsic viscosity and absolute molecular weight were performed on a Tosoh HLC-8220 system equipped with

three poly(styrene-*co*-divinylbenzene) gel columns (Shodex KF-805L, KF-805L, and KF-800D) and a Viscotek Model 302 triple detector array consisting of a differential refractive index detector, a four-capillary differential viscometer, and a low-angle laser light scattering (LALLS) detector. The LALLS measurement was performed at a scattering angle of 7° using a laser light with a wavelength of 670 nm. THF at 40 °C was used as the eluent. The polymer concentration of the injection solution was 0.5 wt% and the polymer solution was filtered through a 0.2 μm filter before injection into the chromatograph.

5.2.3.3 SANS

SANS experiments were performed on the SANS-U spectrometer belonging to the Institute for Solid State Physics, the University of Tokyo, which is installed in the Guide Hall of the JRR-3 Research Reactor of Japan Atomic Energy Agency in Tokai, Ibaraki, Japan.[17–19] A monochromated cold neutron beam with an average neutron wavelength of 7.0 Å and 10% wavelength distribution was used to irradiate the samples at room temperature. The diameter of the neutron beam at the sample position was 15 mm. The scattered neutrons were counted by a two-dimensional position detector (2660N, Ordela, USA). The sample-to-detector distance and collimation length were chosen to be 1 and 4 m, respectively. After necessary corrections for open beam scattering, transmittance, and detector inhomogeneities, the corrected scattering intensity functions were normalized to the absolute intensity scale using a polyethylene secondary standard.

The samples for SANS measurements were prepared by compression molding of a mixture of the phenolic resin and HMTA at 165 °C for 20 min under a pressure of 40 MPa. The contents of HMTA in the stoichiometric mixture with NVH and NVD were 12.0 and 11.1 wt%, respectively. NVD without HMTA was also molded at 60 °C. Molded resins containing HMTA were further cured at 175 °C for 6 h. The thickness and diameter of the disk-shaped molded resins were approximately 1 and 24 mm, respectively.

5.3 Results and Discussion

5.3.1 Polymerization

NVD was prepared by the polycondensation of PhOD and DCDO using oxalic acid as a catalyst as shown in Figure 5.1 with a molar ratio of PhOD/DCDO/oxalic acid of 1/0.9/0.01. The critical molar ratio of formaldehyde-to-phenol, which leads to gelation, is theoretically estimated to be 0.90 assuming full formaldehyde conversion[20] and is experimentally proven to produce high-molecular weight novolac-type phenolic resins without gelation.[21] In this study, this value for the molar ratio of PhOD/DCDO was chosen to obtain a high-molecular weight resin. To evaluate the effect of deuteration on the molecular weight distribution, the polycondensation of nondeuterated monomers was also performed under synthetic conditions similar to those used in the NVD synthesis.

Figure 5.2 shows the GPC chromatograms of these reaction mixtures at polymerization times of 130, 190, and 250 min. All chromatograms exhibit 5 peaks at retention times ranging from 29 to 24 min, which correspond to monomer (phenol), dimer (hydroxyphenylmethylphenol), trimer (bis(hydroxyphenylmethyl)phenol), tetramer, and pentamer. This clearly indicates that the polycondensation of phenol and formaldehyde with oxalic acid proceeds irrespective of the deuteration of monomers. In general, deuteration affects the

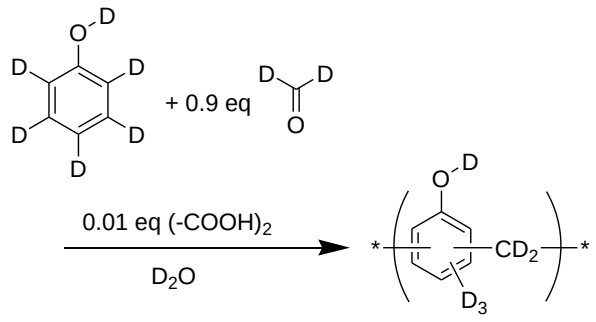

Figure 5.1 Synthesis of a highly deuterated novolac-type phenolic resin.

rate of the reaction,[10,22–24] which was inferred from the difference in the initial monomer conversion rate that is estimated by the area of the peak at the retention time of 29 min in the chromatogram. However, there was no significant difference between the chromatograms of the reaction mixtures at a polymerization time of 250 min. These results indicate that the phenolic resin obtained by the polycondensation of PhOD and DCDO with oxalic acid has essentially the same molecular weight distribution as the typical novolac-type phenolic resins.

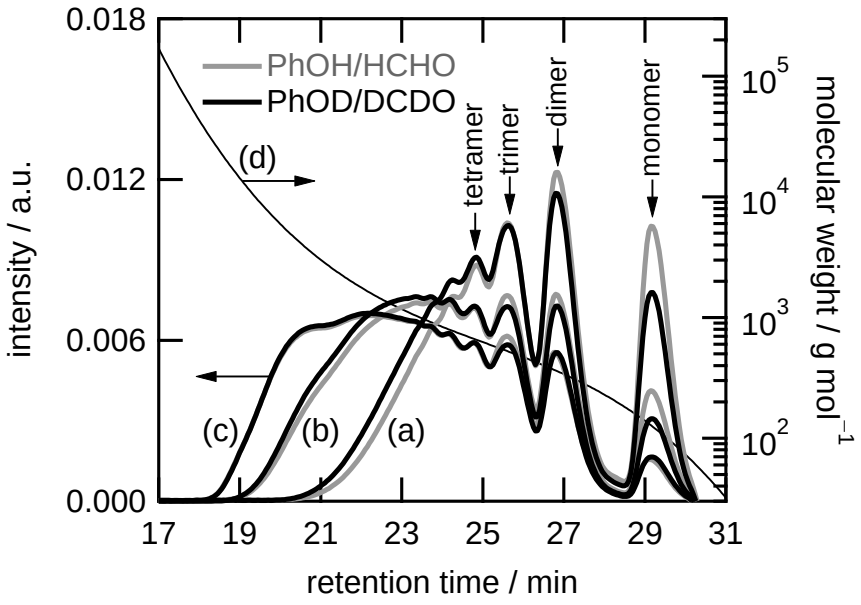

Figure 5.2 GPC chromatograms of the reaction mixture at different polymerization times: (a) 130 min; (b) 190 min; and (c) 250 min. All curves were normalized with respect to the total chromatogram area. (d) Calibration line based on PSt standards.

5.3.2 Structure and Conformation

Figure 5.3 shows the ^{13}C-NMR spectra of NVH and NVD in EtOH-d_6 with a polymer concentration of 25 wt%. The ^{13}C-NMR signals at 31, 36, and 41 ppm correspond to the methylene carbons of *o–o′*, *o–p′*, and *p–p′* linkages, respectively.[25–27] By integrating the peak areas, the molar ratio of *o–o′*/*o–p′*/*p–p′* methylene linkages in NVH and NVD were statistically estimated to be 27/51/22 and 31/45/24, respectively. This result indicates that NVD has the configuration of random novolac-type phenolic resins such as NVH.

Figure 5.4 shows the ^{1}H-NMR spectra of NVH and NVD in DMSO-d_6 with a polymer concentration of 4.3 wt%. The intensity was normalized with respect to the peak area of the hydrogen of DMSO at 2.4–2.7 ppm. The ^{1}H-NMR signals of NVH at 10–8.5, 8–6.5, and 4–3 ppm correspond to the hydrogen of Ar–O*H*, Ar–*H*, and Ar–C*H*, respectively. The signals of Ar–*H* and Ar–C*H* for NVD were slightly observed, and taking NVH as a nondeuterated reference sample, the degree of deuteration of NVD was estimated to be 98% and 99% for the deuterium of Ar–*D* and Ar–C*D*, respectively. These values reasonably agree with the degree of deuteration for PhOD and DCDO. This result indicates that this preparation procedure does not accompany the D-to-H exchange reaction at Ar–*D* and Ar–C*D*. On the other hand, the ^{1}H-NMR signal of Ar–O*H* was clearly observed in the spectra of NVD, and the degree of deuteration was estimated to be 21% for Ar–O*D*. This is probably due to either (i) the existence of H_2O in DMSO-d_6, which was observed at 3.4 ppm in the spectra or (ii) the moisture in the air, which led to the D-to-H exchange reaction at the hydroxyl groups during NMR measurement or sample handling, because the H–D exchange reaction at the hydroxyl group of the phenol proceeds quite easily.[16]

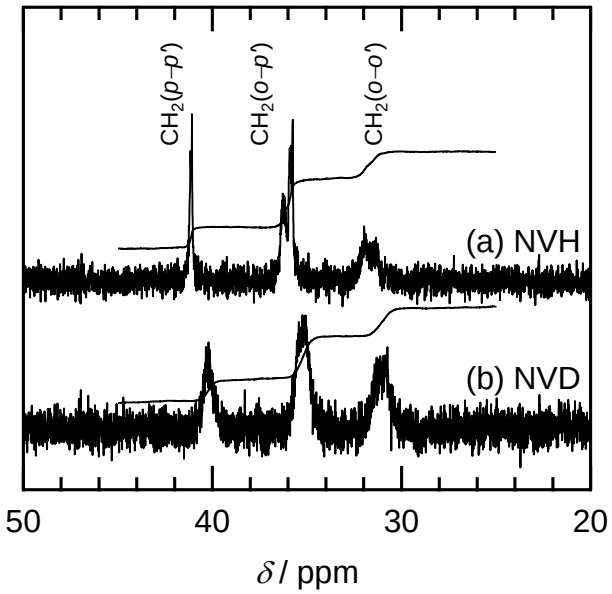

Figure 5.3 ^{13}C-NMR spectra measured in EtOH-d_6: (a) NVH and (b) NVD.

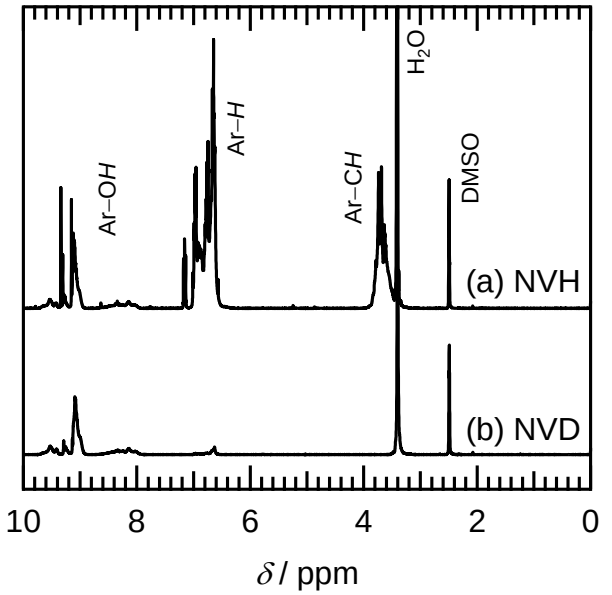

Figure 5.4 ^{1}H-NMR spectra measured in DMSO-d_6: (a) NVH and (b) NVD. The ^{1}H-NMR spectra were normalized with respect to the peak area of the hydrogen of DMSO at 2.4–2.7 ppm.

Figure 5.5 shows the IR spectra for NVH and NVD. For the spectrum of NVD, the IR absorptions that are characteristic of deuterated organic materials were clearly observed in the range from 2700 to 2000 cm^{-1}, which correspond to the O–D and C–D bond stretching vibrations. This is explained by a low-wavenumber shift of the O–H and C–H bond stretching vibrations that are observed in the range from 3700 to 2800 cm^{-1} in the spectrum of NVH, because exchanging H for D in NVH is accompanied by an increase in the reduced mass (μ) of the bond, given by $\mu = (m_1\, m_2) / (m_1 + m_2)$ for atoms with masses m_1 and m_2, which, according to the Hooke's law approximation, leads to a decreased wavenumber, that is, the wavenumber of a bond stretching vibration is proportional to the inverse square root of μ. Thus, the wavenumber of the O–H and C–H bond stretching vibration decreases by a factor of 0.73 by exchanging H

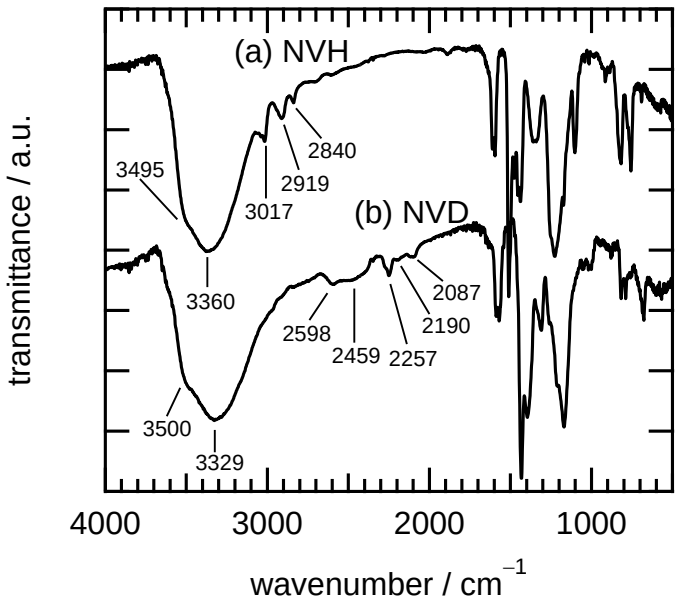

Figure 5.5 FT-IR spectra measured with KBr pellet: (a) NVH and (b) NVD.

for D, assuming that the force constant does not change. As observed in the ^{1}H-NMR spectrum of NVD in Figure 5.4, the nondeuterated hydroxyl group in NVD was also observed as the O–H bond stretching vibration in the range from 3700 to 3000 cm^{-1}. This is probably the result of the D-to-H exchange reaction at Ar–O*D* due to the moisture in the air during handling of the sample, as mentioned above.

Figure 5.6 shows the plots of intrinsic viscosity ([η]) as a function of the absolute molecular weight (M) of NVH and NVD, known as the Mark–Houwink–Sakurada (MHS) plot. Previous studies revealed that novolac-type phenolic resins prepared by the acid-catalyzed polycondensation reaction exhibit a more compact sphere-like conformation than that of a Gaussian chain in good solvents such as acetone and THF.[26,28–32] This solution behavior was clarified by evaluating the scaling exponent (a) in the MHS equation given by [η]

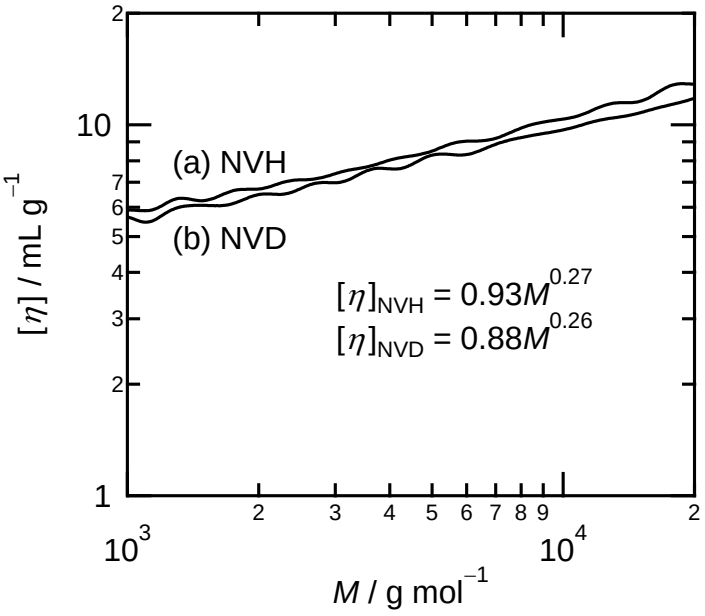

Figure 5.6 Mark–Houwink–Sakurada plot in THF at 40 °C: (a) NVH and (b) NVD.

$= KM^a$, where K denotes the constant that depend on the polymer, solvent, and temperature. According to this equation, a polymer having an a value of 0.5 behaves like a Gaussian chain. If the conformation of a polymer is compact or short in comparison with that of a Gaussian chain, the value of a becomes smaller than 0.5. Previously reported values of K and a for random novolac-type phenolic resins in THF solution were 0.80 and 0.28 at 30 °C by Kamide et al.,[30] 0.637 and 0.28 at 25 °C by Sue et al.,[31] and 0.63 and 0.25 at 25 °C by Yamagishi et al.[26] These studies were achieved using phenolic resins with a narrow molecular weight distribution (i.e., $M_w/M_n < 1.2$), which were obtained by a careful solution fractionation technique using a solvent/nonsolvent system. In this study, using GPC as a polymer separation method, a K value of 0.93 and an a value of 0.27 in THF at 40 °C were obtained for NVH by fitting the data with a power law function. The agreement with the reported values supports the validity of this method. It must be noted that the wavelike lines in Figure 5.6 were due to the characteristics of the measurement device, especially in the low-molecular weight region ($M < 10^4$ g mol^{-1}). Then, for NVD, a K value of 0.88 and an a value of 0.26 were obtained. These results indicate that both NVD and NVH behave like compact spheres in THF, and this characteristic feature of random novolac-type phenolic resins is not affected by deuteration. The $[\eta]$ obtained for NVD was 10–12% smaller than that obtained for NVH as seen in Figure 5.6, and is expected owing to the fact that the hydrodynamic specific volume of NVD is 5% smaller than that of NVH, as estimated from the difference in the bulk density. This is because $[\eta]$ is proportional to the specific volume of the polymer, which is the inverse of density.[33] The decrease in $[\eta]$ and increase in the density by deuteration were also reported for deuterated hydrogeneted-polybutadienes.[7]

5.3.3 Curing Behavior

Figure 5.7 shows DSC heating curves for NVH, NVD, HMTA, and their mixtures ranging from 30 to 190 °C. HMTA is a typical curing agent for phenolic resins[34] and is thermally stable within this temperature range, as seen in the figure. NVH exhibits endothermic behavior owing to the melting of the polymer and

exothermic behavior only in the presence of HMTA because of the cross-linking reaction. These typical behaviors of nondeuterated phenolic resins were also observed in the case with NVD. This result suggests that the curing reaction of phenolic resins with HMTA takes place irrespective of deuteration. The differences in endothermic and exothermic peak temperatures between NVH and NVD may be due to both deuteration as well as slight differences in the amount of absorbed moisture[34,35] and the local configuration of *o–o'*, *p–o'*, and *p–p'* methylene linkages,[27] which generally affect the thermal properties of phenolic resins.[13] The differences in the bulk density and viscosity of NVH and NVD may also affect the thermal behavior. However, currently, there is no experimental result that clearly characterizes the difference between the thermal behavior of NVH and NVD.

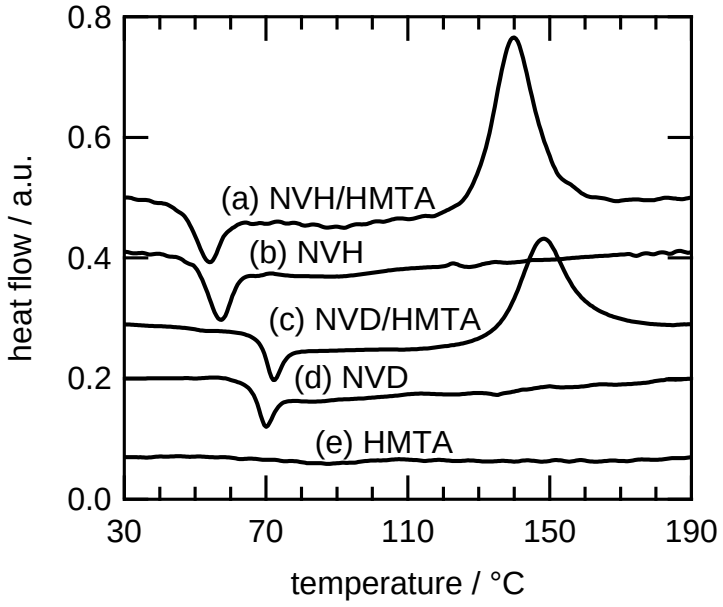

Figure 5.7 DSC thermograms obtained using a capsuled aluminum pan as a sample vessel at a heating rate of 5 °C min^{-1}: (a) a 1/0.1 (wt/wt) mixture of NVH/HMTA; (b) NVH; (c) a 1/0.1 (wt/wt) mixture of NVD/HMTA; (d) NVD; and (e) HMTA.

5.3.4 SANS

Figure 5.8 shows the observed SANS intensities in an absolute scale that includes incoherent neutron scattering background in the q range from 0.5 to 2.5 nm^{-1}, where $q = (4\pi/\lambda)\sin(2\theta/2)$ signifies the magnitude of the scattering vector, and λ and 2θ denote the neutron wavelength and scattering angle, respectively. Measured samples were NVD as a highly deuterated phenolic resin, NVD/HMTA as a partially deuterated cured phenolic resin, and NVH/HMTA as a nondeuterated cured phenolic resin, where the amount of HMTA was stoichiometric to that of the uncured phenolic resin. As seen in this figure, the SANS signals in this q range are dominated by the q-independent incoherent scattering. This was observed even for NVD/HMTA in which nondeuterated HMTA is distributed in the deuterated matrix. This suggests that the cross-links that are derived from HMTA are randomly distributed throughout the network structure of phenolic resins, and phenolic resins exhibit no distinct structure in this SANS region (i.e., in the range from 12 to 2.5 nm, which is given by $2\pi/q$). This conclusion is achieved by

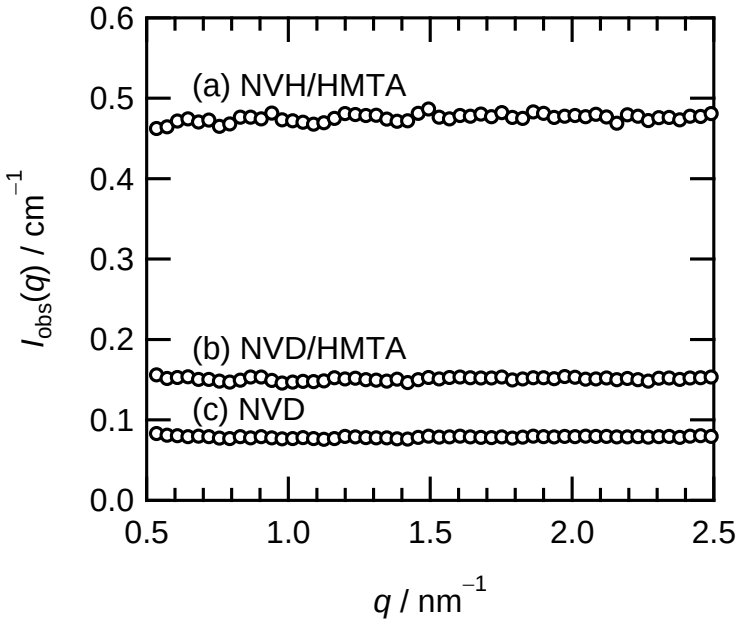

Figure 5.8 SANS curves including the incoherent scattering background: (a) a cured resin prepared from a stoichiometric mixture of NVH/HMTA; (b) a cured resin prepared from a stoichiometric mixture of NVD/HMTA; and (c) NVD.

providing a neutron scattering contrast between the curing agent and matrix resins and lowering the incoherent background of the system using the highly deuterated phenolic resin. The details of the structural analysis of phenolic resins by SANS will be reported in Chapter 6.[36] These results indicate that NVD and NVD/HMTA are suitable for the SANS study of thermosetting resins as matrices with low incoherent backgrounds.

5.4 Conclusions

The highly deuterated random novolac-type phenolic resin was prepared by the polycondensation of deuterated phenol and formaldehyde using oxalic acid as an acid catalyst. The polycondensation of deuterated monomers was confirmed by GPC analysis, and the molecular weight distribution of the resulting deuterated polymer was similar to that of the nondeuterated polymer prepared under the same synthetic conditions. The IR and ^{1}H-NMR spectra supported the formation of the highly deuterated phenolic resin. With the exception of the hydroxyl groups, the degree of deuteration except for the hydroxyl groups was estimated to be more than 98% by the ^{1}H-NMR analysis. The molar ratio of *o–o′*/*o–p′*/*p–p′* methylene linkages was estimated to be 31/45/24 by the ^{13}C-NMR analysis.

The polymer conformation in THF at 40 °C was evaluated from the scaling exponent of the MHS equation, and the exponent of 0.26 was obtained for the deuterated phenolic resin. This value is close to our experimental value and the previously reported values for nondeuterated phenolic resins, which suggests that phenolic resins in THF behave like a compact sphere irrespective of deuteration. From DSC analysis, the curing reaction of phenolic resins with hexamethylenetetramine took place irrespective of deuteration. The cured deuterated phenolic resin exhibits a lower incoherent neutron scattering background than that of the nondeuterated phenolic resin. These results confirm that this highly deuterated phenolic resin is suitable for matrix resins with low incoherent backgrounds for the SANS study of the thermosetting resins. We

believe this deuterated phenolic resin can also be applied to broader studies regarding the polymer physics of thermosetting resins such as polymer chain dynamics and miscibility of polymer blends.

5.5 References

1 R. J. Roe, *Methods of X-ray and Neutron Scattering in Polymer Science*, Oxford University Press, New York, 2000.

2 J. L. Koeing, *Spectroscopy of Polymers*, 2nd edn., Elsevier Science, New York, 1999.

3 R. Kimmich and N. Fatkullin, *Adv. Polym. Sci.*, 2004, **170**, 1–113.

4 D. M. White and S. A. Nye, *Macromolecules*, 1984, **17**, 2643–2645.

5 S. Murahashi, S. Nozakura and K. Yasufuku, *Bull. Chem. Soc. Jpn.*, 1964, **37**, 854–859.

6 A. Izumi, T. Nakao and M. Shibayama, *J. Polym. Sci., Part A: Polym. Chem.*, 2011, **49**, 4941–4947.

7 J. D. Tanzer and B. Crist, *Macromolecules*, 1985, **18**, 1291–1294.

8 J. C. Nicholson and B. Crist, *Macromolecules*, 1989, **22**, 1704–1708.

9 B. Crist, W. W. Graessley and G. D. Wignall, *Polymer*, 1982, **23**, 1561–1567.

10 H. Simon and D. Palm, *Angew. Chem. Int. Ed.*, 1966, **5**, 920–933.

11 J. Atzrodt, V. Derdau, T. Fey and J. Zimmermann, *Angew. Chem. Int. Ed.*, 2007, **46**, 7744–7765.

12 B. Willenberg, *Makromol. Chem.*, 1976, **177**, 3625–3628.

13 E. C. Kelusky, C. A. Fyfe and M. S. Mckinnon, *Macromolecules*, 1986, **19**, 329–332.

14 L. Prókai, *Acta. Chim. Hung.*, 1987, **124**, 901–905.

15 M. S. Kim and A. Reiser, *Macromolecules*, 1997, **30**, 4652–4655.

16 Y. Yamashita and K. Ouchi, *Carbon*, 1981, **19**, 89–94.

17 S. Okabe, M. Nagao, T. Karino, S. Watanabe, T. Adachi, H. Shimizu and

M. Shibayama, *J. Appl. Cryst.*, 2005, **38**, 1035–1037.

18 S. Okabe, T. Karino, M. Nagao, S. Watanabe and M. Shibayama, *Nucl. Instrum. Methods Phys. Res., Sect. A*, 2007, **572**, 853–858.

19 H. Iwase, H. Endo, M. Katagiri and M. Shibayama, *J. Appl. Cryst.*, 2011, **44**, 558–568.

20 M. I. Aranguren, J. Borrajo and R. J. J. Williams, *Ind. Eng. Chem. Prod. Res. Dev.*, 1984, **23**, 370–374.

21 T. Yamagishi, M. Nomoto, S. Ito, S. Ishida and Y. Nakamoto, *Polym. Bull.*, 1994, **32**, 501–507.

22 J. Bigeleisen, *J. Chem. Phys.*, 1949, **17**, 675–678.

23 L. Melander, *Isotope Effects on Reaction Rates*, Ronald Press, New York, 1960.

24 V. J. Shiner, H. R. Mahler, R. H. Baker and R. R. Hiatt, *Ann. N. Y. Acad. Sci.*, 1960, **84**, 583–595.

25 S. A. Sojka, R. A. Wolfe, E. A. Dietz and B. F. Dannels, *Macromolecules*, 1979, **12**, 767–770.

26 T. Yamagishi, M. Nomoto, S. Yamashita, T. Yamazaki, Y. Nakamoto and S. Ishida, *Macromol. Chem. Phys.*, 1998, **199**, 423–428.

27 M. Nomoto, Y. Fujikawa, T. Komoto and T. Yamanobe, *J. Mol. Struct.*, 2010, **976**, 419–426.

28 S. Ishida, M. Nakagawa, H. Suda and K. Kaneko, *Koubunshi Kagaku*, 1971, **28**, 250–253.

29 F. L. Tobiason, C. Chandler and F. E. Schwarz, *Macromolecules*, 1972, **5**, 321–325.

30 K. Kamide and Y. Miyakawa, *Makromol. Chem.*, 1978, **179**, 359–372.

31 H. Sue, Y. Nakamoto and S. Ishida, *Polym. Bull.*, 1989, **21**, 97–104.

32 T. Yamagishi, H. Kumagai, T. Hasegawa, Y. Nakamoto and S. Ishida, *Polym. Int.*, 1995, **36**, 333–338.

33 P. Debye and A. M. Bueche, *J. Chem. Phys.*, 1948, **16**, 573–579.

34 A. Gardziella, L. A. Pilato and A. Knop, *Phenolic Resins: Chemistry, Applications, Standardization, Safety and Ecology*, 2nd completely rev.

edn., Springer, Berlin, 1999.

35 R. Burns and E. W. Orrell, *J. Mater. Sci.*, 1967, **2**, 72–77.

36 A. Izumi, T. Nakao, H. Iwase and M. Shibayama, *Soft Matter*, 2012, **8**, 8438–8445.

Chapter 6

Structural Analysis of Cured Phenolic Resins Using Complementary Small-angle Neutron and X-ray Scattering and Scanning Electron Microscopy

6.1 Introduction

For elucidating the inhomogeneity of gel networks, dynamic light scattering (DLS), small-angle neutron and X-ray scattering (SANS and SAXS, respectively) have been proven to be powerful techniques.[1–3] For the study of thermosetting resins, such scattering techniques have typically been applied to the analysis of the phase separation of thermosetting and thermoplastic polymer blends,[4–6] the aggregation and distribution of nanometer-sized reinforcing fillers in nanocomposites,[7–9] and the pore structure of carbon.[10–13] However, only a few researches have addressed the inhomogeneity of thermosetting resins using these methods and there is no report that uses both SANS and SAXS in the study of the inhomogeneity of thermosetting resins. The use of both neutrons and X-rays in small-angle scattering observations can provide complementary, powerful structural information because of the differences in scattering phenomena between the two; namely, neutrons and X-rays are scattered by individual atomic nuclei and electrons, respectively. SANS and SAXS spectra result from the fluctuations

of the neutron and X-ray scattering length densities (ρ_n and ρ_x), respectively. For SANS, the use of deuterated and nondeuterated species increases the neutron scattering contrast (i.e., the difference in ρ_n) because of a large difference in the coherent neutron scattering length between hydrogen and deuterium (i.e., -3.74×10^{-13} and 6.67×10^{-13} cm, respectively). For SAXS, with the exception of studies that utilize multiple X-ray energies (such as anomalous small-angle X-ray scattering that uses different incident X-ray energies close to an absorption edges of specific elements),[14,15] ρ_x is approximated to be a nonresonant term independent of the X-ray energy and is given by $\rho_x = \rho_e I_e$. Here ρ_e denotes the electron density, and I_e denotes the coherent scattering amplitude of a single electron and is equal to the classical radius of an electron (i.e., 2.82×10^{-13} cm). Therefore, an evaluation of the relationship between the fluctuations of ρ_n and ρ_x through complementary SANS and SAXS observations provide firm structural information that cannot be obtained solely from either of them.

In this chapter, we report the observations from complementary SANS, SAXS, and SEM for cured, partly deuterated phenolic resins to elucidate their cross-link inhomogeneity.

6.2 Experimental

6.2.1 Materials

Phenol-d_6 (98.9 atom % D) and 20 wt% formaldehyde-d_2 (99.8 atom % D) in D_2O were purchased from C/D/N isotopes Inc., Canada. Oxalic acid and hexamethylenetetramine (HMTA) were purchased from Wako Pure Chemical Industries, Ltd., Japan and Chang Chun Petrochemical Co., Ltd., Taiwan, respectively. All materials were used without further purification.

6.2.2 Sample Preparation

A highly deuterated novolac-type phenolic resin oligomer (NVD) was

prepared by polycondensation of deuterated phenol and formaldehyde using oxalic acid as an acid catalyst.[16] A solution containing phenol-d_6 (44.0 g, 439 mmol), 20 wt% formaldehyde-d_2 in D_2O (63.4 g, 396 mmol), and oxalic acid (0.385 g, 4.28 mmol) in a 200 mL round-bottom flask equipped with a reflux condenser and a vacuum distillation head was stirred at 90 °C for 120 min, at 100 °C (reflux) for 180 min under nitrogen, and then at 120 °C for 30 min under reduced pressure to remove D_2O. The resulting polymer was collected and dried in vacuum at 150 °C for 120 min to remove the volatiles including unreacted monomers to give NVD (42.2 g) as a colorless solid with a bulk density (d) of 1.29 g cm^{-3}, where the value d was calculated from the weight and volume of a disk-shaped specimen NVD00 that is described later in this subsection. The values of the weight- and number-average molecular weights (M_w and M_n) were 9200 and 1180 g mol^{-1}, respectively, and were estimated by gel permeation chromatography in THF at 40 °C (performed on a Tosoh HLC-8120 system with a PSt calibration line). The degree of deuteration, with the exception of the hydroxyl groups, was more than 98%, and that of hydroxyl groups was 21%, as estimated from the ^{1}H-NMR spectra recorded on a JEOL JNM-GSX-400 spectrometer in a dimethylsulfoxide-d_6 solution at 400 MHz. Assuming NVD has a linear structure, the average degree of polymerization is estimated to be 10.71, as calculated from the M_n and the degree of deuteration. Further details on the synthesis and characterization of the resin were previously reported in Chapter 5.[16]

The disk-shaped specimens NVD00, NVD05, and NVD10 for SANS, SAXS, and SEM measurements were prepared by compression molding of 0/1, 0.0627/1, and 0.125/1 (w/w) HMTA/NVD mixtures, respectively, where 0.125/1 is a stoichiometric ratio. The 0.0627/1 and 0.125/1 mixtures were molded at 165 °C for 20 min under a pressure of 40 MPa, followed by curing at 175 °C for 6 h under atmospheric pressure, while the 0/1 mixture was molded at 60 °C for 20 min under a pressure of 40 MPa. The thickness and diameter of molded resins were approximately 1 and 24 mm, respectively.

6.2.3 SANS

SANS experiments were performed on the SANS-U spectrometer belonging to the Institute for Solid State Physics, the University of Tokyo, which is installed in the Guide Hall of the JRR-3 Research Reactor of Japan Atomic Energy Agency in Tokai, Ibaraki, Japan.[17–19] A monochromated cold neutron beam with an average wavelength (λ) of 7.0 Å and 10% wavelength distribution was used to irradiate the samples at room temperature. The diameter of the neutron beam at the sample position was 15 mm. A pinhole collimation system (pinhole SANS) was used at sample-to-detector distances (SDD) of 1.0, 4.0, and 12.0 m. The collimation lengths were 4, 4, and 12 m for the SDD of 1.0, 4.0, and 12.0 m, respectively. The scattered neutrons were counted by a two-dimensional (2D) position sensitive detector (PSD) (2660N, Ordela, USA), which has an effective area for neutron detection of 645 × 645 mm, and a spatial resolution of 5.0 × 5.0 mm. A focusing collimation system (focusing SANS) with a collimation length of 12 m was also employed at an SDD of 11.3 m using a 2D high-resolution scintillation PSD consisting of a cross-wired position sensitive photomultiplier tube (R3239, Hamamatsu Photonics K. K., Japan) combined with a ZnS/^{6}LiF scintillator (effective area for neutron detection of 74 mmφ and a spatial resolution of 0.45 × 0.45 mm).[19] A stack of 55 biconcave MgF_2 neutron lenses was used to focus neutron beams.[20,21] After necessary corrections for dark current, background scattering, transmittance, and detector inhomogeneities, the corrected scattering intensity functions were normalized to the absolute intensity scale using a polyethylene secondary standard. Errors were calculated with standard deviations.

6.2.4 SAXS

SAXS experiments were performed on the BL03XU beamline (Frontier Softmaterial Beamline (FSBL)) at SPring-8, which is located in Sayo, Hyogo, Japan.[22] A monochromated X-ray beam with λ of 1.0 Å was used to irradiate the samples at room temperature and the scattered X-rays were counted at the SDD of

1.2, 4.1, and 8.1 m. For measurements at the SDD of 1.2 and 4.1 m, the height and width of the X-ray beam at the sample position were set to be 0.04 and 0.1 mm, respectively, and the scattered X-rays were counted by an imaging plate detector (R-AXIS VII++, Rigaku Corporation, Japan) with 3000 × 3000 pixel arrays and a pixel size of 0.1 mm pixel^{-1}. For SAXS measurements at the SDD of 8.1 m, the height and width of the X-ray beam at the sample position were set to be 0.2 and 0.05 mm, respectively, and the scattered X-rays were converted into visible light by an X-ray image intensifier (V7739P, Hamamatsu Photonics K. K., Japan), then counted by a 2D charge coupled device (ORCA R2, Hamamatsu Photonics K. K., Japan) with 1344 × 1024 pixel arrays and a pixel size of 0.063 mm pixel^{-1}. After necessary corrections for dark current, background scattering, and transmittance, the corrected scattering intensity functions were normalized to the absolute intensity scale using a glassy carbon secondary standard, which was provided by Jan Ilavsky of Advanced Photon Source at Argonne National Laboratory in Illinois, USA.[23] Errors were calculated with standard deviations.

6.2.5 SEM

Field emission SEM observations were performed on a Hitachi S-4700 instrument. Specimens for the fracture surface analysis were prepared by cracking cured phenolic resins in liquid nitrogen using diagonal cutting pliers. Specimens for the etched surface analysis were prepared by etching the surface of cured phenolic resins via focused ion beam (FIB) milling using an accelerated gallium ion at 30 kV (performed on a Hitachi FB-2000A instrument).

6.3 Results and Discussion

6.3.1 SANS and SAXS

The spatial inhomogeneity of cross-links in phenolic resins was investigated through SANS analyses using partly deuterated phenolic resins with

nondeuterated cross-links in the deuterated matrix. On the basis of such a molecular design, specimens were prepared by curing a deuterated phenolic resin oligomer NVD (ρ_n = 5.87 × 10^{10} cm^{-2}) with a nondeuterated cross-linking agent HMTA (ρ_n = 1.85 × 10^{10} cm^{-2}) to provide a coherent neutron scattering contrast between the matrix and the cross-links that results from the difference in ρ_n.

Figure 6.1a shows the observed SANS intensities ($I_{obs}(q)$) of the phenolic resins that include coherent and incoherent scattering intensities ($I(q)$ and I_{incoh}), in which the statistical error bars are hidden by the graph markers. Here q denotes the magnitude of the scattering vector given by $q = (4\pi/\lambda)\sin(2\theta/2)$, where 2θ denotes the scattering angle. The flattening of $I_{obs}(q)$ in the q range of 0.5–2 nm^{-1} for all curves is due to the influence of the q-independent incoherent neutron scattering. There was good reproducibility of the SANS curves from repeated sample preparations. The values of I_{incoh} for NVD00, NVD05, and NVD10 were estimated to be 0.077, 0.107, and 0.143 cm^{-1}, respectively, by assuming that SANS in the q range of 1–2 nm^{-1} is dominated by incoherent scattering, and the coherent scattering in that range is negligible for all samples. Note that there are slight increases in the intensity at q of 0.03 nm^{-1} for all curves, which may have resulted from combining the scattering data that were obtained under different measurement conditions, as described in section 6.2.3 and indicated with arrows in Figure 6.1a.

Figure 6.1b shows the $I(q)$ of the phenolic resins, the values were obtained by subtracting I_{incoh} from $I_{obs}(q)$. Interestingly, all of the curves are nearly superimposed onto a single curve that follows a power-law relationship between q and $I(q)$ with an exponent (m) approximately equal to −3.5 over the entire measured q range of 0.004–2 nm^{-1}. This power-law relationship is independent of the content of HMTA and is also observed for NVD00 that does not contain nondeuterated cross-links in the deuterated matrix. These results suggest that (i) phenolic resins have an inhomogeneity that exists irrespective of the cross-links and (ii) the spatial inhomogeneity of the cross-links in the range of 3–1600 nm, which is given by $2\pi/q$ in the measured q range (i.e., q = 0.004–2 nm^{-1}), is very

small and negligible in comparison with the preceding inhomogeneity of the phenolic resins in terms of the fluctuations of the neutron scattering length density; namely, the cross-links can be considered to be randomly distributed over

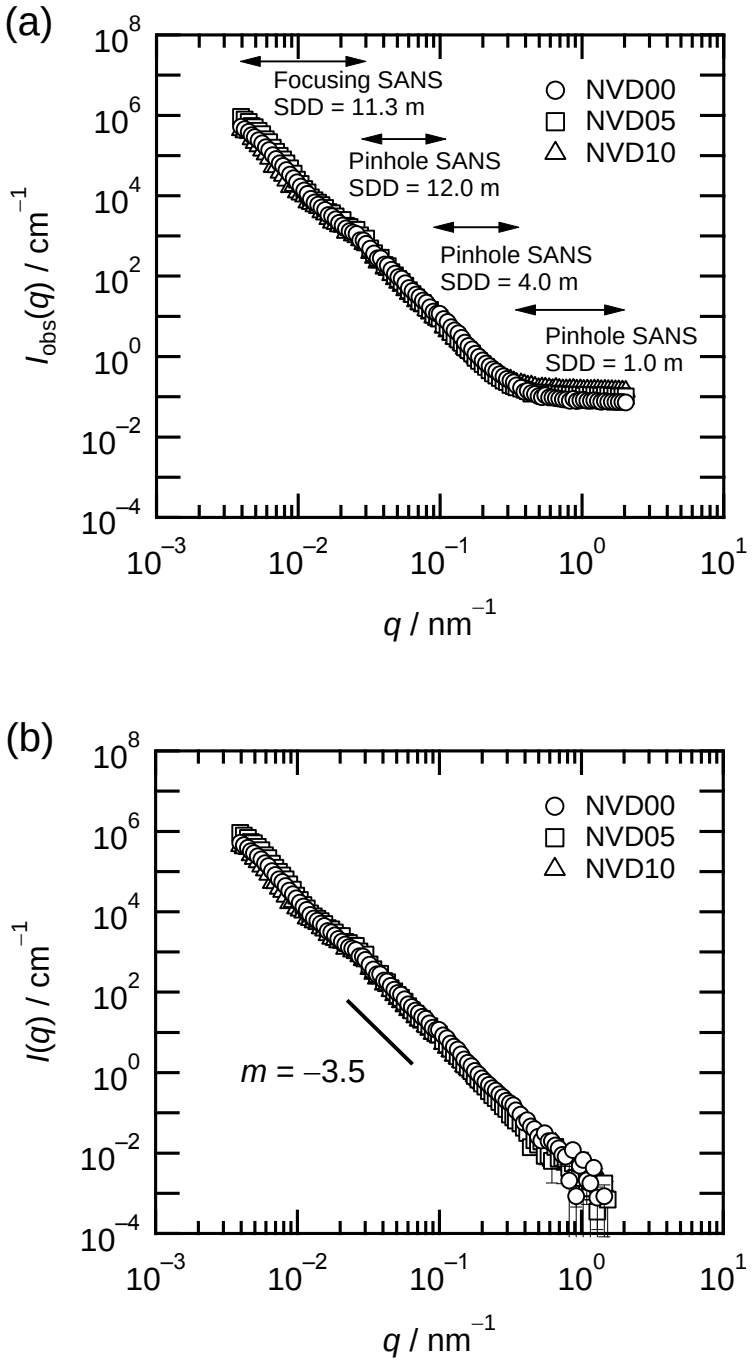

Figure 6.1 SANS curves of the phenolic resins: (a) Observed scattering functions and (b) coherent neutron scattering functions. Circle, NVD00; Square, NVD05; Triangle, NVD10.

the range.

The absence of inhomogeneity of the cross-links in that range is contradictory to the presence of nodular structures with particle sizes ranging from tens to hundreds of nanometers suggested by previous SEM and TEM observations of fractured surfaces.[24–30] On the other hand, our result agrees with the other interpretation of the nodular structures that was previously suggested by SANS and SAXS observations of unfractured thermosetting resins; namely, the nodular structure itself has nothing to do with the evidence of cross-link inhomogeneity.[31–34] Thus, it can be concluded that the nodular structures are a characteristic morphology of the fracture surface and not sufficient to account for the inhomogeneity of the cross-links that likely exists inside unfractured resins. Therefore, to elucidate the origin of the inhomogeneity of phenolic resins more clearly, SAXS analyses were also performed. Figure 6.2 shows the SAXS results for the same specimens that were used for the SANS measurements. As in the case with SANS, all SAXS curves are nearly superimposed onto a single curve that follows a power-law relationship between q and $I(q)$, with m approximately

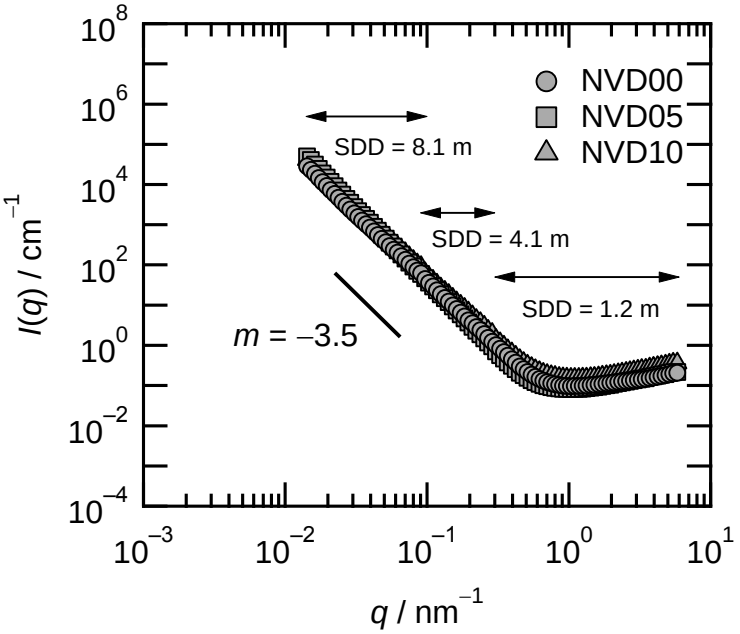

Figure 6.2 SAXS curves of phenolic resins. Circle, NVD00; Square, NVD05; Triangle, NVD10.

equal to −3.5 in the q range of 0.01–0.2 nm^{-1}. This power-law relationship is independent of the content of HMTA in the measured q range. On the other hand, there is an apparent deviation from the power-law relationship in the q range of 0.5–6 nm^{-1}. This upturn of SAXS curves is probably due to a tail of an amorphous halo that results from the short-range density fluctuation of carbon atoms.

To characterize the structure that gives these SANS and SAXS curves, the internal structure of NVD00 was examined considering the fluctuations of the neutron and X-ray scattering length densities. The following results were obtained: (i) There is no neutron scattering contrast resulting from the difference in ρ_n between the deuterated and nondeuterated components, because NVD00 was prepared by compression molding of one deuterated component (NVD), and this lack of contrast cannot explain the SANS results for NVD00. (ii) There is a difference in ρ_n between the deuterated and nondeuterated hydroxyl groups in NVD, whose degree of deuteration was 21%. However, even if the distribution of the hydroxyl groups is inhomogeneous, it would be insufficient to account for the SAXS result for NVD00 because the deuterated and nondeuterated hydroxyl groups have the same number of electrons, and thus, the difference in ρ_x that results only from the difference in densities between these hydroxyl groups would be negligible. (iii) If there are crystalline and noncrystalline domains of NVD in NVD00 and their bulk densities are different, it would cause differences in both ρ_n and ρ_x between these domains, which would result in SANS and SAXS, respectively. However, there might be no crystalline domains in NVD00, because the phenolic resins that are prepared from phenol and formaldehyde using an acid catalyst typically have no crystalline structure.[35] (iv) As ρ_n and ρ_x values of voids are zero, there are clear difference in both ρ_n and ρ_x between the voids and NVD. Assuming NVD00 contains voids with a broad size distribution ranging from the nanometer to micrometer scale, the SANS and SAXS curves of NVD00, as shown in Figures 6.1b and 6.2, can be explained as the scattering from rough interfaces between the voids and NVD that have a surface fractal dimension (D_s) approximately equal to 2.5. The maximum size of the voids would be larger than 1600 nm, which corresponds to a value of q equal to 0.004 nm^{-1}, because a

power-law relationship between q and $I(q)$ is observed in the q range of 0.004–2 nm^{-1}. Note that D_s is given by $D_s = 6 + m$ and the value of D_s ranges from 2 for perfectly smooth surfaces to 3 for extremely rough surfaces.[36]

Conjecture (iv) for NVD00, namely, the presence of the internal fractal interfaces between voids and phenolic resins, is also sufficient to account for the SANS and SAXS results of NVD05 and NVD10. To prove this conjecture, the SANS and SAXS results of these phenolic resins were analyzed through the scattering functions given by

$$I(q) = (\Delta\rho)^2 \langle n \rangle \langle V_0^2 \rangle P(q) S(q), \tag{6.1}$$

where $\Delta\rho$ denotes the difference in the scattering length density between voids and phenolic resins ($\Delta\rho_n$ for SANS and $\Delta\rho_x$ for SAXS); n and V_0 denote the number density and volume of voids, respectively, and angle brackets denote the ensemble average; and $P(q)$ and $S(q)$ denote the function of the form factor of voids and the inter-void structure factor, respectively. When both the SANS and SAXS curves, as shown in Figures 6.1b and 6.2, primarily result from the difference in the scattering length density between voids and phenolic resins, the difference in the scattering function given by eq 6.1 between SANS and SAXS is just the scattering contrast term $(\Delta\rho)^2$. Thus, the SANS and SAXS curves normalized by $(\Delta\rho)^2$ should give the same function, where the values of $\Delta\rho$ for SANS and SAXS are equal to ρ_n and ρ_x of phenolic resins, respectively, because these values of voids are zero. Table 6.1 summarizes the values of $\Delta\rho_n$ and $\Delta\rho_x$ for NVD00, NVD05,

Table 6.1 Structural parameters

sample	unit formula[a]	d / g cm^{-3}	$\Delta\rho_n$ / cm^{-2}	$\Delta\rho_x$ / cm^{-2}
NVD00	$C_{50.53}H_{9.84}D_{36.40}N_{1.38}O_{7.01}$	1.29	5.87×10^{10}	1.20×10^{11}
NVD05	$C_{39.11}H_{10.40}D_{27.06}N_{2.05}O_{5.22}$	1.29	5.64×10^{10}	1.20×10^{11}
NVD10	$C_{22.35}H_{11.21}D_{13.36}N_{3.04}O_{2.58}$	1.29	5.43×10^{10}	1.20×10^{11}

[a] Estimated from the molar ratio of NVD ($C_{50.53}H_{9.84}D_{36.40}N_{1.38}O_{7.01}$; d = 1.29 g cm^{-3}) and HMTA ($C_6H_{12}N_4$; d = 1.33 g cm^{-3}) in the mixtures used for compression molding. The unit formula of NVD was estimated from M_n and the degree of deuteration by assuming that NVD is a linear polymer.

and NVD10, which are estimated from their unit formulas and *d*, in which the unit formulas were calculated from the molar ratio of NVD and HMTA in the mixture for compression molding.

Figure 6.3 shows the normalized SANS and SAXS curves, $(\Delta\rho)^{-2}I(q)$ vs q for NVD00, NVD05, and NVD10. The curves for each sample can be nearly superimposed onto a single curve in the q range of 0.015–0.2 nm^{-1}, which strongly confirms that the SANS and SAXS results for the phenolic resins primarily result from the difference in the scattering contrast between the voids and the phenolic resins. Note that there is a large deviation between the normalized SANS and SAXS curves in the q range of 0.5–2 nm^{-1}. This deviation can be explained by the difference in the short-range fluctuations of ρ_n and ρ_x that correspond to the local structure of deuterated polymers. The upturn of SAXS curves is probably owing to a tail of an amorphous halo that results from the short-range density fluctuation of carbon atoms. On the other hand, the short-range fluctuation of ρ_n is generally smaller than that of ρ_x for deuterated

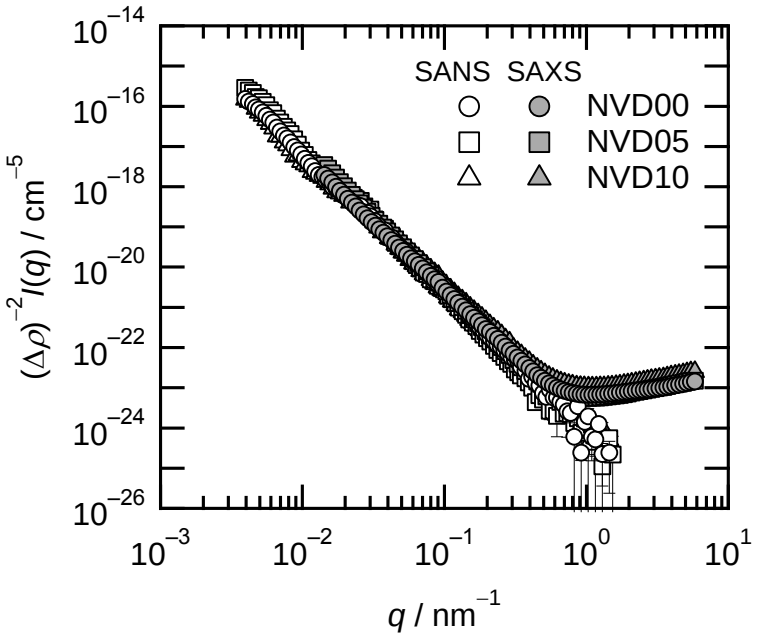

Figure 6.3 Normalized scattering functions of the phenolic resins: Circle, NVD00; Square, NVD05; Triangle, NVD10: Open symbol, SANS; Filled Symbol, SAXS.

amorphous polymers because there is no significant difference in the coherent neutron scattering lengths between carbon and deuterium (i.e., 6.65×10^{-13} and 6.67×10^{-13} cm, respectively). Thus, the SANS curves in the entire measured range are considered to be due to the difference in the scattering contrast between the voids and the phenolic resins.

For surface fractals, $P(q)$ for sizes well below the correlation length of the voids (ξ), namely, $\xi q >> 1$, was derived by Bale and Schmidt as[37]

$$P(q) = \pi S_0 \left\langle V_0^{-2} \right\rangle \Gamma(5 - D_s) \sin\left(\frac{\pi(D_s - 1)}{2}\right) q^{-(6-D_s)}, \quad (6.2)$$

where S_0 denotes the total surface area of the interfaces between voids and phenolic resins and has a unit of cm^{Ds}, and $\Gamma(5 - D_s)$ is the gamma function given by

$$\Gamma(5 - D_s) = \int_0^\infty x^{(5-D_s)-1} e^{-x} dx. \quad (6.3)$$

Note that there are arguments as to whether scattering contributions from fractal surfaces vanish in the $D_s \rightarrow 3$ limit because eq 6.2 states that $P(q)$ becomes zero when D_s is 3. Wong and Bray pointed out that this issue results from overlooking a subtle prefactor in eq 6.2.[38,39] They proposed a modified function given by a form of eq 6.2 divided by a factor $(3 - D_s)$ that does not vanish when D_s is 3 owing to the introduction of a sinc function (i.e., $\sin[\pi(3 - D_s)/2]/(3 - D_s)$, where $\sin[\pi(3 - D_s)/2]$ is equal to $\sin[\pi(D_s - 1)/2]$ in eq 6.2). On the other hand, Pfeifer and Schmidt pointed out that scattering contributions from internal surfaces should vanish in the $D_s \rightarrow 3$ limit and that there is no overestimation of a prefactor in eq 6.2 because the space is fully occupied by the surface and there is no boundary dividing the two phases (i.e., no density fluctuation) when D_s is equal to 3.[40–42] On the basis of these arguments, eq 6.2 was chosen as the formula for $P(q)$ in this study because the SANS and SAXS curves in Figures 6.1b and 6.2 indicate that phenolic resins have a value of D_s well below 3 (i.e., $m < -3$). The form factor $S(q)$ can be approximated to be unity when the volume fraction of the voids ($\langle n \rangle \langle V_0 \rangle$) is very small,[43] such that eq 6.1 can be expressed as[37]

$$I(q) = \pi(\Delta\rho)^2 \langle n \rangle S_0 \, \Gamma(5 - D_s) \sin\left(\frac{\pi(D_s - 1)}{2}\right) q^{-(6-D_s)}. \quad (6.4)$$

The SANS curves in Figure 6.1b were fitted using eq 6.4, and the values of the fitting parameters D_s and $\langle n \rangle S_0$ were obtained. The specific surface area (S_{sp}) was then calculated using $S_{sp} = \langle n \rangle S_0 d^{-1}$, with units of $cm^{Ds}\ g^{-1}$. The results are summarized in Table 6.2. Among the three samples, NVD05 has the smallest value of D_s (2.46) and the largest value of S_{sp} (1.54 $cm^{2.46}\ g^{-1}$). NVD00 and NVD10 have similar values of D_s (~2.6) and $\langle n \rangle S_0$ (~$10^{-1}\ cm^{2.6}\ g^{-1}$). However, NVD10 has smaller D_s and larger S_{sp} than NVD00.

These results can be explained by considering the cross-linking reaction and the degree of cross-linking of the phenolic resins. Phenolic resins that are prepared by compression molding originally have an inhomogeneity that is associated with the internal fractal interfaces between voids and phenolic resins, with D_s equal to ~2.6 and S_{sp} equal to ~$10^{-1}\ cm^{2.6}\ g^{-1}$. This inhomogeneity is related to compression molding and is independent of the content of the cross-linking agent. When the phenolic resins are cured with the cross-linking agent HMTA, cross-links are produced by the degradation of HMTA. The cross-linking reaction is initiated by formation of hydrogen bonds between the hydroxyl groups of phenolic resins and the nitrogen atoms of HMTA, followed by proton transfer to the nitrogen atoms, where almost all of the HMTA decomposes at the very initial stage of the cross-linking reaction under the molding conditions (i.e., 165 °C and 40 MPa in this study). The details of the reaction mechanisms are described in the literatures.[35,44,45] Most of the degraded HMTA forms cross-links, but some part of it is decomposed to low molecular weight volatile byproducts

Table 6.2 SANS curve fitting results

sample	D_s / –	S_{sp} / $cm^{Ds}\ g^{-1}$
NVD00	2.56 ± 0.03	0.349 ± 0.002
NVD05	2.46 ± 0.05	1.54 ± 0.01
NVD10	2.60 ± 0.05	0.188 ± 0.002

such as ammonia. The volatile products are generally degassed outside the phenolic resins by applying sufficient pressure during compression molding, which causes diffusion of the volatile products in the phenolic resins and results in formation of voids. When the number of cross-links is sufficient, as is the case with NVD10, the voids vanish because they are compressed by the molding pressure and then tightly clamped by sufficient cross-links. This change also accompanies a decrease in the amount of original internal fractal interfaces, which results in a decrease in S_{sp} and an increase in D_s. On the other hand, if the number of cross-links is not sufficient, as is the case with NVD05, the cross-links cannot clamp all of the compressed void structure, which results in the generation of void structures after the release of the molding pressure. The resulting interface between the voids and phenolic resins is slightly smoother in comparison with the original internal fractal interface, which leads to an increase in S_{sp} and a decrease in D_s.

6.3.2 SEM

The complementary SANS and SAXS analyses clearly indicate that phenolic resins have inhomogeneity that is characterized as the fractal interfaces between voids and phenolic resins. On the other hand, as is the case with the previously reported SAXS observation of epoxy resins,[33] this result is inconsistent with the existence of an inhomogeneity associated with the nodular structures that have been observed on the fracture surface of thermosetting resins by SEM and TEM analyses. To address this issue, SEM analysis was performed on the specimens that were used for both the SANS and SAXS measurements.

Figures 6.4a and 6.4b show SEM images of the freeze-fracture surfaces of NVD05 and NVD10, respectively. As is the case with previous SEM and TEM observations,[24–31] particle-like nodular structures with sizes ranging from tens to hundreds of nanometers are observed for both samples. There are also void-like structures with sizes ranging from tens to hundreds of nanometers. In order to clarify whether these voids were produced in the fracturing process or originally

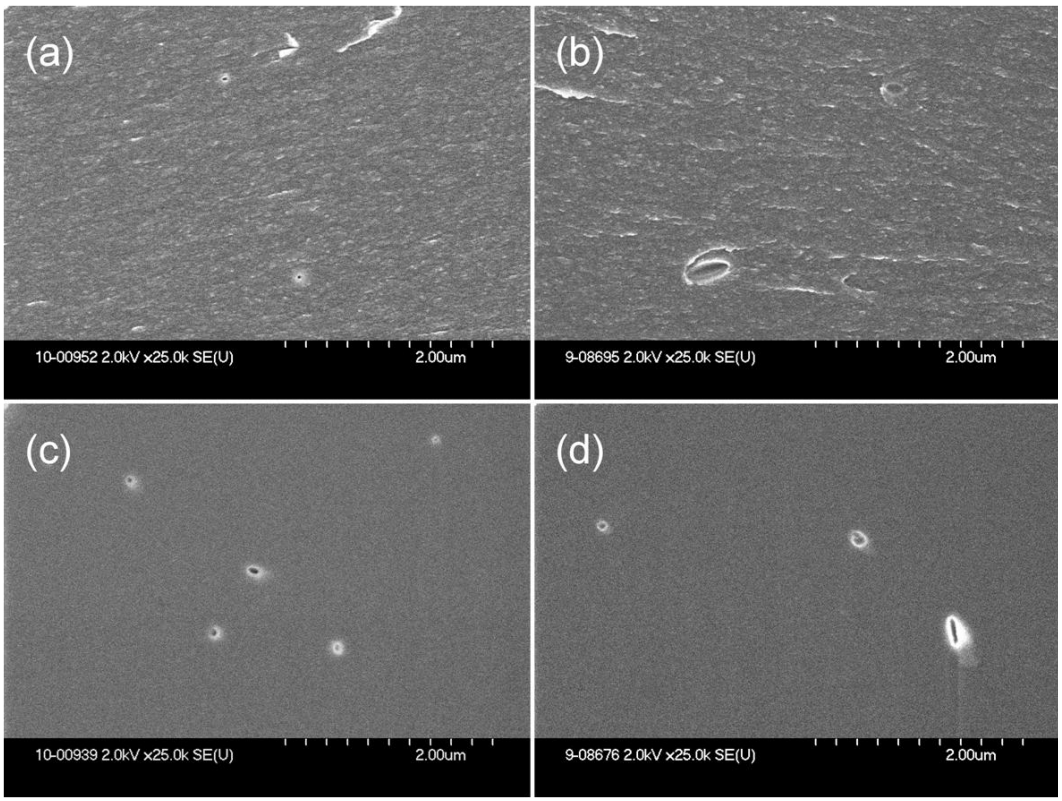

Figure 6.4 FE-SEM images of phenolic resins: freeze-fractured surfaces of (a) NVD05 and (b) NVD10; FIB etched surfaces of (c) NVD05 and (d) NVD10.

existed before fracture, the surfaces of the specimens were etched by FIB milling and observed by SEM. Note that the FIB milling technique has been broadly used in the field of cross-sectional SEM and TEM analyses of semiconductor devices because it can etch samples without damaging fine nanostructures.[46] However, to our knowledge, it has not been applied in the study of the inhomogeneity of thermosetting resins. Figures 6.4c and 6.4d show FIB-SEM images of NVD05 and NVD10, respectively. A couple of white circles with sizes ranging from tens to hundreds of nanometers are observed for both samples, which could be characterized as the edges of voids. This conclusion is based on the fact that the brightness of the image relates to the number of secondary electrons emitted from the specimen surface to the detector where the number of secondary electrons

depends on the angle of incident electrons on the surface. A higher incident angle results in a larger emission of secondary electrons, and thus, the edge of the voids gives a brighter image than other surfaces, a behavior that is referred to as the edge effect.[47] These results indicate that voids with sizes ranging from tens to hundreds of nanometers originally existed before fracture. More interestingly, the etched surface does not have the cross-sectional pattern corresponding to the nodular structures that are observed at the fracture surface, which suggests that the nodular structure are related to the fracture process of the sample and would appear only on fracture surfaces.

6.4 Conclusions

Complementary SANS, SAXS, and SEM analyses were performed to investigate the inhomogeneity of phenolic resins prepared by compression molding of a deuterated phenolic resin oligomer NVD and a nondeuterated curing agent HMTA. Both the SANS and SAXS curves of the phenolic resins exhibit a power-law relationship between q and $I(q)$ with an exponent approximately equal to −3.5 in the measured q ranges of 0.004–2 nm^{-1} (SANS) and 0.01–0.2 nm^{-1} (SAXS). This power-law relationship was independent of the amount of HMTA. These scattering results obtained by utilizing partly deuterated phenolic resins indicate that (i) phenolic resins have an inhomogeneity characterized by the internal fractal interfaces between voids and phenolic resins irrespective of cross-links and (ii) the spatial inhomogeneity of the cross-links in the range of 3–1600 nm is small and negligible in comparison with the above-mentioned inhomogeneity in terms of the fluctuations of the neutron and X-ray scattering length densities, and the cross-links can be considered to be randomly distributed over the range. By considering the difference in the scattering contrast term $(\Delta\rho)^2$ between the SANS and SAXS functions, the presence of voids is confirmed by the superposition of the normalized SANS and SAXS functions $(\Delta\rho)^{-2}I(q)$. It should be mentioned that this firm conclusion cannot be obtained solely from either

SANS or SAXS. The values of D_s and S_{sp} of the phenolic resins, estimated by fitting the SANS curves using the scattering function of the fractal surface, are estimated to be 2.5–2.6 and 10^{-1}–10^{0} cm^{Ds} g^{-1}, respectively. When NVD is cured with a half-stoichiometric amount of HMTA, new void structures are generated owing to the introduction of an insufficient number of cross-links, which results in a decrease in D_s and an increase in S_{sp} in comparison with NVD00. On the other hand, when NVD is cured with a stoichiometric amount of HMTA, the formation of new void structures is suppressed and initially existing interfaces between voids and phenolic resins decrease owing to the introduction of a sufficient amount of cross-links, which in turn results in an increase in D_s and a decrease in S_{sp} in comparison with NVD00. The FIB-SEM analyses of etched surfaces of the phenolic resins indicated the presence of voids with sizes ranging from tens to hundreds of nanometers and the absence of nodular structures that are observed at the fracture surface, which supports the above mentioned SANS and SAXS results for the phenolic resins.

6.5 References

1 M. Shibayama, *Macromol. Chem. Phys.*, 1998, **199**, 1–30.

2 M. Shibayama and T. Norisuye, *Bull. Chem. Soc. Jpn.*, 2002, **75**, 641–659.

3 M. Shibayama, T. Karino, Y. Domon and K. Ito, *J. Appl. Cryst.*, 2007, **40**, s43–s47.

4 E. Girard-Reydet, H. Sautereau, J. P. Pascault, P. Keates, P. Navard, G. Thollet and G. Vigier, *Polymer*, 1998, **39**, 2269–2279.

5 F. L. Meng, S. X. Zheng, H. Q. Li, Q. Liang and T. X. Liu, *Macromolecules*, 2006, **39**, 5072–5080.

6 D. Hu, Z. G. Xu, K. Zeng and S. X. Zheng, *Macromolecules*, 2010, **43**, 2960–2969.

7 J. Brus, M. Špírková, D. Hlavatá and A. Strachota, *Macromolecules*, 2004, **37**, 1346–1357.

8 D. W. Schaefer and R. S. Justice, *Macromolecules*, 2007, **40**, 8501–8517.

9 H. Zou, S. S. Wu and J. Shen, *Chem. Rev.*, 2008, **108**, 3893–3957.

10 E. Hoinkis and A. J. Allen, *Carbon*, 1991, **29**, 81–91.

11 A. Gupta and I. R. Harrison, *Carbon*, 1994, **32**, 953–960.

12 J. M. Calo, P. J. Hall and M. Antxustegi, *Colloids Surf., A*, 2001, **187–188**, 219–232.

13 J. M. Calo and P. J. Hall, *Carbon*, 2004, **42**, 1299–1304.

14 G. Goerigk, H. G. Haubold, O. Lyon and J. P. Simon, *J. Appl. Cryst.*, 2003, **36**, 425–429.

15 H. B. Stuhrmann, *Adv. Polym. Sci.*, 1985, **67**, 123–163.

16 A. Izumi, T. Nakao and M. Shibayama, *J. Polym. Sci., Part A: Polym. Chem.*, 2011, **49**, 4941–4947.

17 S. Okabe, M. Nagao, T. Karino, S. Watanabe, T. Adachi, H. Shimizu and M. Shibayama, *J. Appl. Cryst.*, 2005, **38**, 1035–1037.

18 S. Okabe, T. Karino, M. Nagao, S. Watanabe and M. Shibayama, *Nucl. Instrum. Methods Phys. Res., Sect. A*, 2007, **572**, 853–858.

19 H. Iwase, H. Endo, M. Katagiri and M. Shibayama, *J. Appl. Cryst.*, 2011, **44**, 558–568.

20 M. R. Eskildsen, P. L. Gammel, E. D. Isaacs, C. Detlefs, K. Mortensen and D. J. Bishop, *Nature*, 1998, **391**, 563–566.

21 S. M. Choi, J. G. Barker, C. J. Glinka, Y. T. Cheng and P. L. Gammel, *J. Appl. Cryst.*, 2000, **33**, 793–796.

22 H. Masunaga, H. Ogawa, T. Takano, S. Sasaki, S. Goto, T. Tanaka, T. Seike, S. Takahashi, K. Takeshita, N. Nariyama, H. Ohashi, T. Ohata, Y. Furukawa, T. Matsushita, Y. Ishizawa, N. Yagi, M. Takata, H. Kitamura, K. Sakurai, K. Tashiro, A. Takahara, Y. Amamiya, K. Horie, M. Takenaka, T. Kanaya, H. Jinnai, H. Okuda, I. Akiba, I. Takahashi, K. Yamamoto, M. Hikosaka, S. Sakurai, Y. Shinohara, A. Okada and Y. Sugihara, *Polym. J.*, 2011, **43**, 471–477.

23 F. Zhang, J. Ilavsky, G. G. Long, J. P. G. Quintana, A. J. Allen and P. R. Jemian, *Metall. Mater. Trans. A*, 2010, **41A**, 1151–1158.

24 R. A. Spurr, E. H. Erath, H. Myers and D. C. Pease, *Ind. Eng. Chem.*, 1957, **49**, 1839–1842.

25 E. H. Erath and R. A. Spurr, *J. Polym. Sci.*, 1959, **35**, 391–399.

26 J. L. Racich and J. A. Koutsky, *J. Appl. Polym. Sci.*, 1976, **20**, 2111–2129.

27 V. B. Gupta, L. T. Drzal, W. W. Adams and R. Omlor, *J. Mater. Sci.*, 1985, **20**, 3439–3452.

28 J. Mijović and L. Tsay, *Polymer*, 1981, **22**, 902–906.

29 H. Kishi, T. Naitou, S. Matsuda, A. Murakami, Y. Muraji and Y. Nakagawa, *J. Polym. Sci., Part B: Polym. Phys.*, 2007, **45**, 1425–1434.

30 J. Mijović and J. A. Koutsky, *Polymer*, 1979, **20**, 1095–1107.

31 K. Dušek, J. Pleštil, F. Lednický and S. Luňák, *Polymer*, 1978, **19**, 393–397.

32 K. Dušek, *Angew. Makromol. Chem.*, 1996, **240**, 1–15.

33 R. J. Matyi, D. R. Uhlmann and J. A. Koutsky, *J. Polym. Sci., Part B: Polym. Phys.*, 1980, **18**, 1053–1063.

34 S. J. Bai, *Polymer*, 1985, **26**, 1053–1057.

35 A. Gardziella, L. A. Pilato and A. Knop, *Phenolic Resins: Chemistry, Applications, Standardization, Safety and Ecology*, 2nd completely rev. edn., Springer, Berlin, 1999.

36 R. J. Roe, *Methods of X-ray and Neutron Scattering in Polymer Science*, Oxford University Press, New York, 2000.

37 H. D. Bale and P. W. Schmidt, *Phys. Rev. Lett.*, 1984, **53**, 596–599.

38 P. Z. Wong and A. J. Bray, *J. Appl. Cryst.*, 1988, **21**, 786–794.

39 P. Z. Wong and A. J. Bray, *Phys. Rev. Lett.*, 1988, **60**, 1344–1344.

40 P. Pfeifer and P. W. Schmidt, *Phys. Rev. Lett.*, 1988, **60**, 1345–1345.

41 P. W. Schmidt, Use of Scattering to Determine the Fractal Dimension. in *The Fractal Approach to Heterogeneous Chemistry: Surfaces, Colloids, Polymers*, ed. D. Avnir, John Wiley & Sons, Chichester, England, 1989.

42 P. W. Schmidt, *J. Appl. Cryst.*, 1991, **24**, 414–435.

43 J. Teixeira, *J. Appl. Cryst.*, 1988, **21**, 781–785.

44 S. A. Sojka, R. A. Wolfe and G. D. Guenther, *Macromolecules*, 1981, **14**,

1539–1543.

45 X. Zhang, M. G. Looney, D. H. Solomon and A. K. Whittaker, *Polymer*, 1997, **38**, 5835–5848.

46 L. A. Giannuzzi and F. A. Stevie, *Introduction to Focused Ion Beams: Instrumentation, Theory, Techniques, and Practice*, Springer, New York, 2005.

47 G. H. Michler, *Electron Microscopy of Polymers*, Springer, Berlin, 2008.

Summary

To elucidate the cross-link inhomogeneity of phenolic resins, phenolic resins were investigated using molecular dynamics (MD) simulations and light, neutron, and X-ray scattering techniques. The structure–property relationship of cross-linked phenolic resins was successfully characterized from the atomistic viewpoint using fully atomistic MD simulations (in Chapter 2). Cross-link inhomogeneity of phenolic resins was studied through structural analysis at their oligomerization (in Chapter 3), gelation (in Chapter 4), and curing processes (in Chapters 5 and 6) using dynamic light scattering (DLS), small-angle neutron and X-ray scattering (SANS and SAXS, respectively).

Through these investigations, we have successfully demonstrated the presence of the inhomogeneity during their gelation process and characterized the mechanism of the formation and growth of the inhomogeneity. In addition, we want to emphasize that the topic of this study addresses general issues of thermosetting resins and is not limited specially to phenolic resins, which is important because elucidating their cross-link inhomogeneity remains one of the major objectives of studies on thermosetting resins, and this study offers a new technique for elucidating the inhomogeneity of thermosetting resins. The details of the respective chapters are summarized below.

In Chapter 2, cross-linked phenolic resins were studied by atomistic MD simulations. Cross-linked structures consisting of a network of three functional phenols and two functional methylenes with the degrees of cross-linking (*D*) equal to 0.70, 0.82, and 0.92 were prepared by the cross-linking reactions of linear novolac-type phenolic resins that have an all-*ortho* configuration and the degree of polymerization of 9 in a unit cell under three-dimensional periodic boundary

conditions. The glass-transition temperature (T_g) shows clear dependence on D, namely, an increase in D accompanied an increases in T_g, which indicates that segmental motions were suppressed by the cross-links. Then, uniaxial elongations of the cross-linked structures were performed in the strain range of 0–0.03 at 300 K (i.e., below T_g). The change in the potential energies owing to the uniaxial elongation indicated that cross-links suppressed local segmental motions in the cross-linked structures, probably at the region around the linear and terminal phenols. As a result, it was found that an increase in the degree of cross-linking accompanied a decrease in Poisson's ratio and an increase in Young's modulus.

In Chapter 3, solution properties of unfractionated phenolic resins prepared by the polycondensation of phenol (PhOH) and formaldehyde (HCHO) using oxalic acid (OX) as a catalyst were investigated by gel permeation chromatography (GPC), DLS, and SANS experiments. The hydrodynamic radius (R_h) in 1 vol% acetone solution obtained by DLS obeys the power-law relation with the *z*-average molecular weight (M_z) (estimated by GPC) and obtained the scaling exponent of 0.57. SANS curves of 10 vol% solution in THF-d_8 were fitted using the Ornstein–Zernike (OZ) equation and could be superimposed to a single curve with the reduced variables, $\xi^{-2}I(q)$ and ξq, where ξ and q denote the correlation length and the magnitude of the scattering vector, respectively. These results indicate that ξ is determined by the polymer size or molecular weight and the polymers have a self-similar structure with respect to the molecular-weight distribution. In addition, ξ obeys the power-law relation with M_z with the scaling exponent of 0.27. These results indicates that phenolic resin oligomers grow as polymerization proceeds with a power-law of $R_h \sim M_z^{0.57}$ and ξ evolves with $\xi \sim M_z^{0.57}$, while maintaining the self-similarity between $\xi^{-2}I(q)$ and ξq.

In Chapter 4, to elucidate the cross-link inhomogeneity of novolac-type phenolic resins, their gelation process during polycondensation of phenol and formaldehyde using oxalic acid as an acid catalyst at 100 °C was investigated using ^{13}C-NMR and SAXS analyses. The initial molar ratios $[PhOH]_0/[HCHO]_0/[OX]_0$ were chosen to be 1.0/1.0/0.01, 1.0/1.2/0.01 (i.e., off-stoichiometric ratios) and 1.0/1.5/0.01 (i.e., on-stoichiometric ratio). The

change in the ratio of methylene-to-phenolic units with reaction time, which was estimated using ^{13}C-NMR spectra, implies the presence of different gelation mechanisms that depend on the ratio of $[HCHO]_0/[PhOH]_0$. To characterize the mechanism, SAXS experiments were performed with 7 wt% semidilute THF solutions for the soluble polymers and fully THF-swollen gels (i.e., in the semidilute state) for the insoluble polymers. The SAXS curves from the 7 wt% solutions are well fitted by the OZ equation. On the other hand, the SAXS curves after gelation can be fitted by a combination of the OZ and the Squared–Lorentz (SL) equations, which describe liquid-like fluctuations and solid-like frozen inhomogeneity, respectively. This result indicates that there is frozen cross-link inhomogeneity in the network structure of phenolic resins. The change in the correlation length of the OZ equation with reaction time indicates an increase in the size of the polymer chains before gelation and a decrease in the mesh size of the gel network after gelation. The change in the correlation length of the inhomogeneity of the SL equation indicates that the formation and growth of the inhomogeneity of phenolic resins depends on the amount of a cross-linker; namely, there are different mechanisms when there is (i) an insufficient or (ii) a sufficient amount of a cross-linker. In case (i), inhomogeneous domains with a loosely cross-linked network appear at the initial stage of gelation. The degree of cross-linking in the domain increases with the reaction time, which results in a decrease in the degree of swelling of the domain. In case (ii), inhomogeneous domains with a tightly cross-linked network appear at the initial stage of gelation, followed by an increase in the size of the domain.

In Chapter 5, the highly deuterated random novolac-type phenolic resin (NVD) was prepared by the polycondensation of deuterated phenol and formaldehyde using oxalic acid as an acid catalyst. The polycondensation of deuterated monomers was confirmed by GPC analysis, and the molecular weight distribution of the resulting deuterated polymer was similar to that of the nondeuterated polymer prepared under the same synthetic conditions. The polymer conformation in THF at 40 °C was evaluated from the scaling exponent of the Mark–Houwink–Sakurada equation, and the exponent of 0.26 was obtained

for the deuterated phenolic resin. This value is close to our experimental value and the previously reported values for nondeuterated phenolic resins, which suggests that phenolic resins in THF behave like a compact sphere irrespective of deuteration. From DSC analysis, the curing reaction of phenolic resins with hexamethylenetetramine (HMTA) took place irrespective of deuteration. The cured deuterated phenolic resin exhibits a lower incoherent neutron scattering background than that of the nondeuterated phenolic resin. These results confirm that this highly deuterated phenolic resin NVD is suitable for matrix resins with low incoherent backgrounds for the SANS study of the thermosetting resins.

In chapter 6, complementary SANS, SAXS, and SEM analyses were performed to investigate the inhomogeneity of phenolic resins prepared by compression molding of a deuterated phenolic resin oligomer NVD and a nondeuterated curing agent HMTA. The SANS and SAXS results indicate that (i) phenolic resins have an inhomogeneity characterized by the internal fractal interfaces between voids and phenolic resins irrespective of cross-links and (ii) the spatial inhomogeneity of the cross-links in the range of 3–1600 nm is small and negligible in comparison with the abovementioned inhomogeneity in terms of the fluctuations of the neutron and X-ray scattering length densities, and the cross-links can be considered to be randomly distributed over the range. The values of surface fractal dimension (D_s) and the specific surface area (S_{sp}) of the phenolic resins, estimated by fitting the SANS curves using the scattering function of the fractal surface, indicate that (i) when NVD is cured with a half-stoichiometric amount of HMTA, new void structures are generated owing to the introduction of an insufficient number of cross-links, which results in a decrease in D_s and an increase in S_{sp}, on the other hand, (ii) when NVD is cured with a stoichiometric amount of HMTA, the formation of new void structures is suppressed and initially existing interfaces between voids and phenolic resins decrease owing to the introduction of a sufficient amount of cross-links, which in turn results in an increase in D_s and a decrease in S_{sp}. The FIB-SEM analyses of etched surfaces of the phenolic resins indicated the presence of voids with sizes ranging from tens to hundreds of nanometers and the absence of nodular

structures that are observed at the fracture surface, which supports the above mentioned SANS and SAXS results for the phenolic resins.

List of Publications

1 Atsushi Izumi, Toshio Nakao and Mitsuhiro Shibayama, "Atomistic Molecular Dynamics Study of Cross-Linked Phenolic Resins", *Soft Matter*, 2012, **8** (19), 5283–5292. DOI: 10.1039/c2sm25067e. (**Chapter 2**)

2 Atsushi Izumi, Takeshi Takeuchi, Toshio Nakao and Mitsuhiro Shibayama, "Dynamic Light Scattering and Small-Angle Neutron Scattering Studies on Phenolic Resin Solutions", *Polymer*, 2011, **52** (19), 4355–4361. DOI: 10.1016/j.polymer.2011.06.059. (**Chapter 3**)

3 Atsushi Izumi, Toshio Nakao and Mitsuhiro Shibayama, "Gelation and Cross-link Inhomogeneity of Phenolic Resins Studied by ^{13}C-NMR Spectroscopy and Small-Angle X-ray Scattering", *Soft Matter*, in press. DOI: 10.1039/c3sm27438a. (**Chapter 4**)

4 Atsushi Izumi, Toshio Nakao and Mitsuhiro Shibayama, "Synthesis and Properties of a Deuterated Phenolic Resin", *J. Polym. Sci., Part A: Polym. Chem.*, 2011, **49** (23), 4941–4947. DOI: 10.1002/pola.24948. (**Chapter 5**)

5 Atsushi Izumi, Toshio Nakao, Hiroki Iwase and Mitsuhiro Shibayama, "Structural Analysis of Cured Phenolic Resins Using Complementary Small-Angle Neutron and X-ray Scattering and Scanning Electron Microscopy", *Soft Matter*, 2012, **8** (32), 8438–8445. DOI: 10.1039/c2sm26072g. (**Chapter 6**)

Acknowledgments

This dissertation is based on the study carried out in the research group of Professor Mitsuhiro Shibayama at Department of Advanced Materials Science, Graduate School of Frontier Sciences, The University of Tokyo from 2009 to 2013.

First of all, I would like to gratefully and sincerely thank Professor Mitsuhiro Shibayama. This dissertation would not have been possible without his patient guidance and encouragement throughout my research. He has generously provided me with his deep and thorough knowledge of polymer physics to perform my research. I really appreciate his instruction and feel honored to be a member of his research group.

I am deeply grateful to Dr. Toshio Nakao for his insightful comments, suggestions, and encouragement throughout this research. He introduced me to this scientific field regarding network polymers and has generously given me his knowledge, views, and experience. I am so honored to be a member of the Nakao group in my career as a scientist.

I also want to thank Professor Toshio Masuda, my master's thesis advisor at Kyoto University, for encouraging me to complete this dissertation.

My special thanks are extended to my colleagues of Sumitomo Bakelite group, all present and past members of Shibayama laboratory, and all the staff of Neutron Scattering Laboratory, the Institute of Solid State Physics, The University of Tokyo, for their kind cooperation.

Finally, I am deeply indebted to my family for their support, patience, and encouragement during the course of my work.

February, 2013

Atsushi Izumi